Magnetic Domain Walls
and
Spin Current-driven
Magnetization Manipulation
in confined Geometries
probed with
High Resolution SEMPA

Dissertation
zur Erlangung des Grades
"Doktor der Naturwissenschaften (Dr. rer. nat.)"
am Fachbereich Physik
der Johannes Gutenberg-Universität Mainz

Pascal Krautscheid
geboren in Stadthagen

Mainz, September 2017

JG|U

Pascal Krautscheid

Magnetic Domain Walls and Spin Current-driven Magnetization Manipulation
in confined Geometries probed with High Resolution SEMPA

Johannes Gutenberg-Universität Mainz
AG Kläui
Institut für Physik
Staudingerweg 7
55128 Mainz

Kurzzusammenfassung

Das heute vorherrschende Datenspeichermedium setzt auf die kontrollierte Modifikation der Magnetisierung von ferromagnetischen Dünnfilmen oder Strukturen im Nanometerbereich. Die traditionelle Herangehensweise benutzt Magnetfelder zum Schalten von magnetischen Zuständen und erreicht durch die Kombination mit fortschrittlichen magnetischen Abtastungverfahren ein exponentielles Wachstum der Datendichte, unterdessen versprechen neue Anätze weitere Fortschritte in diesem Bereich. Der Stillstand in der Speicherlatenz und Leistung bei wahlfreiem Zugriff führte jedoch dazu, dass der Datenspeicher zu einem Flaschenhals in der Computerarchitektur wurde. Infolgedessen führte ein gestiegenes Interesse in bisher nicht genutzte Wechselwirkungen zur Entwicklung von neuen Ansätzen, darunter die Spinstrom induzierte Modifikation von wohldefinierten magnetischen Zuständen. Basierend auf der Strom induzierten Verschiebung von Domänenstrukturen entlang eines dünnen und schmalen magnetischen Drahtes stellte Parkin im Jahr 2008 das Konzept des Racetrack-Speichers vor. Dazu bedarf es einer Untersuchung geeigneter Geometrien, die die zuverlässige Erzeugung und Beeinflussung zugeschnittener magnetischer Zustände zulassen, sowie ein hinreichendes Verständnis der zugrundeliegenden physikalischen Paramater, die die Strom induzierte Magnetisierungsdynamik bestimmen.

In der vorliegenden Arbeit wurden zwei erwartete Voraussetzungen für Domänenwandbasierte Spintronik betrachtet. Insbesondere untersuchten wir sowohl die Stabilität von Domänenwandzuständen als auch Ansätze zur effizienten Modifikation von technisch relevanten Systemparametern. Zuerst wurde die kontrollierte Enstehung von magnetischen Domänenwänden in ferromagnetischen Eisenringen verschiedener Größe untersucht indem wir die Dicke und den inneren Durchmesser in einem technisch interessanten Bereich variierten und die enstandenen Zustände mit einem hochauflösenden Rasterelektronenmikroskop mit Polarisationsanalyse (SEMPA) abbildeten. Mikromagnetische Simulationen bei $0\,\mathrm{K}$ wurden durchgeführt, die die Nukleation von Domänenstrukturen nachbildeten und die Metastabilität bestimmter magnetischer Konfigurationen berücksichtigte. Es wurde gezeigt, dass der niedrigste Energiezustand, der durch ein Zusammenspiel der Austausch- und magnetostatischen Energie einer transversen und einer Vortexdomänenwand bestimmt wird, nicht notwendigerweise bei tiefen Temperaturen erreichbar ist. Zusätzlich zur Geometrieabhängigkeit zeigte eine genaue Analyse der experimentellen Daten Einflüsse von Materialeigenschaften, Defekten und der thermischen Aktivierung auf. Diese Einflüsse müssen berücksichtigt werden, um die Domänenwandbildung zu verstehen und eine zuverlässige Kontrolle der experimentell zugänglichen Zuständen zu gewährleisten, wie sie für Anwendungen benötigt wird. Um ein besseres Verständnis der Magnetisierungsmanipulation zu gewinnen, wurde die Wechselwirkung zwischen einem spinpolarisierten Strom und einem magnetischen Vortexzustand für verschiedene Dy Dotierungskonzentrationen in einem Mu-Metall untersucht. Daraufhin wurde eine kontrollierte Verschiebung der Kernregion des Vortexzustandes für bis zu vier verschiedene, jedoch energetisch identische Zustände beobachtet und die wirkenden Drehmomente separiert um den nicht-adiabatische Para-

meter, ξ, zu bestimmen. Die Messung wurde für verschiedene Dysprosiumkonzentrationen wiederholt und es zeigte eine Steigerung für ξ, der mit einer Erhöhung des unabhängig gemessenen Gilbert-Dämpfungsparameter, α, zusammenfällt. Das Verhältnis ξ zu α war im betrachteten Dotierungskonzentrationsbereich konstant and verhinderte daher höhere Domänenwandgeschwindigkeiten bei niedrigeren Stromdichten. Das hat zur Folge, dass effiziente "Spin-Transfer-Torque" und domänenwandbasierte Geräte nicht mit einer geringen Dy Dotierungskonzentration erreicht werden können und andere Herangehensweisen benötigt werden.

Abstract

The prevalent data storage devices today rely on a controlled magnetization modification of thin ferromagnetic films or elements on a nanometer scale. The traditional approach of Oersted field-induced magnetic switching combined with advances in magnetic sensing enabled an exponential increase in data density and proposed concepts predict further advances in this field. However, general read/write latency and random-access performance stagnated and the data storage device became a bottleneck in computer architecture. Subsequently, an increased interest in unexploited mechanisms led to the development of new concepts including the spin polarized current-induced manipulation of well-defined magnetic states. For instance, the racetrack memory device proposed by Parkin in 2008 employes the current-induced displacement of domain structures along thin and narrow magnetic wires. This requires first the investigation of suitable geometries where the spin configuration can be reliably tailored and controlled and secondly an understanding of the fundamental physical parameters that govern the magnetization dynamics under current excitations. In this thesis, we considered two expected requirements for domain wall-based spintronics and studied the stability of tailored domain wall states as well as effective approaches to change technologically relevant system parameters. First, we studied the controlled formation of magnetic domain walls in ferromagnetic rings made of iron for various sizes by varying the thickness and inner diameter in a regime relevant for devices using a high resolution scanning electron microscope with polarization analysis (SEMPA). Micromagnetic simulations at $0K$ were performed mimicking the nucleation process and accounting for the metastability of intermediate magnetic spin configurations. Accordingly, it has been shown that the lowest energy state determined by comparing the magnetostatic and exchange energy of a transverse and vortex domain wall configuration is not necessarily accessible at low temperatures. Furthermore, a careful analysis of the experimental data revealed that in addition to the geometry, the influence of materials properties, defects and thermal activation all need to be taken into account in order to understand and reliably control the experimentally accessible states, as needed for device applications. To further understand approaches of magnetization manipulation, the interaction of a spin polarized current with a flux-closure magnetic vortex state for variously doped Permalloy-alloys was studied. A controlled displacement of the well-defined vortex core region was observed for up to four different energetically identical magnetic states and the acting spin torque contribution was subsequently isolated to determine the non-adiabatic parameter, ξ. The measurement was repeated for different dysprosium dopant-concentrations and an increase in ξ concurrent with an increase in the independently measured Gilbert-damping parameter, α, was observed. However, ξ/α was constant within the studied dopant concentration range and thus faster domain wall motion at lower current densities as required for efficient spin transfer torque-driven domain wall-based devices can not be accomplished by a low Dy dopant concentration and has to be achieved with a different approach.

Contents

CHAPTER 1

Introduction

The vast majority of today's data storage industry relies on our understanding of magnetic media and our ability to reliably control the magnetic states within. Classically, Ampère's circuital law has been employed via Oersted fields generated by charge currents and consequently switch between two bistable magnetic states (labeled logical "0" and logical "1"). To meet the requirements of rapidly growing data storage and data-intensive computing, an increase in data density and throughput is necessary. In the past decades, the workhorse of magnetic recording, the hard disk drive (HDD), was steadily improved with regard to the areal density by employing the anomalous [1], the giant [2, 3] and the tunnel magnetoresistance [4] for the readout process while decreasing the physical size of the bistable magnetic bits. To ensure the long time stability of the stored data the energy barrier between the magnetic states is typically more than forty times larger than the thermal energy, $k_B T$, of the system. Since the necessary current density to write data increases with decreasing physical size of the magnetic state, further miniaturization becomes difficult beyond a certain point due to the detrimental effects of increased Joule heating.

Since the research focus has shifted from traditional magnetic field driven techniques to alternative concepts, e.g. employing spin currents in spintronics, a more favorable scaling behavior is possible. For functional spintronic devices highly spin polarized currents, well-defined device geometries and tailored magnetic states are required to control the dynamics of the magnetic state sufficiently. Furthermore, the materials properties of a system are one key factor and hence choosing a suitable device material is crucial and a detailed knowledge of the influence on the device performance is necessary.

This thesis investigates the dependence of the magnetic domain wall configuration on its geometrical confinement in planar wires and the interaction of a specific magnetic state with a spin polarized current to extract the non-adiabatic coupling strength while varying the doping level in the host material. We employ high resolution scanning electron microscopy with polarization analysis (SEMPA) to image magnetic states between and during manipulation of the embedded magnetic state.

The contents of the thesis are outlined below:

Chapter 1 introduces the theoretical background of stable magnetic states as well as the equations describing magnetization dynamics in field and spin polarized current-driven systems.

Chapter 2 presents a brief history of magnetic imaging techniques and introduces the main measurement system used in this work, the scanning electron microscope with polarization analysis (SEMPA).

Chapter 3 describes the employed techniques to fabricate nanoscale sample structures using a multistep electron beam lithography process combined with the thin film growth of simple metals and their alloys in an ultra high vacuum chamber.

Chapter 4 presents the characterization of magnetic domain wall spin configurations in geometrically confined structures and discusses the energetical stability as a function of the system size. We demonstrate the stability of symmetric transverse domain walls in narrow and thin ring structures by measurement and extensive micromagnetical simulations and observe a transition to asymmetric transverse and vortex domain wall states. The measurements suggest a qualitative agreement with the expected distribution of do-

main wall states and highlight the importance of the material properties, defects as well as the sample edge structure.

Chapter 5 extends considerations to spin polarized current-driven magnetic states and investigates the non-adiabatic coupling strength for Permalloy as a function of dysprosium dopant concentration by using a controlled displacement of the core region in a magnetic vortex state. The determined coupling strength is correlated to the Gilbert damping and demonstrates an avenue for tailoring dynamic parameters of the system.

Chapter 6 summarizes the conclusions of this work and presents suggestions for future projects based on the experimental results and recently performed modifications of the SEMPA setup.

CHAPTER 2

Introduction to Magnetism in Condensed Matter

2.1 Microscopic Origin of Magnetism

The investigation of magnetic materials is one of the oldest though liveliest fields in physics with the magnetic moment, $\boldsymbol{M}$, at its core. However, the specific origin of $\boldsymbol{M}$ is diverse and depends on the considered system. While further manifestations exists, many magnetic phenomena can be associated with dia-, para-, ferro-, ferri or antiferromagnetism. In particular, ferromagnetic materials are essential for widely used modern technologies including non-volatile data storage and electrical engines. The underlying microscopic elements are unpaired electrons which contribute to $\boldsymbol{M}$ through intrinsic magnetic moments associated to the electron spin and a magnetic moment associated with the orbital angular momentum of the electrons. Suitable interactions favour a parallel alignment of magnetic moments on neighboring atoms which mediate long-range order, e.g. the exchange interaction for overlapping wave functions of strongly localized electrons. In the case of weakly localized electrons an inbalance of the majority and minority spins can spontaneously occur if the Stoner criterion is fulfilled (see Fig. 2.1 (a)/(b)):

$$Ug(E_F) \geq 1$$

with U being a material dependent measure of the intraatomic Coulomb repulsion and the electron density of states, $g(E_F)$, at the Fermi energy, E_F [5]. This itinerant or band ferromagnetism introduced by Stoner [6] predicts ferromagnetism for the $3d$ transition-metals Fe, Co and Ni. Additional ferromagnetic single compound materials are found in the lanthanide series, e.g. Gd, Tb, Dy, Tm, Ho and Er. However, the ferromagnetic ordering temperature is significantly reduced compared to the mentioned ferromagnetic transition-metals and is below $\approx 290\,\mathrm{K}$ [8] with the dominant mechanism being the exchange interaction between strongly localized $4f$-subshells. The bulk magnetic states in the rare earth elements are more diverse than those observed in Fe, Co or Ni. Dysprosium, for instance, exhibits paramagnetic ($T > 179\,\mathrm{K}$), helical-antiferromagnetic ($179\,\mathrm{K} > T > 85\,\mathrm{K}$) and ferromagnetic ordering ($T < 85\,\mathrm{K}$) at different temperatures [9]. By alloying different elements, combinations of magnetic properties can be achieved which are inaccessible for single compound materials. The Fe_xNi_{1-x} alloy Permalloy exhibits a pronounced peak in the magnetic susceptibility at $x \approx 0.2$ [10] due to the proximity of minima in magnetocrystalline anisotropy [11] and magnetostriction [12]. Moreover, for an amorphous alloy of Permalloy and a rare earth element, shared $5d$ electrons establish an antiferromagnetic coupling between the $3d$ and $4f$ subshells of the two constituents [13, 14]. Due to a precessional motion of the magnetic moments in the $3d$ subshell in Py a time-dependent $3d$-$5d$-hybridization causes a Zeeman splitting and a delayed thermal redistribution of $4f$ electrons of the rare earth element occurs (see Fig. 2.1 (c)). As a consequence, the $5d$ electron distribution is locally changed which influences the $3d$-$5d$ interaction and subsequently counteracts the original dynamics of the $3d$ electrons, hence increasing the effective damping of the precessional motion of the $3d$ magnetic moments [13, 15, 16]. Here, we introduced an atomistic representation of the underlying magnetization dynamics, however, due to computational limitations the simulation of large scale magnetic structures requires approximations.
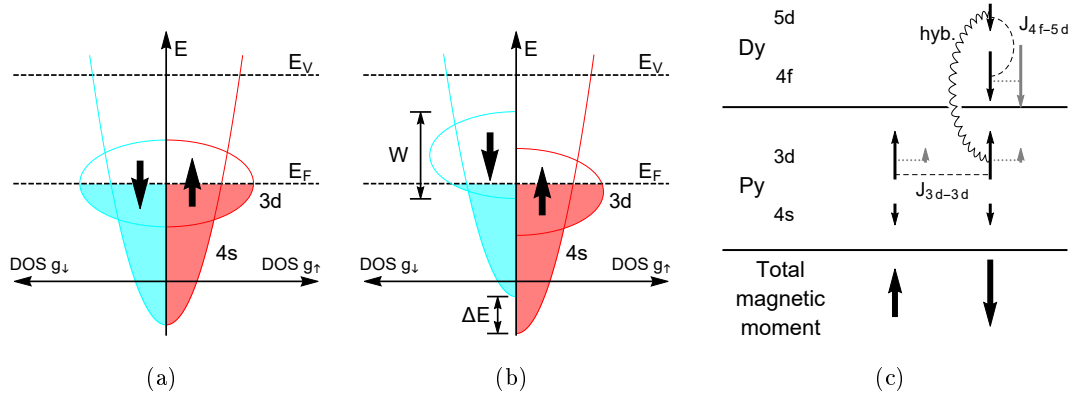
Figure 2.1: Schematics of partially populated electronic band structures in a non-magnetic material, (a), and in a ferromagnetic material, (b). The magnetic material exhibits an asymmetric population of the majority (up) and minority (down) bands leading to a net magnetic moment (up). Here, a relative shift of ΔE between the majority and minority bands enables a reduction of the total energy of the system favoring unequally populated electronic $3d$-subshells with width, W, in the absence of applied external fields. E_V additionally denotes the vacuum energy of the host material. (c) depicts the interaction between magnetic moments in a heavy-lanthanide Permalloy alloy. The intrinsic magnetic moments (thin black arrows) interact via exchange interactions of varying strength, J, and via hybridization. Specifically for Dysprosium with $L = 5$ an angular momentum contribution (gray arrows) to the magnetic moment exists and links to the spin via spin orbit interaction (dotted gray line). The total magnetic moment of a Py-Dy system is seen below indicating an alteration of the saturation magnetization as the Py-Dy-ratio changes (adapted from [7]).

2.2 Micromagnetic Description of Magnetism

In the following section, we will introduce the micromagnetic description of meso- and macroscopic ferromagnetic systems by approximating the atomistic Heisenberg Hamiltonian [17] which is based on localized magnetic moments, $\boldsymbol{M}$, definite at discrete positions, e.g. a cuboid lattice with fixed lattice constants. Considering only small misalignments between neighbouring magnetic moments a spatially continuous and sufficiently smooth magnetization, $\boldsymbol{M}(\boldsymbol{r})$, is introduced which enables the dominating magnetization contributions of a magnetic system to be determined more readily [18]. In particular, within the mean-field approximation of the Ginzburg-Landau theory, the zero temperature Landau free energy can be written as an integral over the energy density, ϵ [18]:

$$\mathcal{F}[\boldsymbol{M}] = \int_V \mathrm{d}r^3 \epsilon(\boldsymbol{M}(\boldsymbol{r}))$$
$$= \int_V \mathrm{d}r^3 (\epsilon_{Ex}(\boldsymbol{r}) + \epsilon_D(\boldsymbol{r}) + \epsilon_{Ani}(\boldsymbol{r}) + \epsilon_Z(\boldsymbol{r}))$$

with the exchange energy density, ϵ_{Ex}, the magnetostatic energy density, ϵ_D, the anisotropy energy density, ϵ_{Ani}, and the Zeeman energy density, ϵ_Z. Local minima of the Landau free energy [18] in the magnetic configuration space correspond to meta-stable states and transitions between meta-stable states can occur in the presence of magnetic excitations, e.g. driven by an external magnetic field [19] or a charge current [20][1]. The individual energy density contributions are integrated over the volume, V, of the magnetic system and will be discussed in the following. Examples of different magnetic configurations in a specific confined geometry will be given in section 2.3.

2.2.1 Exchange Energy

The first energy density contribution, ϵ_{Ex}, accounts for the exchange interaction between spins at discrete lattice sites. The exchange interaction has a quantum mechanical origin and thus depends on the shared wave function of the involved electrons. The imposed constraint of Pauli's exclusion principle permits only wave functions which are antisymmetric under the exchange of two electrons. Approximating the shared wave function by a product of the unperturbed single atom wave functions yields an expression for the exchange interaction constant which describes the energy difference of the parallel and antiparallel spin configuration of electrons associated to different lattice sites. The exchange interaction constant depends on the overlap of wave functions from atoms at distinct lattice sites and the Coulomb energy penalty associated with the exchange of electrons between the considered atoms. Here, we apply the usual restriction of a nearest neighbour interaction with strength, J. The total energy corresponding to the Heisenberg Hamiltonian of spins,

---

[1]In experimentally realized systems thermally-driven magnetic excitations can occur due to finite temperature [21]. These excitations are not included in the presented theoretical description and following analysis. However, thermal effects in magnetism are of interest and new approaches have been proposed to describe these systems theoretically [22].

$\boldsymbol{S}_i$, located on a cubic lattice with a constant lattice spacing, a, can be written as [23]

$$
\begin{aligned}
\mathcal{F}_{Ex} &= -\frac{J}{a^3} \sum_{i \neq j; n.n.} \boldsymbol{S}_i \cdot \boldsymbol{S}_j \\
&= -\frac{JS^2}{a^3} \sum_{i \neq j; n.n.} \cos^2 \phi_{ij} \\
&= +\frac{JS^2}{a^3 M_S^2} \sum_{i \neq j; n.n.} (|\boldsymbol{M}_i - \boldsymbol{M}_j|^2 - 2M_S^2).
\end{aligned}
$$

Here, we replaced each spin, $\boldsymbol{S}_i$, with the corresponding magnetic moment, $\boldsymbol{M}_i$, and used a cosine formula. After neglecting the constant contribution, we consider only positive exchange interaction constants, J, and approximate $\mathcal{F}_{Ex}$ with its continuum limit,

$$
\begin{aligned}
\mathcal{F}_{Ex} &\approx \int_V \mathrm{d}r^3 \frac{A}{M_S^2} |\boldsymbol{\nabla} \boldsymbol{M}(\boldsymbol{r})|^2 \\
&= \int_V \mathrm{d}r^3 \epsilon_{Ex}(\boldsymbol{r}). \tag{2.2.1}
\end{aligned}
$$

The derived expression assumes a change in the orientation of the magnetic moments on a length scale large compared to the lattice spacing, a. Thus, a sufficiently small misalignment between neighboring spins is assumed and a smooth magnetization, $\boldsymbol{M}(\boldsymbol{r})$, is subsequently introduced. Furthermore, we introduced the exchange stiffness, $A = JS^2/a$, and the saturation magnetization, $M_S = |\boldsymbol{M}(\boldsymbol{r})|$, and defined the exchange energy density

$$
\epsilon_{Ex}(\boldsymbol{r}) = \frac{A}{M_S^2} |\boldsymbol{\nabla} \boldsymbol{M}(\boldsymbol{r})|^2.
$$

Evidently, for $A \propto J > 0$ the lowest exchange energy is found for a spatially constant magnetization which is experimentally well-realized within single ferromagnetic domains. However, for $J < 0$ the magnetization configuration minimizing the energy of the Heisenberg Hamiltonian corresponds to antiparallel alignment of neighbouring magnetic moments, i.e. a large change in the orientation of magnetic moments on a length scale equal to the lattice spacing. Thus, equation 2.2.1 is not appropriate to describe an antiferromagnetic or a ferrimagnetic state.

2.2.2 Zeeman Energy

An additional energy contribution is the so-called Zeeman energy [18],

$$
\begin{aligned}
\mathcal{F}_Z &= \int_V \mathrm{d}r^3 (-\mu_0 \boldsymbol{M}(\boldsymbol{r}) \cdot \boldsymbol{H}(\boldsymbol{r})) \\
&= \int_V \mathrm{d}r^3 \epsilon_Z(\boldsymbol{r}),
\end{aligned}
$$

with μ_0 being the permeability of free space. The associated energy density, $\epsilon_Z(\boldsymbol{r})$, is linear in the applied external magnetic field, $\boldsymbol{H}(\boldsymbol{r})$. For sufficiently high magnetic fields the Zeeman energy is the dominant contribution to $\mathcal{F}$ and the magnetization locally aligns with $\boldsymbol{H}(\boldsymbol{r})$. For spatially constant magnetic fields, the Zeeman energy is independent of the sample geometry and is proportional to the dot product of the net magnetic moment of the sample, $\int_V \mathrm{d}r^3 \boldsymbol{M}(\boldsymbol{r})$, with the external magnetic field, $\boldsymbol{H}$.

2.2.3 Magnetostatic Energy

The above energy contributions are not explicitly sample geometry dependent, however, within the magnetic material Gauss's law [23],

$$\boldsymbol{\nabla} \cdot \boldsymbol{M}(\boldsymbol{r}) = -\boldsymbol{\nabla} \cdot \boldsymbol{H}_D(\boldsymbol{r}),$$

has to be fulfilled[2]. Here, the magnetization acts as a source of a demagnetization field, $\boldsymbol{H}_D$, with associated magnetic volume and surface charges, i.e. $-\boldsymbol{\nabla} \cdot \boldsymbol{M}(\boldsymbol{r})$ and $\boldsymbol{n}(\boldsymbol{r}) \cdot \boldsymbol{M}(\boldsymbol{r})$, respectively. Solving for $\boldsymbol{H}_D$ in the case of an arbitrary magnetization configuration in complex sample geometries requires a numerical approach [24], but for uniform magnetization in simple geometries like rectangular prisms and ellipsoids, analytical solutions are known [23, 25]. The demagnetization field interacts with the generating magnetization and demands an energy penalty of [23]

$$
\begin{aligned}
\mathcal{F}_D &= \int_V \mathrm{d}r^3 \left(-\frac{\mu_B}{2} \boldsymbol{M}(\boldsymbol{r}) \cdot \boldsymbol{H}_D(\boldsymbol{r}) \right) \\
&= \int_V \mathrm{d}r^3 \left(+\frac{\mu_B}{2} |\boldsymbol{H}_D|^2(\boldsymbol{r}) \right) \\
&= \int_V \mathrm{d}r^3 \epsilon_D(\boldsymbol{r}).
\end{aligned}
$$

Here, $\mathcal{F}_D$ can only be lowered by avoiding the creation of a demagnetization field, e.g. by reducing the magnetization divergence within the sample and the projection of the edge magnetization on the surface normal, $\boldsymbol{n}(\boldsymbol{r})$, of the sample. Consequently, specific magnetic states, possibly energetically degenerated, can be favourable for a given sample geometry, e.g. for certain diameter-thickness combinations disk-shaped Permalloy elements exhibit one out of four energetically degenerate remanent flux-closure domain structures [26, 27] called vortex states (a specific vortex state is shown in Fig. 2.2 (c)/(f))[3]. Due to its properties and origin the magnetostatic energy is also called dipolar or shape anisotropy energy [30].

2.2.4 Anisotropy Energy

Some materials exhibit an intrinsic anisotropy independent of the sample geometry, but due to the underlying crystal symmetry, i.e. the spatial arrangement of atoms influences the orientation as well as the population of the electron orbitals which subsequently influences the orbital angular momentum, $\boldsymbol{L}$ [30]. Hence, the crystal symmetry can effect the orientation of the electron spin, $\boldsymbol{S}$, if it couples to the orbital angular momentum via the spin-orbit interaction [30–32],

$$U_{SO} \propto \frac{Z}{r^3} (\boldsymbol{S} \cdot \boldsymbol{L}).$$

---

[2]The equation assumes the absence of an external magnetic field. The general case is described in [23].

[3]Additionally, small particles often exhibit simple magnetic domain states strongly influenced by the sample geometry. For a single domain state an upper ellipsoid particle size is given by Brown's fundamental theorem [28], e.g. in an iron particle with an axial ratio of 0.2 a critical size of $\approx 200\,\mathrm{nm}$ for monodomain states has been estimated [29].

Specifically, for magnetic materials with a hexagonal close-packed (hcp) crystal structure, e.g. Dysprosium[4], a uniaxial anisotropy [34],

$$\mathcal{F}_{Ani,u} = \int_V \mathrm{d}r^3 \left(\frac{K_{u1}}{M_S^2} (\boldsymbol{n} \cdot \boldsymbol{M}(\boldsymbol{r}))^2 + \frac{K_{u2}}{M_S^4} (\boldsymbol{n} \cdot \boldsymbol{M}(\boldsymbol{r}))^4 \right)$$
$$= \int_V \mathrm{d}r^3 \epsilon_{Ani,u}(\boldsymbol{r})$$

is observed. The preferred magnetization orientation in the presence of such an anisotropy depends on the relative sign and ratio of the coefficients K_{u1} and K_{u2}. Nonetheless, for two negative coefficients the magnetic moments align with $\boldsymbol{n}$ and if both coefficients are positive magnetic moments favour a perpendicular orientation to $\boldsymbol{n}$ which allows for anisotropy energy penalty-free continuous magnetization rotations around the symmetry axis. However, a face or body centered cubic (fcc/bcc) crystal structure reduces the rotational symmetry further [35] prohibiting such a continuous energy penality-free rotation around any fixed direction. Here, lowest-order terms contributing to the Landau free energy are [18]:

$$\mathcal{F}_{Ani,c} = \int_V \mathrm{d}r^3 \left(\frac{K_{c1}}{M_S^4} (M_1^2(\boldsymbol{r}) M_2^2(\boldsymbol{r}) + M_1^2(\boldsymbol{r}) M_3^2(\boldsymbol{r}) + M_2^2(\boldsymbol{r}) M_3^2(\boldsymbol{r})) \right.$$
$$\left. + \frac{K_{c2}}{M_S^6} M_1^2(\boldsymbol{r}) M_2^2(\boldsymbol{r}) M_3^2(\boldsymbol{r}) \right)$$
$$= \int_V \mathrm{d}r^3 \epsilon_{Ani,c}(\boldsymbol{r}).$$

Although typical representatives are nickel (fcc) and iron (bcc), the effective anisotropy for polycrystalline thin films of the two materials and their alloys is small for systems which are sufficiently large compared to the average grain size, provided that the individual grains are randomly orientated [36]. In particular, the cubic anisotropy of $Fe_x Ni_{1-x}$ shows a minimum for $x \approx 0.2$ (as mentioned in section 2.1). Nevertheless, a uniaxial anisotropy is induced under certain deposition conditions[5] for example due to magnetostriction [38].

2.2.5   Effective Magnetic Field and Brown's Equation

We introduced the Landau free energy contributions appropriate to our material systems and associated the local energy minima with metastable magnetic states; nevertheless, to derive possible metastable states a suitable equation has to be inferred. By observing the effect of infinitesimal magnetization changes, $\delta \boldsymbol{M}(\boldsymbol{r})$, on the energy and ensuring the magnetization normalization, $|\boldsymbol{M}(\boldsymbol{r}) + \delta \boldsymbol{M}(\boldsymbol{r})|^2 = M_S^2 + 2[\boldsymbol{M}(\boldsymbol{r}) \times \delta \boldsymbol{M}(\boldsymbol{r})] = M_S^2$, Brown's equations [39],

$$0 = [\boldsymbol{M}(\boldsymbol{r}) \times \boldsymbol{H}_{eff}(\boldsymbol{r})] \qquad\qquad \forall \boldsymbol{r} \in V \qquad\qquad (2.2.2)$$
$$0 = [\boldsymbol{M}(\boldsymbol{r}) \times (\boldsymbol{n}(\boldsymbol{r}) \cdot \boldsymbol{\nabla}) \boldsymbol{M}(\boldsymbol{r})] \qquad\qquad \forall \boldsymbol{r} \in \partial V \qquad\qquad (2.2.3)$$

---

[4]The observed crystal structure of the helical-antiferromagnetic ordering is hcp, but below the first-order ferromagnetic transition at $85\,\mathrm{K}$ the crystal structure is orthorhombic [33].

[5]By adding a small molybdenum content to the alloy the cubic anisotropy and the magnetostriction can simultaneously be minimized preventing a uniaxial anisotropy [37].

for the stability of a state are derived with the second equation being valid on the sample surface, ∂V. Here, the effective magnetic field,

$$\boldsymbol{H}_{eff}(\boldsymbol{r}) = -\frac{1}{\mu_0}\frac{\delta\mathcal{F}}{\delta\boldsymbol{M}}(\boldsymbol{M}(\boldsymbol{r}))$$
$$= \frac{2A}{\mu_0 M_S^2}\boldsymbol{\nabla}^2\boldsymbol{M}(\boldsymbol{r}) + \boldsymbol{H}_D(\boldsymbol{r}) - \frac{1}{\mu_0}\frac{\delta\mathcal{F}_{Ani}}{\delta\boldsymbol{M}}(\boldsymbol{M}(\boldsymbol{r})) + \boldsymbol{H}(\boldsymbol{r}),$$

is introduced and for an unstable equilibrium or a metastable state the local magnetization points along the axis defined by $\boldsymbol{H}_{eff}(\boldsymbol{r})$. Incidentally, $\boldsymbol{H}_{eff}$ characterizes the typical length scale of magnetization variations, e.g. for magnetostatic $(l_{Ex} = \sqrt{A/(\mu_0 M_S^2/2)})$ and anisotropy $(l_{Ani} = \sqrt{A/K_{Ani}})$ dominated systems [18, 40]. A closer inspection of metastable magnetic states and the dynamics which lead to equilibration of states is given in chapter 4 and in section 2.4.

2.3 Magnetic Domains and Domain Walls

The lowest energy state of a magnetic system depends on the material and the sample geometry as well as the applied external magnetic field. Usually, a simultaneous minimization of every energy contribution can not be accomplished and multiple metastable or degenerate states exist. In an exchange interaction dominated system, one or multiple sample regions exist, commonly known as domains, in which the magnetic moments align along one direction, however, with specific directions favored in systems with anisotropy and/or magnetostatic energy. For thin film samples of common materials like nickel, iron and their alloys, the magnetization preferably aligns parallel to the film plane to reduce the magnetostatic energy [28]. Adding geometrical restrictions by structuring the film sample effects the in-plane orientation of the magnetization, particularly at the lateral structure edges, e.g. by stabilizing flux-closure states such as the four-domain Landau states (see Fig. 7.3) or Vortex states (see Fig. 2.2 (f)) found in appropriately sized rectangular or disk shaped elements, respectively [42]. The influence of different energy contributions is illustrated in Fig. 2.2. The transition region between neighboring domains, the domain wall, mediates the magnetization rotation at the expense of exchange, anisotropy and magnetostatic energy. In particular, for sufficiently thin (unstructured) soft magnetic films balancing the energy contributions leads to the formation of distinct domain wall types such as Néel, Cross-Tie and Bloch walls (see Fig. 2.3 and Fig. 4.1) in Permalloy films of increasing thickness [18, 43]. A Bloch wall is characterized by a magnetization rotation parallel to the domain wall plane, whereas the magnetization rotation in a Néel wall occurs perpendicular to said plane. Following Jakubovics [18, 44], the corresponding domain walls widths can be defined based on the magnetic flux profile. Here, a film is considered thin if its thickness is comparable or smaller than the materials associated Bloch wall width.

In chapter 4, we take a closer look at the preferred remanent spin structures in iron rings after saturating the system in an external magnetic field, $\boldsymbol{H}$.
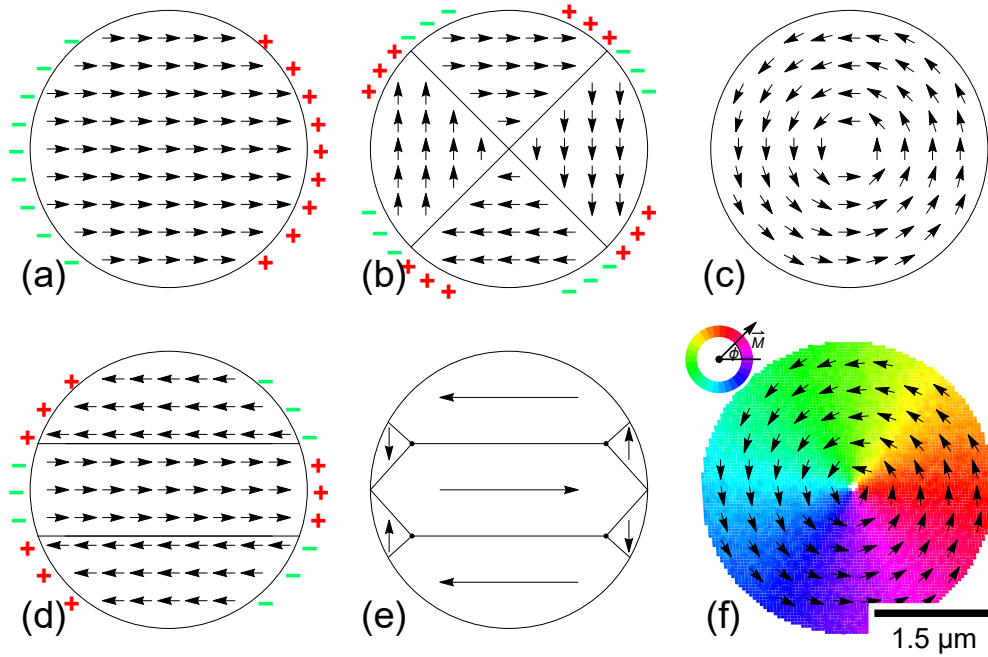
Figure 2.2: Remanent magnetic states in thin disk structures with the exchange [(a)], anisotropy [(b)/(d)] and the magnetostatic energy [(c)] being minimized. The states in (b)/(d) are energetically favourable for a cubic or uniaxial anisotropy, respectively. (e) shows reduced surfaces charges due to the formation of a flux-closure state. Lateral areas with a notable magnetic surface charge are indicated with $+/-$. (f) in-plane spin structure of a magnetic vortex state in a thin structure measured with SEMPA resembling (c). Close to the disk center a reduction of the in-plane magnetization five times higher than the noise-level, σ, indicates a magnetic-flux through the sample surface (white cross). Adapted from [41].
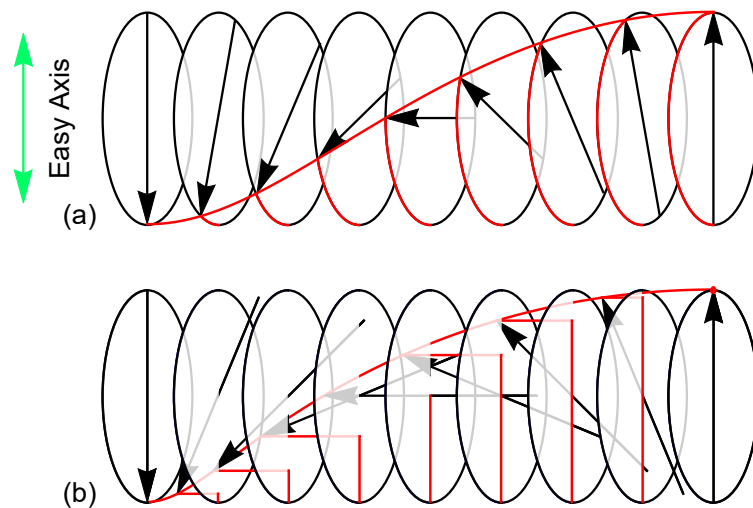

Figure 2.3: Schematics of the magnetization rotation within (a) a Bloch domain wall and (b) a Néel domain wall in a system with an magnetic easy axis along the indicated direction.

2.4 Magnetization Dynamics and Micromagnetic Simulations

In section 2.2.5, the effective magnetic field, $\boldsymbol{H}_{Eff}$, and the equilibrium conditions were introduced, however, no dynamical description of the equilibration process was given. In particular, for a magnetic field sweep-induced nucleation a detailed understanding of the previous history of the magnetic system is required to distinguish between metastable, possibly energetically degenerate, states and select the equilibrium state. Further complications arise for the description of temperature-induced effects on magnetization, which lie beyond the scope of this work and which are themselves an active field of research [22], however, we consider spin current-induced magnetization modifications. In the following, we look at the governing equation of motion and discuss the current-induced motion of a Bloch-domain wall.

2.4.1 Landau-Lifshitz-Gilbert Equation

Landau and Lifshitz introduced an equation describing the precession of a magnetic moment, $\boldsymbol{M}$, in a magnetic field, $\boldsymbol{H}$, with a subsequent aligning of $\boldsymbol{M}$ with $\boldsymbol{H}$ [45]:

$$\frac{d\boldsymbol{M}}{dt} = -\gamma_0 [\boldsymbol{M} \times \boldsymbol{H}_{Eff}] - \frac{\alpha_{LL}}{M_S^2} [\boldsymbol{M} \times [\boldsymbol{M} \times \boldsymbol{H}_{Eff}]]. \qquad (2.4.1)$$

with the gyromagnetic ratio, γ_0, $\boldsymbol{H}$ replaced by the effective field and the damping parameter, α_{LL} which is assumed to satisfy $\alpha_{LL} \ll \gamma M_S$. The precession of the magnetic moment occurs with a frequency of $\gamma_0|\boldsymbol{H}_{Eff}|$ while relaxing within a time $\tau = (\gamma\alpha_{LL}|\boldsymbol{H}_{Eff}|)^{-1}$. A modification was proposed by Gilbert who derived the equation of motion in a Lagrange formalism and introduced a Rayleigh dissipation function which leads to an alternative formulation [46]:

$$\frac{d\boldsymbol{M}}{dt} = -\gamma_{LLG} [\boldsymbol{M} \times \boldsymbol{H}_{Eff}] + \frac{\alpha_{LLG}}{M_S} [\boldsymbol{M} \times \frac{d\boldsymbol{M}}{dt}]$$

with the parameter α_{LLG} being assumed to be small compared to $\gamma_{LLG} M_S$. It becomes apparent that the two equations are closely related, however, the gyromagnetic ratio, $\gamma_0(1 + \alpha_{LLG}^2) = \gamma_{LLG}$, has to be renormalized. Figure 2.4 illustrates a relaxation process of a magnetic moment and indicates the direction of the acting torques. Micromagnetics,

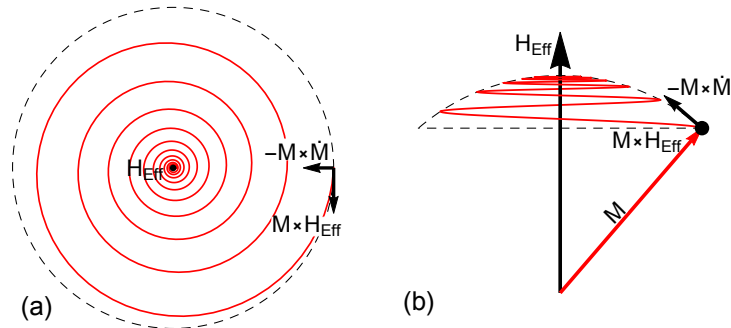Figure 2.4: Precession of a magnetic moment, $\boldsymbol{M}$, around an effective field, $\boldsymbol{H}_{Eff}$, and subsequent relaxation towards the $\boldsymbol{H}_{Eff}$. The direction of the acting torques can be seen from the top, (a), and from the side, (b).

specifically the micromagnetic simulator used in this work [47], relies on the Landau-Lifshitz-Gilbert (LLG) equation. Extra terms are needed to describe current-induced excitations. The first missing ingredient, the adiabatic spin-torque interaction, $\boldsymbol{T}_{Ad}$, with a spin current, was introduced by Berger [48] and by Slonczewski [49] and subsequent measurements suggested the validity of this contribution [40, 50]. The torque describes an adiabatic aligning of the intrinsic magnetic moments of $4s$ conduction electrons in slowly varying magnetic structures, e.g. domain walls [48]. This interaction excludes the reflection of electrons and thus a second missing ingredient, the non-adiabatic spin transfer torque, $\boldsymbol{T}_{Non-Ad}$, was introduced [51] which accounts for spin-flips of $4s$ conduction electrons at nonuniform magnetic structures and acts perpendicular to the adiabatic torque. To illustrate the behaviour of the extended Landau-Lifshitz-Gilbert equation[6] [51],

$$\frac{d\boldsymbol{M}}{dt}(\boldsymbol{r}) = -\gamma[\boldsymbol{M}(\boldsymbol{r}) \times \boldsymbol{H}_{Eff}(\boldsymbol{r})] + \frac{\alpha}{M_S}[\boldsymbol{M}(\boldsymbol{r}) \times \frac{d\boldsymbol{M}}{dt}(\boldsymbol{r})] \qquad (2.4.2)$$

$$\underbrace{-\frac{1}{M_S^2}[\boldsymbol{M}(\boldsymbol{r}) \times [\boldsymbol{M}(\boldsymbol{r}) \times (\boldsymbol{u} \cdot \boldsymbol{\nabla})\boldsymbol{M}(\boldsymbol{r})]]}_{=\,\boldsymbol{T}_{Ad} \text{ with } \boldsymbol{u} = \mu_B P \boldsymbol{j_e}/eM_S} \qquad (2.4.3)$$

$$\underbrace{-\frac{\xi}{M_S}[\boldsymbol{M}(\boldsymbol{r}) \times (\boldsymbol{u} \cdot \boldsymbol{\nabla})\boldsymbol{M}(\boldsymbol{r})]}_{=\,\boldsymbol{T}_{Non-Ad}}, \qquad (2.4.4)$$

the spin current-induced motion of a domain wall is described. Here, a charge current, $\boldsymbol{j_e} = eM_S\boldsymbol{u}/\mu_B P$, with spin polarization, P, acts on a transverse domain wall in a thin wire [52] and moves it, after initial acceleration, with terminal velocity towards the current source. Above a critical current density, the previously monotonic terminal motion becomes periodic and a domain wall oscillation as well as transformation can be observed [53]. An analytical solution below the so-called Walker breakdown predicts $v_{DW} = (\xi/\alpha)u$ while the maximum domain wall velocity scales with $\alpha/|\xi - \alpha|$ [52, 54]. Generally, however, this equation is solved numerically, e.g. via a finite difference method. In the case of a field sweep-induced domain wall nucleation the energy of the system is minimized iteratively and the highest angular velocity observed for the magnetic moments within the sample is compared to a preset value defined as the highest angular velocity acceptable for a sufficiently converged magnetic system which approximately fulfills Brown's equations of equilibrium 2.2.2.

In chapter 5, we take another look at domain wall dynamics and consider specific cases. Furthermore, we will determine the non-adiabatic coefficient, ξ, for undoped as well as for dysprosium-doped Permalloy.

---

[6]For convenience, we remove the indices from the gyromagnetic ratio, γ_{LLG}, and the damping parameter, α_{LLG}.
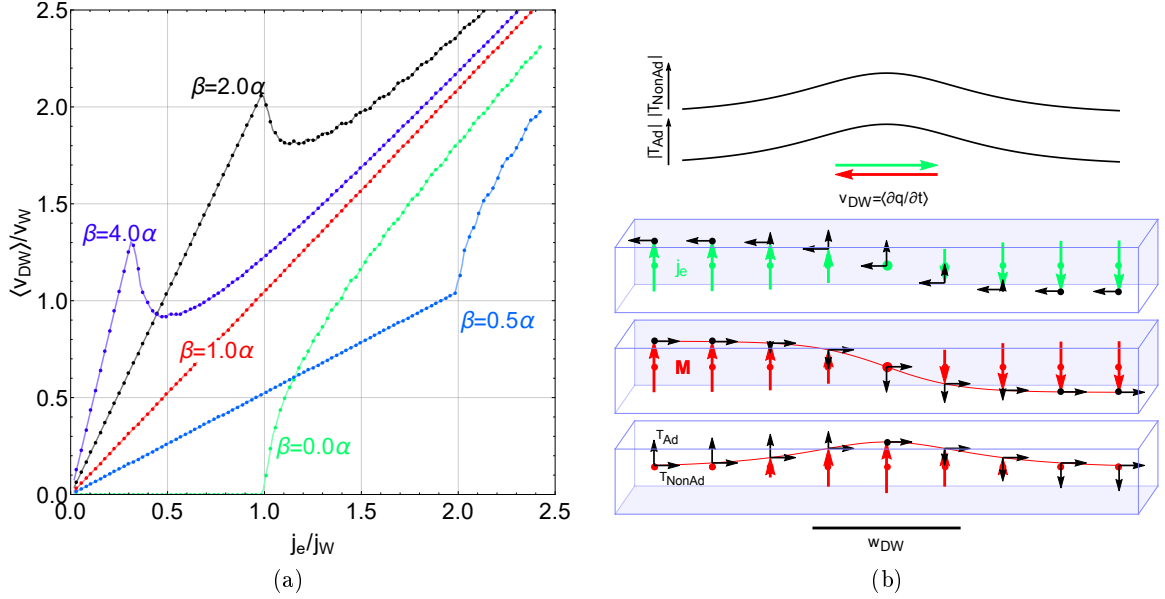
Figure 2.5: (a) Normalized average velocity, $\langle v_{DW} \rangle$, of a current-driven domain wall structure assuming a constant domain wall width, w_{DW}, for different non-adiabaticity coefficients, ξ, and a damping of $\alpha = 10^{-2}$. The instantaneous domain wall velocity, v_{DW}, of an initially resting magnetic structure was derived by solving the Landau-Lifshitz-Gilbert equation for a one-dimensional transverse domain wall profile [54] numerically and simulating a time span of $8 \cdot 10^{-6}$ s. Subsequently, v_{DW} is averaged over the last $5 \cdot 10^{-6}$ s of the simulated system time. Here, we assumed $M_s = 1.7 \cdot 10^6$ A/m, $A = 2.1 \cdot 10^{-11}$ J/m and $K_{Ani} = 46.8 \cdot 10^3$ J/m^3 as well as a spin current polarization of $P = 0.5$. Below the Walker breakdown a steady domain wall motion is achieved and the slope of the domain wall velocity is strongly correlated to ξ while above a ξ-dependent critical current a periodic transformation of the domain wall structure is observed, causing partially compensated average domain wall motion. Notably, no domain wall motion appears below a critical current for $\xi = 0$ and strikingly for $\xi = \alpha$ the domain wall shape stays unaltered at any current density and no Walker breakdown occurs. (b) shows the influence of a spin-polarized charge current, j_e, on a Bloch domain wall [52] in a wire from different angles (corresponding sides are shaded). The direction of the acting torques on a magnetic moment, $\boldsymbol{M}$, and the current are indicated by black arrows with the relative strength displayed above. The adiabatic and non-adiabatic torques are derived for the specific spin structure using equation 2.4.3 and equation 2.4.4, respectively.

CHAPTER 3

Experimental Methods

3.1 Imaging of Magnetic Samples

The invention of various experimental techniques for the observation of domain and domain wall structures was a prosperous field during the last century. Many techniques were established, based on different interactions, which probe different system properties. In 1931, Bitter [55] demonstrated the use of colloids to exploit the stray field coupling between magnetic particles and a magnetic sample. Later improvements drastically increased the stray field sensitivity and the spatial resolution by tailoring the shape, size and magnetic state of the colloids, enabling imaging of minute details below $\sim 80\,\mathrm{nm}$ [56–58]. However, the Bitter method has limited applicability for strictly in-plane magnetized materials and the visibility varies between domain walls of different types, e.g. colloids accumulate preferably at Bloch instead of at Néel walls. Nowadays, a wide range of accompanying and complementary techniques are available, e.g. magnetic force microscopy (MFM) [18] and Lorentz force microscopy [59] which are sensitive to magnetic-flux, magneto-optical methods like Kerr microscopy as well as the element specific X-ray magnetic circular dichroism (XMCD)-based scanning transmission X-ray microscopy (STXM) [60] and photoemission electron microscopy (PEEM) [61]. The magnetic surface sensitivity of the listed methods ranges from $\sim 10\,\mu\mathrm{m}$ down to a couple of nm. However, additional techniques are available which probe the configuration and the spin polarization of the electronic structure of atoms in solids by utilizing unpolarized high energy electron beams. Figure 3.1 (a) illustrates one possible sequence of events starting with an unpolarized primary electron beam (PE) which is inelastically scattered at an inner-shell electron. Here, an electron (SE) is excited from a bound state to a continuum state and creates an inner-shell vacancy which is subsequently filled by an electron from a higher-shell. Due to the Auger effect [62] a second electron, the Auger electron (AE), is excited and leaves the atoms[1]. Both the secondary electron and the Auger electron can excite further electrons with lower energies until the initial electron is thermalized or escapes the solid [64]. Before escaping through the surface of the solid, the secondary electrons undergo multiple elastic electron-electron scattering events for which a minority spin electron above the Fermi energy preferably switches with a majority spin electron before the later escapes [65–67]. By detecting the spin polarization of the expelled electron, the magnetization of the area from which it originates can be inferred. Furthermore, the primary electron beam generates a backscattered electron beam (BSE) if it is deflected in the electric field of the nucleus, producing bremsstrahlung, γ_B [68]. Figure 3.1 (b) shows the situation on a macroscopic scale with the primary electron beam entering the sample and afterwards being deflected within the sample. Here, in particular, the beam direction gets reversed and the backscattered beam (BSE) breaks through the sample surface. Secondary electrons generated in a thin layer under the surface within a depth of the material-dependent average spin attenuation length, λ, can escape the solid with their spin polarization intact. They can originate both from areas close to the entry point of the primary beam and the exit point of the backscattered beam. Specifically for the primary beam the area depends on the beam diameter at the point of entry. On the other hand, due to the energy and material dependent stochastic deflection of the primary beam within the sample, the effective area from which the backscattered beam can penetrate the surface is considerably larger [69]. Furthermore, due to the lower energy of the backscattered electrons more secondary electrons ($\mathrm{SE_{II}}$) are generated close to the exit point [69] than close to the entry point which

---

[1] Energy-dispersive X-ray (EDX) spectroscopy uses the alternatively emitted element-specific X-ray radiation to determine the material composition [63].
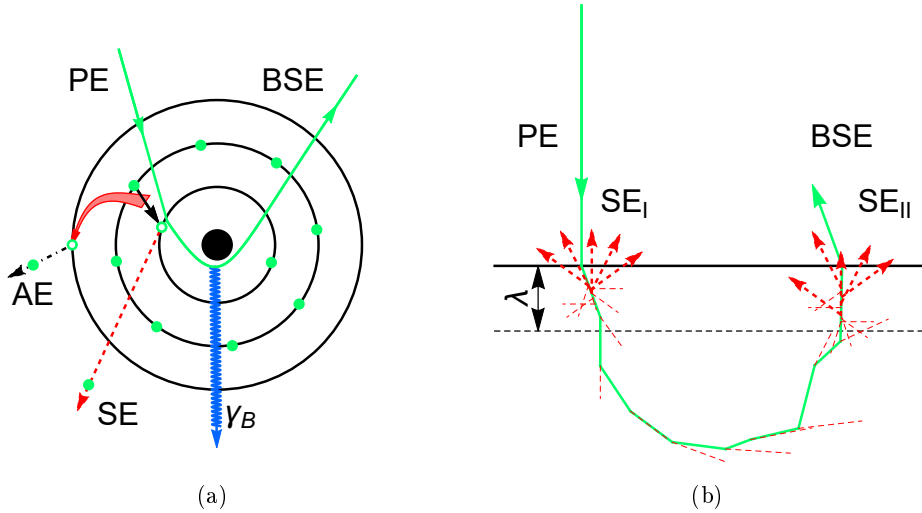
18

(a)   (b)

Figure 3.1: (a) shows the electronic structure of an atom as well as possible excitations due to an unpolarized primary electron beam (PE). Here, an Auger electron (AE) is emitted from the atom after PE scatters inelastically at an inner-shell electron which gets excited into a continuum state as a so-called secondary electron (SE). Furthermore, PE generates bremsstrahlung, γ_B during deflection in the electric field of the nucleus. (b) exemplifies one possible deflection of the primary electron in a sample as well as the backscattered beam (BSE). Secondary electron generated in an element dependent sample depth, λ, can escape through the sample surface with their spin polarization intact.

can significantly reduce the spatial resolution of a technique which uses these electrons for imaging such as SEMPA as outlined in the following paragraph [70, 71]. Here, the SE_I-SE_{II} ratio depends on the energy of the primary electron beam as well as the host material, e.g. SE_{II} are the dominating contributuion for gold at primary beam energies above $10\,\mathrm{keV}$ [69]. For the common magnetic materials Fe and Ni the reported attenuation lengths are $\sim 0.6 - 0.8\,\mathrm{nm}$ [72, 73] and $\sim 1.1\,\mathrm{nm}$ [72], respectively.

This work relies on scanning electron microscopy with polarization analysis (SEMPA) which exhibits a very high surface sensitivity of $\sim 1\,\mathrm{nm}$ combined with a high spatial resolution [71, 74]. The low magnetic probing depth can be attributed to the mean free path, λ, of the detected low energy secondary electrons in solids [74]. While a change in the accepted energy range of the detected secondary electrons affects the magnetic depth sensitivity only slightly [75] a larger effect is observed for the lateral resolution and electron spin polarization [70]. Thus, the accepted energy range has to be carefully balanced. Historically, a possible spin polarization, P, of surface emitted secondary electrons was hypothesized in 1930 [76] and subsequently observed for europium oxide in 1976 with a reasonably high $P = 32\,\%$, whereas the exciting primary electron beam was unpolarized [77]. This observation and the availability of appropriate scanning electron microscopes (SEMs) triggered the construction of the first SEMPA in 1984 [78]. In the following years, the measurement system itself has been characterized in detail [70, 79–81] which influenced the design of newer systems with greatly increased spatial resolution of the surface magnetization of up to $\sim 5\,\mathrm{nm}$ [71]. However, our commercial Scienta-Omicron SEMPA setup (see Fig. 3.2) is capable to resolve magnetic features down to at least $\sim 35\,\mathrm{nm}$ [82] restricted to two orthogonal, preferably in-plane, magnetization components. A modification of the
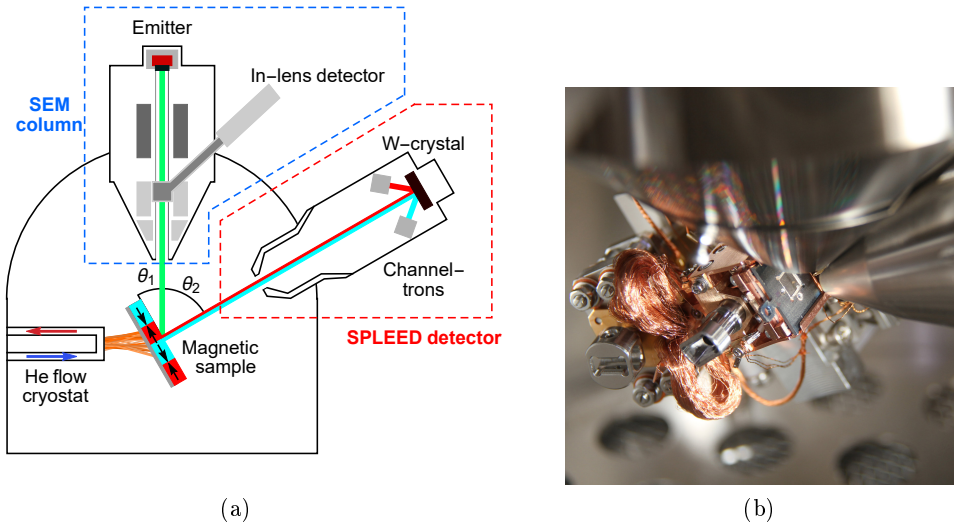
(a) (b)

Figure 3.2: (a) Schematic of our SEMPA setup shows the position of the SEM column, the magnetic sample and the SPLEED detector with relative angles of $\theta_1 \approx 26°$ [70] and $\theta_1 + \theta_2 = 90°$. The SPLEED detector consists of four Channeltron detectors, of which two are depicted here, positioned at the $(2,0)$ low energy electron diffraction spots of the tungsten crystal with a (100) surface. The relative Channeltron count rates are correlated to the surface magnetization of the sample. Incoming secondary electrons are accelerated in an electric potential of $\approx 102.5\,\mathrm{V}$ [70] and subsequently scattered on the crystal. The surface contamination on the tungsten crystal is regularly removed between measurements. In addition, a helium flow cryostat is available for cooling the sample down to temperatures of $\approx 25\,\mathrm{K}$ and for dissipating the heat generated during current-induced magnetization modification measurements. Attached to this primary chamber is a electromagnet at an off-stage position allowing either the application of a magnetic field of up to $\approx 180\,\mathrm{mT}$ within a fixed $2d$-plane or up to $\approx 5\,\mathrm{mT}$ along the perpendicular axis. A second chamber provides an argon ion gun for in-situ surface cleaning and three electron beam evaporators for the thin film deposition of simple metals including iron. (b) shows the sample stage in the measurement position with the SEM column at the top while the SPLEED detector approaches the sample from the right. The helium flow cryostat is attached at the backside of the sample stage.

secondary electron optics found in other setups enables the third orthogonal magnetization component to be captured [71, 83]. Furthermore, all SEMPA setups have in common that a topography image is acquired during the magnetization measurement which is useful for later feature correlation.

3.2 Origin of Spin Polarized Electrons and Their Detection

The typical primary electron acceleration voltages employed by our SEMPA setup are between $3-15\,\mathrm{kV}$ which is sufficient to excite the inner electronic structure of the material (see Fig. 3.1 (a)). In addition to other possible excitations, secondary electrons are created and undergo spin dependent scattering within the sample material [66, 84]. Here, electrons in an energy range, W, directly above the vacuum energy, E_V, experience a pronounced spin filtering [84]. Due to the band structure, electrons with a minority-spin character are less likely to elastically scatter with electrons of the minority band and excite majority band electrons above E_V, while electrons with an energy of E_V or less are themselves trapped and do not contribute to the secondary electrons. On the other hand, primary majority spin character electrons are scattered at other electrons with a lower efficiency and can escape the material [66, 84, 85]. The resulting spin polarization of the escaped low-energy secondary electrons is greatly enhanced and peaks for $3d$-transition metals at $E_{SE} < 10\,\mathrm{eV}$ [66, 85, 86]. For higher energies, the polarization expected from band structure considerations agrees well with the observed properties of escaped electrons [66, 84, 85]. However, only secondary electrons within a distance of the material dependent spin attenuation length, λ, to the surface can escape with enhanced spin polarization and be detected (see Fig. 3.1 (b)) [66]. Coincidentally, the escape rate of these low energy secondary electrons is higher than at higher electron energies which increases their relative importance to the yield [69].

3.2.1 Spin Dependent Separation of Secondary Electrons

To infer information from the escaping secondary electrons a spin dependent selection process is employed to separate the minority and majority character-like electrons carrying the magnetization information from the surface layer. In 1929, Mott proposed [87] that an electron moving in the vicinity of an atomic nucleus with atomic number, Z, experiences a spin-orbit interaction [32],

$$U_{SO} \propto \frac{Z}{r^3}(\boldsymbol{S} \cdot \boldsymbol{L}),$$

and the Mott-detector was developed on which the first operational SEMPA system was based [88]. Alternative detectors rely on low-energy diffusive scattering (LEDS) [89], low-energy electron diffraction (LEED) [90] and, more recently, the spin dependent scattering on oxidized iron thin films (FERRUM) [91]. The efficiency, κ, of the Mott-, LEDS-, and LEED-detectors is low and a long acquisition time is required to reach a signal-to-noise ratio comparable to a conventional SEM topography image [70]. A careful characterization of a LEED detector, identical to the one used in our SEMPA setup, suggests $\kappa \approx 1.6 \cdot 10^{-4}$ for a (100) tungsten surface at a scattering energy of $104.5\,\mathrm{eV}$. The magnetization is subsequently derived from the asymmetry in the measured count rates at the $(2,0)$ LEED spots of the crystal. Here, we will follow the discussion for a partially polarized beam of spin-$1/2$ particles and the Pauli vector, $\boldsymbol{\sigma}$, provided by Kirschner [32]: The electron beam can be described by a spin density matrix,

$$\rho = \sum_n (\alpha_1^{(n)}, \alpha_2^{(n)})^{\top} (\alpha_1^{(n)*}, \alpha_2^{(n)*}) = \sum_n |\chi^{(n)}\rangle \langle \chi^{(n)}|,$$

with the pure spin states $|\chi^{(n)}\rangle = (\alpha_1^{(n)}, \alpha_2^{(n)})^\top$. The spin polarization, P_i, of the given ensemble with respect to the Pauli matrix, σ_i, is by definition

$$P_i = \frac{tr(\rho\sigma_i)}{tr(\rho)} = \frac{\sum_n \langle \chi^{(n)} \sigma_i \chi^{(n)} \rangle}{\sum_n (|\alpha_1^{(n)}|^2 + |\alpha_2^{(n)}|^2)}.$$

For instance, assuming a pure state ($n = 1$) and σ_z the expression yields

$$P_z = \frac{|\alpha_1|^2 - |\alpha_2|^2}{|\alpha_1|^2 + |\alpha_2|^2} = \frac{N_\uparrow - N_\downarrow}{N_\uparrow + N_\downarrow},$$

with $|\alpha_{1/2}|^2$ being the probabilities to find an electron of spin $\pm\hbar/2$. For a measurement over a large number of electrons described by the pure spin state, this directly corresponds to the number of counts, $N_{\uparrow/\downarrow}$, for the respective spin directions. Getting back to the original expression, since $\sigma_{i i=x,y,z}$, form a basis the density matrix can be stated as

$$\rho = \frac{1}{2} tr(\rho)(\mathbb{1} + \boldsymbol{P\sigma}).$$

After a measurement time, T, our system provides four mean count rates, $I_i = N_i/T$, obtained at two orthogonal pairs of LEED spots with the tungsten crystal facing the magnetic sample, i.e. the two orthogonal quantization axes imposed by the crystal capture the in-plane magnetization information, however, each individual LEED spot receives electrons both due to magnetization and topography. A correct combination of I_i yields the polarizations [70],

$$P_x = \frac{1}{S} A_x = \frac{1}{S} \frac{I_{(2,0)} - I_{(\overline{2},0)}}{I_{(2,0)} + I_{(\overline{2},0)}} \qquad P_y = \frac{1}{S} A_x = \frac{1}{S} \frac{I_{(0,2)} - I_{(0,\overline{2})}}{I_{(0,2)} + I_{(0,\overline{2})}}, \qquad (3.2.1)$$

proportional to the surface magnetization of the sample with an energy and scattering angle dependent detector sensitivity, S, of ≈ -0.27 at $E \approx 104.5\,\text{eV}$. However, only the measured electron count rates, I_i, are directly accessible as well as the derived asymmetries A_x and A_y. Specifically for our measurement system a beam of secondary electrons from the sample reaches the tungsten crystal with a rate of I is only partially diffracted into the LEED spots [70]. Thus, the total Channeltron count rate, $RI = I_{(2,0)} + I_{(0,2)} + I_{(\overline{2},0)} + I_{(0,\overline{2})}$, is reduced by the limited reflectivity, $R \approx 0.0011$ [70], of the tungsten crystal. Here, the expected polarization follows a Poisson distribution with a width which increases according to $(RITS^2)^{-1/2}$ for a fixed measurement time, T. The corresponding figure-of-merit [70], κ, is

$$\kappa = 2RS^2 \approx 1.6 \cdot 10^{-4}.$$

Thus, to reach a signal-to-noise equal to that of a common SEM image SEMPA has to significantly increase the measurement time. Therefore, a considerable effort has been put into refining the spin detector both in terms of the figure-of-merit and the number of accepted secondary electrons [70, 71, 91, 92], but it remains an inherent limitation of SEMPA. In the following section, we take a look at surface magnetizations found in thin films and in whiskers.

3.2.2 SEMPA Imaging Example and Experimental Restrictions

In the previous section, we described how SEMPA determines magnetization for a single source, i.e. a small area. Hence, to determine a spatially varying magnetic state on a larger
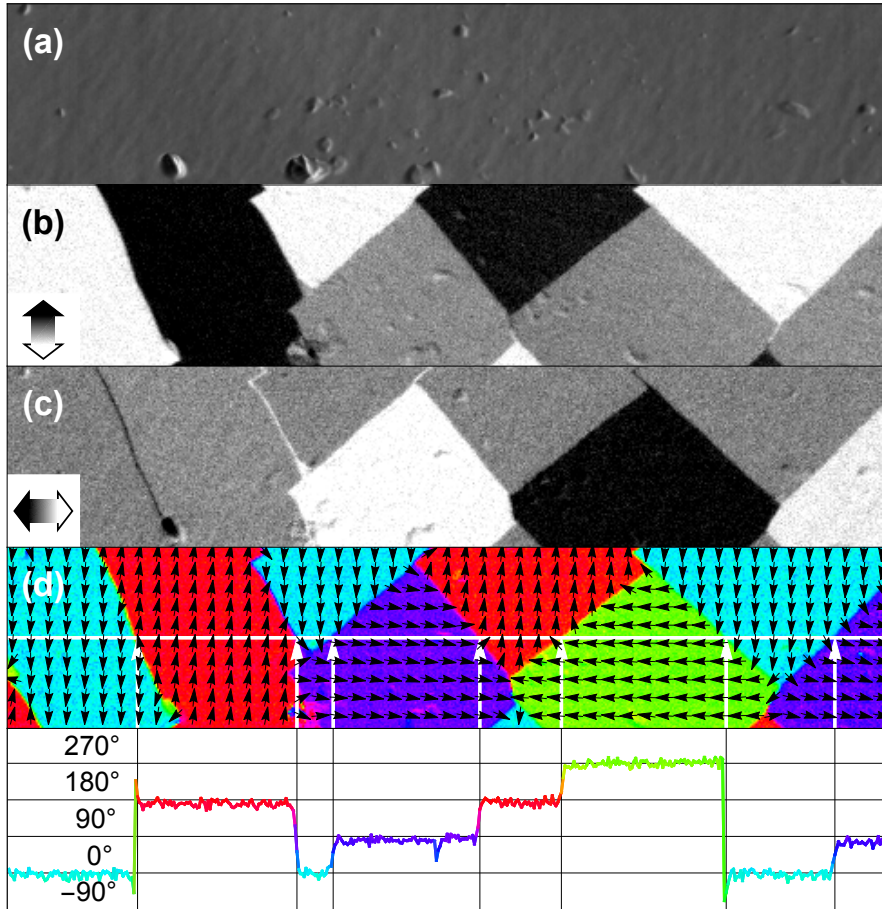
Figure 3.3: Magnetization configuration of a multidomain state on the surface of an iron whisker [93]. The topography depicted in (a) shows the whisker with the corrected in-plane asymmetry shown in (b) and (c). The in-plane magnetization direction derived from (b)/(c) is indicated in (d). The graph below depicts the orientation of magnetic moments along the indicated line in (d) relative to the magnetization direction of the first domain with four distinct orientations 90° apart.

scale, an area is divided into smaller areas which are subsequently measured step-by-step. The collected data is sorted into three matrices, one for the topography and two for the orthogonal asymmetry components, A_x and A_y. Experience has shown that a correction has to be applied to the acquired asymmetry (see appendix 7.1), e.g. due to differences in the inherent Channeltron efficiencies and a geometrical misalignment of the sample. Figure 3.3 illustrates the outcome of a measurement with the magnetization components for two orthogonal directions represented as grayscale images in (b)/(c) and the combined data in (d) using a color-code. The data is sufficient to determine the relative orientation of the observed domains and identify the influence of defects on the magnetic structure. A closer look at the domain walls reveal 90° and 120° transitions, e.g. the first two domain walls are characterized as Bloch lines [18] and show a pronounced reduction in the in-plane asymmetry indicating magnetic-flux through the surface. Since it is not directly accessible with our SEMPA setup, we estimated the out-of-plane magnetization component, $|A_z^2|$, by
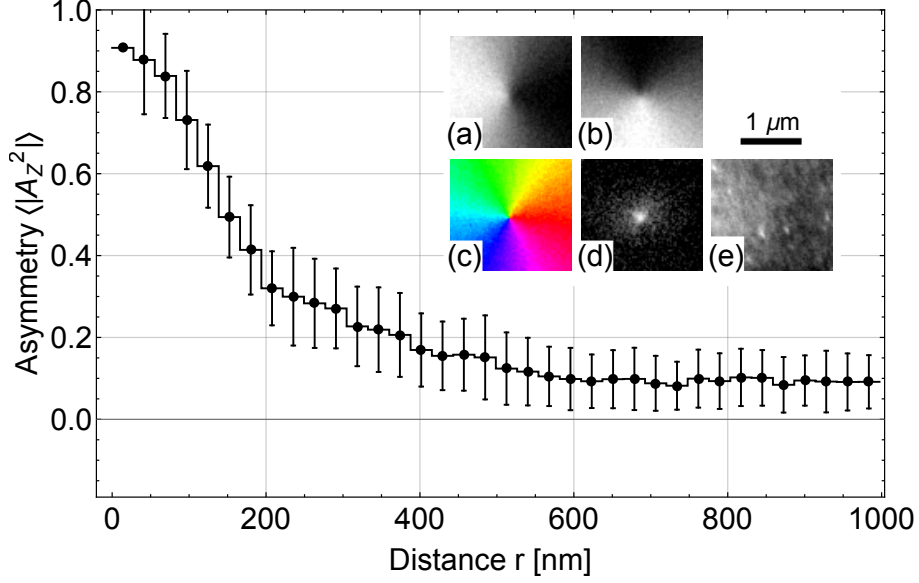
Figure 3.4: Estimated average magnitude of the out-of-plane asymmetry derived from the corrected measured in-plane components in a vortex state. The measurement was performed with a primary electron acceleration voltage of $10\,\mathrm{kV}$, imaging the state multiple times and applying a drift correction before combining the measurements. The inset (a)/(b) shows the measured in-plane asymmetry components of the considered magnetic state and the combined color-coded image in (c). (d) depicts the derived out-of-plane contribution, $|A_z^2|$, corresponding to the graph. $\langle|A_z^2|\rangle$ shows a strong increase with decreasing distance, r, to the vortex core below $r \approx 200\,\mathrm{nm}$ and approaches the noise floor limit for large r. Micromagnetic simulations have shown a vortex core radius of $\sim 10\,\mathrm{nm}$ associated with a sharp decrease of the out-of-plane magnetization component. However, direct measurements of the out-of-plane asymmetry showed a good agreement with simulations [83]. The difference can be attributed to a convolution of properties of the sample and the measurement setup, e.g. a mixing of secondary electrons from the primary and the backscattered beam, originating from different positions close to the primary electron beam spot [83], as well as beam properties such as the intensity distribution. Furthermore, it depends on the angular and energy acceptance range of the secondary electron detector [70], as well as the distribution of the primary electron energies. The topography of the measured sample can be seen in (e).

employing the imposed in-plane asymmetry normalization[2]:

$$|A_z^2| = |1 - A_x^2 - A_y^2|.$$

Even though, all SEMPA systems are restricted to two simultaneous orthogonal asymmetry component measurements, modified setups determine the third component in a second measurement to complete the picture, e.g. A_x & A_y followed by A_x & A_z [71, 83]. To illustrate this, we derived the profile of the estimated out-of-plane component of a flux-closed vortex state (see Fig. 3.4). Since the escape depth, λ, of spin polarized secondary electrons for transition metals is about $1\,\mathrm{nm}$ the surface condition has to comply with

---

[2]We use an area which is expected to have no magnetic flux through the surface to determine a suitable asymmetry correction and occasionally change the area selection to adjust for the specific magnetic state.
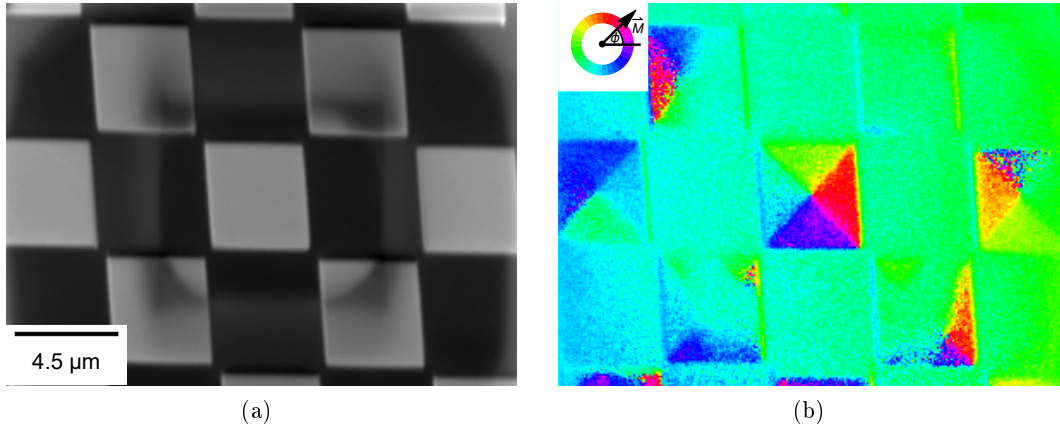
(a)   (b)

Figure 3.5: (a) Sample topography showing regularly arranged Permalloy squares each with a lateral dimension of $4.3\,\mu$m on a Si/SiO_2 substrate. Strong electron beam-induced hydrocarbonization of structures close to the image center is visible [94]. (b) Color-coded magnetization direction after applying an asymmetry correction to the central square. The central structure shows a well-defined Landau state while the remaining structures seem not to exhibit flux-closure magnetic states due to the skewed asymmetry. Here, the effects of a surface contamination-induced reduction in the average polarization of the secondary electrons originating from the contaminated area [96], preventing an immediate comparison of different areas with different surface conditions within the image.

the SEMPA requirements, e.g. undesirable capping and oxidized layers are removed using argon milling. Furthermore, to maintain suitable surface conditions measurements are performed in a UHV environment ($p_{Base} \sim 10^{-12}\,$mbar). Nevertheless, a degradation due to electron beam induced deposition of the residual gas is observed and reduces the polarization of secondary electrons produced in the magnetic layer underneath (see Fig. 3.5) [94]. An iron film, a few atoms thick, added to the system can increase the magnetic contrast by an exchange coupling through the contamination to the first magnetic layer of the sample [90] or by sputter cleaning the surface and then deposit Fe or directly deposit a thin Fe layer on the film under investigation [95]. Additionally, a thorough examination of the central Landau state indicates an apparent change in the asymmetry close to the edges and is characteristic for rough structures with high curvature [81]. A controlled correction of these effects by means of post-processing is unknown, however, suitable spin detectors employ a second scattering target with a low Z-material, e.g. carbon, to eliminate the effect by directly comparing the images at two vastly different spin-orbit coupling strengths [81]. A line scan across the structure reveals a pronounced change in both asymmetry components as well as in the total count rate (see Fig. 3.6). Thus, we restrict our consideration of the in-plane magnetization to areas sufficiently far away from the aforementioned features.
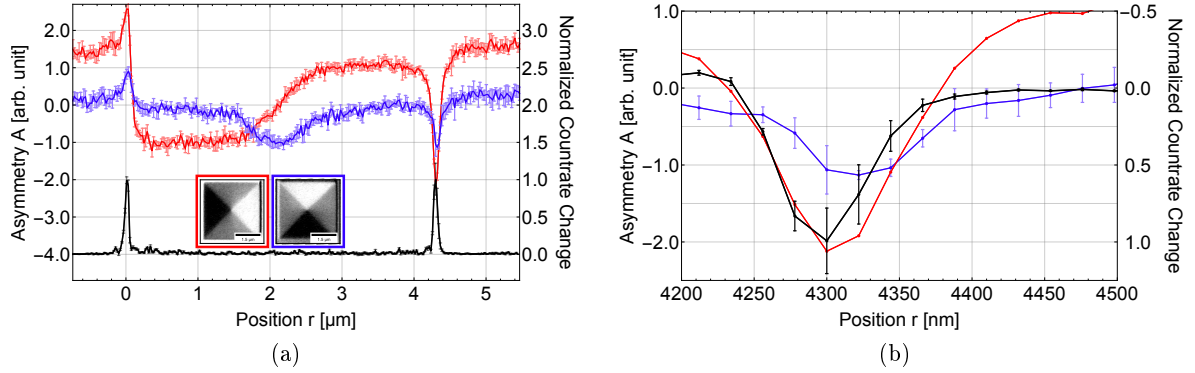
Figure 3.6: (a) shows a line scan across the corrected in-plane asymmetry of a Landau state in a $4.3\,\mu$m wide Permalloy square. The normalized count rate change (black line) exhibits pronounced spikes at the sample edges and the perceived in-plane asymmetry shows features at the same positions (see insets of the measured state). (b) A detailed view of the right edge indicates a feature width in the count rate change of $\sim 100\,$nm which agrees well with the change in the magnetic images.

3.3 Magneto-Optical Kerr Effect

Our main measurement setup, SEMPA, is limited to operation at low external magnetic fields, typically $\sim 1\,\mathrm{Oe}$ [74, 81], and thus a field-induced hysteresis can not be observed during operation. Here, we resort to the magneto-optical Kerr effect (MOKE) discovered by Kerr in 1877 [97] to measure the magnetic hysteresis as well as its angular dependence. It is differentiated into polar-, longitudinal-, transversal and additional higher order MO effects, although the latter are not considered in this analysis. In particular, longitudinal MOKE enables the characterization of in-plane magnetized materials, e.g. Permalloy, by illuminating the sample with a light beam which is linearly polarized perpendicular to the plane of incidence (see Fig. 3.7) [97]. During the reflection process, the two orthogonal polarization components undergo a phase shift due to the magnetization direction dependent dielectric tensor [98]. The polarization rotation of the outgoing light is subsequently determined for different external magnetic fields to infer the hysteric behaviour. However, the obtained signal only follows the magnetization qualitatively and depends on further parameters, e.g. the optical properties of the material and the geometrical arrangement of the setup such as the complex refractive index and the angle of incidence, θ [100]. Nonetheless, it allows the extraction of the normalized remanent magnetization, M_r/M_S, and the coercive field, H_c. Furthermore, by measuring a hysteresis loop along the magnetically hard axis (see Fig. 3.7 (b)) and assuming the applicability of the Stoner-Wohlfarth model for the measured material the anisotropy field, $H_K = 2K(\mu_0 M_S)^{-1}$, can be deduced [99]. The information depth of MOKE can be considerably larger than for SEMPA and is for metallic systems on the order of $20\,\mathrm{nm}$ [101]; thus, the removal of thin metallic capping layers can be avoided.
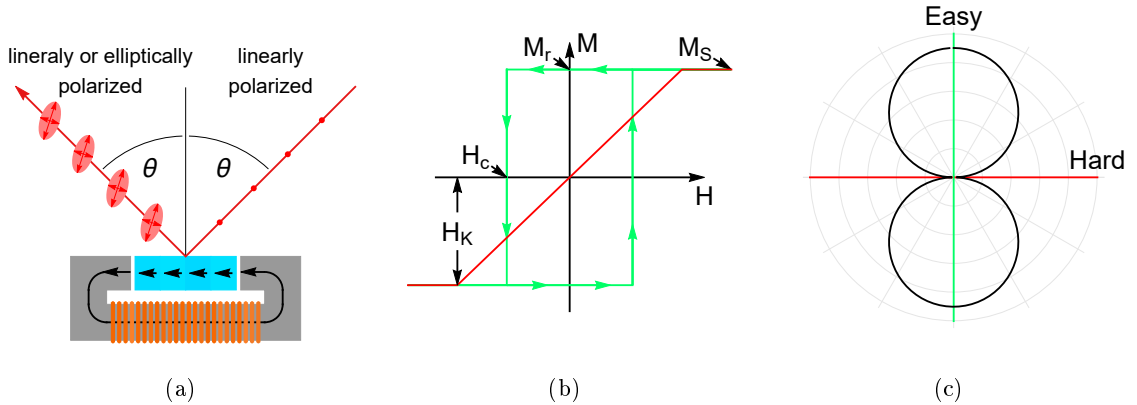

Figure 3.7: (a) Schematic of a longitudinal MOKE measurement on an in-plane magnetized material. Here, the linearly polarized light beam (red) gets reflected at a surface magnetized parallel to the plane of incidence. The polarization of the reflected light carries information about the magnetization of the probed surface. Furthermore, an external magnetic field can be applied during measurements to capture the hysteric behaviour depicted in (b) for the magnetically easy (green) and hard axis (red) of a material with a uniaxial anisotropy. (c) shows the angular dependence of the remanent magnetization, M_r, according to the Stoner-Wohlfarth model [99].
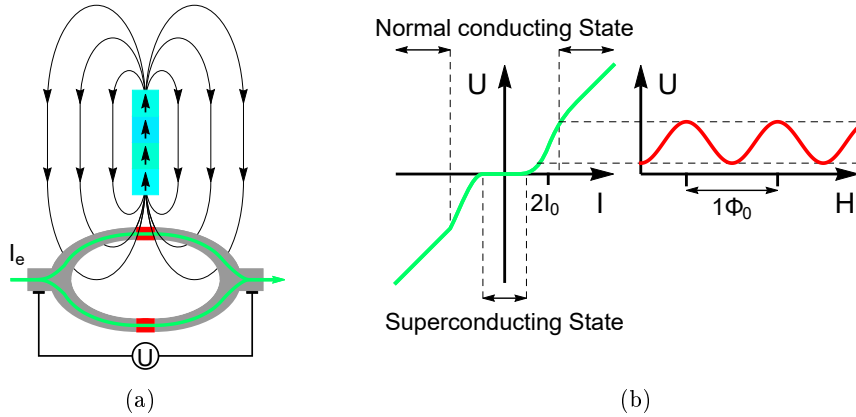
Figure 3.8: (a) The schematic depicts a DC-SQUID measurement with a superconducting loop and two Josephson junctions (red). The magnetic sample generates a stray field which causes a magnetic flux, ϕ, through the enclosed area. Within the superconducting state (see (b)) no voltage response occurs. Thus, a bias current, $2I_0$, is injected into the system and drives it into an intermediate state which enables resistance measurements. (b) shows the operation of a SQUID at the bias current and the periodic voltage response as the magnetic field is changed. The periodicity is given by the magnetic flux quantum $\Phi_0 = 2\pi\hbar/(2e)$. Adapted from [106].

3.4 Josephson Effect and SQUID Magnetometry

During current-induced domain wall excitations high current densities are employed leading to a substantial thermal load on the structure. To counteract this, the temperature of the system is lowered via a cryostat to prevent structural deterioration [102]. However, the magnetic properties of the system, such as M_S, are temperature dependent and SEMPA relies on a sufficiently high saturation magnetization for reasonable contrast at an acceptable acquisition time. Hence, we measure M_S for different temperatures using a superconducting quantum interference device (SQUID) based on Josephson junctions. Predicted in 1962 [103] and experimentally verified in 1963/1964 [104, 105] the Josephson effect describes the electric current flow in two superconducting materials which are coupled through a thin insulating layer, commonly known as a weak link. For DC-SQUIDs[3] two Josephson junctions are introduced and a bias current, $2I_0$, is applied (see Fig. 3.8 (a)) [106]. An additional current is present in the system and depends on the magnetic flux, Φ, through the area enclosed by the device. In the case that $2I_0$ is within a small range above the critical current, the measured voltage, U, becomes periodic in the magnetic flux (see Fig. 3.8 (b)) [106]. Thus, after calibrating the system, magnetic flux changes below $\Phi_0/4$ can be deduced by observing U, however, a negative feedback mechanism is applied to allow for larger flux ranges by stabilizing U and determining the current applied to an induction coil (not shown) which counteracts the experienced magnetic flux change [106]. Consequently, the described SQUID is only sensitive to relative field changes and modified setups are required to measure absolute field strengths, e.g. 'flip-coil' magnetometers [106].

---

[3]The SQUID system used for our measurement is referred to as a RF-SQUID and relies on a single Josephson junction. However, in the following the mode of operation of a DC-SQUID is described.

28

3.5 Ferromagnetic Resonance

In case that an effective magnetic field, $\boldsymbol{H}_{Eff}$, is not aligned with a magnetic moment, $\boldsymbol{M}$, a precession of $\boldsymbol{M}$ around the field with a frequency of $f_{Lamor} = \gamma|\boldsymbol{H}_{Eff}|$ is observed due to the field-induced torque. The dynamics of the magnetic moment including the subsequent alignment with $\boldsymbol{H}_{Eff}$ through energy dissipation is described by equation 2.4.1. Assuming a homogeneously magnetized macroscopic ferromagnetic state driven by a homogeneous external magnetic field with sinusoidal modification of frequency, f, Kittel [107] derived a magnetic susceptibility with a pronounced maximum at a shape and $|\boldsymbol{H}_{Ext}|$ dependent ferromagnetic resonance frequency (see Fig. 3.9 (a)),

$$f_{FMR} = (2\pi)^{-1}\gamma\sqrt{|\boldsymbol{H}_{Ext}|(|\boldsymbol{H}_{Ext}| + M_S)}. \qquad (3.5.1)$$

Thus, performing an excitation frequency sweep for a fixed external field strength, $|\boldsymbol{H}_{Ext}|$, reveals the saturation magnetization, M_s, and the frequency profile of the material susceptibility. In a conventional ferromagnetic resonance (FMR) measurement an external magnetic field sweep is performed at a constant excitation frequency, f_{FMR}. Here, the
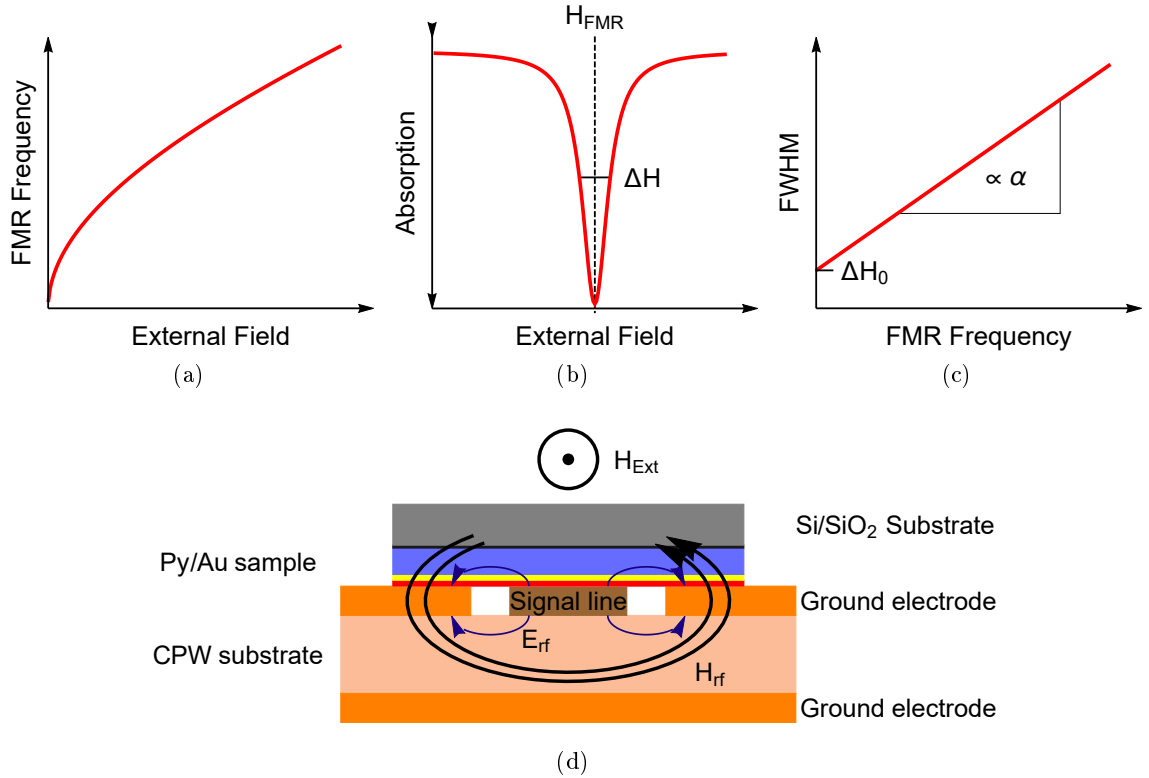

Figure 3.9: (a) Schematic dependence of ferromagnetic resonance frequency, f_{FMR}, on the external field strength, $|\boldsymbol{H}|$. (b) A schematic of an absorption spectrum determined via a FMR measurement showing a maximum at H_{FMR} with a FWHM of ΔH. (c) shows the dependence of the FWHM on the excitation frequency as well as the relation of the slope to α. The intersection with the y-axis indicates inhomogeneous broadening. (d) shows a schematic of the cross section of the experimental setup with a film sample placed on the signal line which emits a periodically modulated magnetic field, $\boldsymbol{H}_{rf}$. The sample is separated from the waveguide by a thin PMMA film (red) for electrical isolation.

sample is placed on the signal line of an electrically grounded coplanar waveguide (CPW) (see Fig. 3.9 (d)).

The observed spectrum (see Fig. 3.9 (b)) provides a convenient way to determine the Gilbert damping parameter, α, via the full width at half maximum (FWHM), ΔH, of the resonance peak at H_{FMR} [108]:

$$\Delta H = 4\pi\alpha\gamma^{-1}f_{FMR}$$

However, for spatially dependent resonance conditions an additional linewidth broadening, ΔH_0, occurs which is attributed to field inhomogeneities, two-magnon scattering and local variations in sample parameters such as the saturation magnetization, the anisotropy and deviations from a thin film geometry [109]. Within the local resonance model the interaction between neighbouring magnetic moments is small and the linewidth is described by [109–111]:

$$\Delta H = \Delta H_0 + 4\pi\alpha\gamma^{-1}f_{FMR}. \tag{3.5.2}$$

Thus, it is necessary to determine ΔH for various frequencies and infer the Gilbert damping parameter from the slope seen in Fig. 3.9 (c). In the case of a considerable large interaction strength between magnetic moments a rich excitation spectrum is observed which complicates the spectrum analysis as well as the determination of the damping parameter [109].

3.6 Rutherford Backscattering Spectroscopy

The elemental composition of a material can be analyzed by a wealth of techniques based on different interactions, e.g on X-ray absorption. Dating back to an experiment in 1911 [112] ionized atoms of energy, E_0, mass, M_0, and charge, Z_0, are used in scattering techniques to analyse samples of various thicknesses. For thin samples the escape of particles from the sample side facing the ion source as well as on the opposite side can be detected. Rutherford backscattering spectroscopy (RBS) restricts the analysis to backscattered particles and is thus applicable to thick films, too. For light ions, e.g. Alpha particles, the detected particles are themselves Alpha particles, however with altered energies, E_{Out} (see Fig. 3.10). Since the Rutherford cross section is charge and mass dependent a careful examination of the energy distribution of the detected particles enables the relative abundance of the elemental constituents to be inferred [113, 114] and further analysis yields their distribution since the scattering energy depends on the depth, d, in which a scattering event occurs [113].

In this work the RBS setup of the Helmholtz Zentrum Dresden Rossendorf is employed[4] to determine the dysprosium dopent concentration of Permalloy films (see chapter 5).

---

[4]We expressly thank Prof. Dr. Jürgen Fassbender, Dr. Julia Osten and Jonathan Ehrler for performing the RBS measurements and for the clarifications provided.
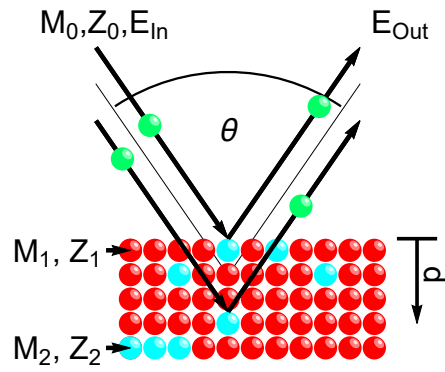
Figure 3.10: A compound is analyzed using RBS which employs a beam of light ions (green) of energy, E_{In}. The material composition and element specific depth profile is inferred by measuring the energy, E_{Out}, of the outgoing ions. The highest mass sensitivity is reached for a scattering angle of $\theta = 0°$ [113].

3.7 Sample Preparation

In this thesis, we observe the equilibrium magnetization configuration of multiple structures with varying shapes, widths and thicknesses. For repeated structures with an intended identical size, a reliable and reproducible fabrication is required to render a meaningful comparison possible. Several factors, including the substrate material, lithography steps, deposition conditions and material have to be considered and are described in the following. For the experiments, we produced geometrically confined magnetic structures with typical lateral dimensions between 100 nm and 5000 nm using electron beam lithography[5] (EBL) and molecular beam epitaxy (MBE) deposition which is performed in an ultra high vacuum (UHV) environment. Electron beam lithography is the main technique for defining the geometric shapes as well as the spatial size of structures, and is widely used in nanofabrication of submicron structures down to below 10 nm [115, 116]. The lithography steps are performed in a "Class 10" cleanroom environment to prevent contaminants such as dust particles altering the shape, roughness and composition of the resulting structures. The majority of our samples consist of isolated ring and electrically contacted disk structures. For these samples, we use undoped naturally oxidized Si substrates with a thin oxide layer [117–119] and a resistivity of $> 1000\,\Omega cm$. The substrate is grounded and sufficiently conducts electric charge injected into the bulk by our electron beam during the lithography and SEMPA imaging, while the oxide layer electrically isolates structured samples sufficiently to prevent both shunting during current-driven manipulations and charging of detached structures during imaging. We use different thickness positive resist stacks during the production process, but restrict ourselves to methyl-methacrylate (MMA) and polymethyl-methacrylate (PMMA) as polymers and use anisole as a solvent. In any case, the resist stack thickness is controlled by the solvent concentration and the rotation speed during the spin coating process which is used to create a homogenous MMA or PMMA thin film. Each resist film is spin coated separately, followed by a rest time for the film to homogenize, a baking step to remove solvent as well as to induce cross linking of the acrylate, followed by an additional rest time. During the next step, the cross linked MMA/PMMA is broken apart [120] to pattern the critical sample structure, e.g. a disk or a ring, which is transferred using the lithography system with an appropriate aperture size to enable a smaller step size for a given area exposure dose and reduce the electron beam speed during writing. Furthermore, for contacted or multi-step structures, markers are patterned to allow precise alignment during the next exposure step. Developing/dissolving the resist in a methyl isobutyl ketone (MIBK) bath, as one of the most critical steps in lithography, is carefully performed to achieve a reproducible linewidth and edge roughness. Isopropyl alcohol (IPA) is then used to stop the development process. The following material deposition is done in a molecular beam epitaxy (MBE) setup in an ultra high vacuum chamber with a base pressure of $\sim 10^{-9}$ mbar and deposition rates of 4 nm/h for iron (rings), $4 - 14$ nm/h for Permalloy and up to 2 nm/h for dysprosium (disks). Here, the deposition rates are determined with a calibrated quartz microbalance. Due to the geometry of the MBE chamber, the sample is turned by up to 180° after the first deposition to avoid significant layer mismatch between the first and subsequent layers. During the second deposition a thin gold capping layer of $\sim 3 - 7$ nm is added at rates up to 9 nm/h to prevent oxidation of the magnetic material during the next production steps. The excess deposit is removed during a lift-off process in a solvent bath, e.g. using 120°C N-Ethylpyrrolidone (NEP) for rings and 50°C acetone for disk structures.

---

[5]Our electron beam lithography uses a commercial Raith *PIONEER* system.

This is the concluding fabrication step for our iron ring structures, however, for contacted Permalloy disks we repeat the electron lithography steps and deposit a $Cu(\sim 80\,\mathrm{nm})/Au(\sim 10\,\mathrm{nm})$ stack as an electric contact. Firstly, we carefully align the contact pad mask to the first metal layer in a multistep alignment process, expose the area and transfer the developed sample to the MBE chamber. Secondly, to obtain symmetric contacts and reduce shadowing effects due to the height of the first metal layer, we deposit a copper layer with up to $\sim 100\,\mathrm{nm/h}$ as well as a gold capping layer with $\sim 8\,\mathrm{nm/h}$ from an angle (see Fig. 3.11) and turn the sample by 180° after reaching half the target thickness for copper and gold, respectively. The sample production concludes with a lift-off process in a heated acetone bath.

A numeric listing of the sample preparation procedure is outlined below:

1. Cleaning of cleaved Si/SiO_2 substrate: We remove a protection layer from the substrate using NEP and mechanical rubbing, followed by rinsing in acetone, IPA and a water bath. Afterwards, the substrate is inspected with an optical microscope and the steps are repeated till the surface contamination level appears low.

2. The substrate is coated with a thin layer of PMMA 4% using 500 rpm for 2 s followed by 3500 rpm for 60 s with a set ramp-up time of 0 s.

3. The substrate rests for 7 min at room temperature before a 90 s soft-bake at 180°C is applied, followed by another rest time of 7 min.

4. The lithography pattern is transferred using an area dose of $175\,\mu\mathrm{C/cm}^2$ at an acceleration voltage of $U = 10\,\mathrm{kV}$ and an aperture of $20\,\mu\mathrm{m}$ to reach a stepsize of 4 nm.

5. The resist is developed in a MIBK:IPA (1:3) bath for 30 s and stopped with IPA.

6. A magnetic material layer is deposited, either $\sim 5-25\,\mathrm{nm}$ of iron for rings or $\sim 25\,\mathrm{nm}$ of Permalloy for disk structures. The doping of Py is achieved through co-deposition of dysprosium mainly by varying the Py rate while keeping the Dy deposition rate low ($\lesssim 1\,\mathrm{nm/h}$). The magnetic layer is capped with a thin gold layer ($\sim 3-7\,\mathrm{nm}$) after aligning the sample with the gold evaporator by rotating the sample holder to minimize a layer mismatch.

7. In the case of iron ring structures, the resist is lifted-off using a 120°C NEP bath under constant agitation till the substrate is cleaned. For Permalloy, a 50°C hot acetone bath and agitation is sufficient to remove the resist and the metal layer.

For the contacted disks, we continue with the following steps:

8. The substrate is coated with MMA 6% using 500 rpm for 5 s followed by 2500 rpm for 60 s with a set ramp-up time of 0 s. .

9. The substrate rests for 5 min at room temperature before a 90 s soft-bake at 180°C is applied, followed by another rest time of 5 min.

10. The substrate is coated with a thin layer of PMMA 4% using 500 rpm for 5 s followed by 2500 rpm for 60 s.
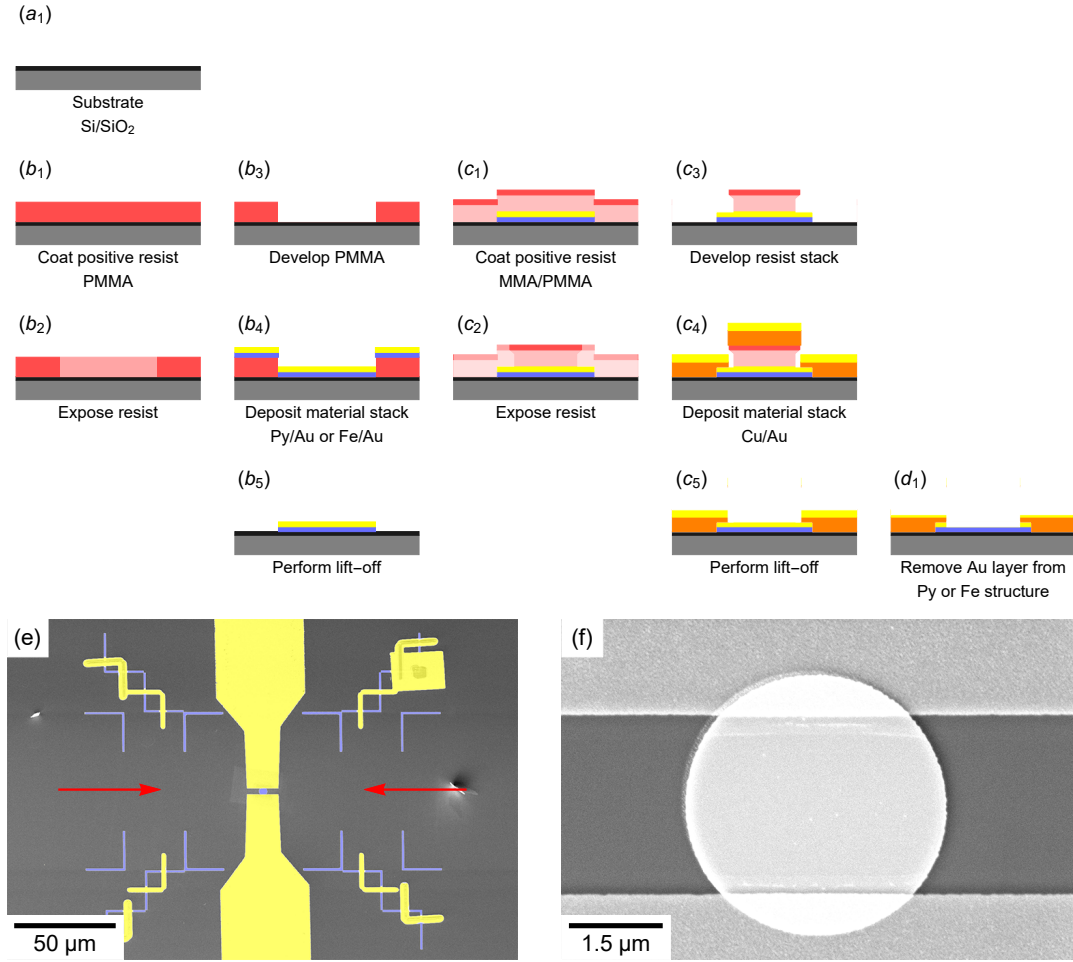
Figure 3.11: Schematic illustration of the sample preparation steps. (a_1) shows the naturally oxidized $500\,\mu$m-thick Si-substrate with an electric resistivity above $1000\,\Omega$cm. (b_1) to (b_5) describe the lithography steps necessary for manufacturing the disk or ring structures and the alignment markers (not shown). The lithography required for the electric contact structures is depicted in (c_1) to (c_5). In a last step, (d_1), the Au capping layer is removed from the disk or ring structure before performing magnetic imaging. The colored SEM image in (e) shows a Cu/Au (yellow) contacted Permalloy (purple) disk including the alignment markers. The red arrows indicate the deposition direction for the contact structures. (f) shows a close up of the structure which exhibits a limited layer mismatch as well as a small edge roughness.

11. The substrate rests for $5\,$min before a $90\,$s soft-bake at $180°$C is applied, followed by another rest time of $5\,$min.

12. The inner contact structures are transferred using an area dose of $160\,\mu$C/cm^2 at an acceleration voltage of $U = 10\,$kV and an aperture of $30\,\mu$m after carefully aligning the mask using alignment markers of the previous layer. The outer structures are written with the largest available aperture of $120\,\mu$m while keeping the acceleration voltage and the area dose constant.

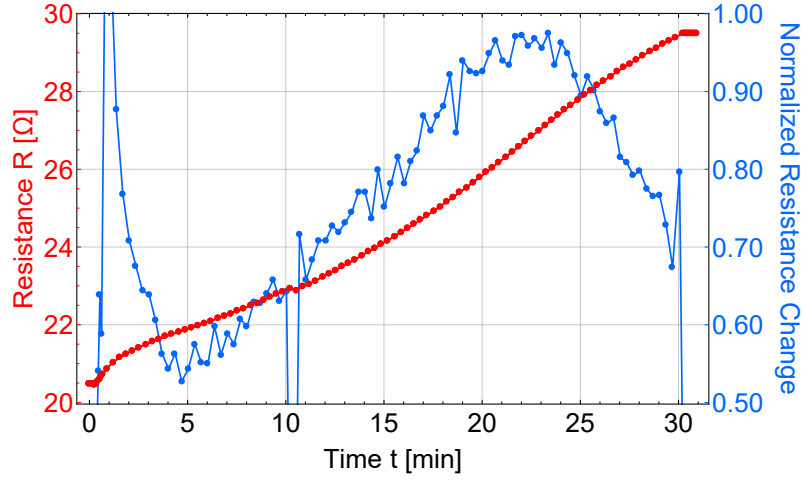13. First, a $\sim 40\,$nm thick Cu-layer is evaporated from an angle (see Fig. 3.11), followed

34

Figure 3.12: Resistance of a contacted disk structure with $4.5 \pm 0.5\,\mathrm{nm}$ thick Au capping layer during argon milling at an argon pressure of $7.5 \cdot 10^{-6}\,\mathrm{mbar}$ and an acceleration voltage of $1\,\mathrm{kV}$. Around the $22-23\,\mathrm{min}$ mark, the slope changes indicating an uncovering of the magnetic layer due to the difference in milling rate and specific resistivity of the magnetic material.

by a rotation of the sample by $180°$ and a second $Cu(\sim 40\,\mathrm{nm})$ deposition. After aligning the sample with a gold evaporator, the step is repeated for the new material with a total thickness of $\sim 10\,\mathrm{nm}$.

14. The resist is lifted-off using a $50°\mathrm{C}$ acetone bath under constant shaking till the substrate is cleaned.

The Au capping layer has to be removed for both structures to enable imaging due to the low magnetic probing depth of SEMPA. At an argon pressure of $\sim 7.5 \cdot 10^{-6}\,\mathrm{mbar}$ and an acceleration voltage of $1\,\mathrm{kV}$, we determined an Au milling rate of $\approx 0.20\,\mathrm{nm/min}$ (see Fig. 3.12).

Domain Wall Formation in Confined Geometries

In section 2.2.3 the possibility to shape the magnetic state by changing the relative influence of the Landau free energy contributions was demonstrated. Specifically for applications, a well controlled magnetization configuration of nanoscale magnetic structures is a vital requirement for spintronic devices [121]. The materials properties of a system are one key factor in changing the relative influence of the energy contributions and hence varying the material of a device is one handle to control the magnetic state.

Another contribution is introduced with a geometrical confinement of the magnetic material due to the magnetostatic energy. In thin film samples the confinement favours the magnetization to align with the surface, since there is an energetic advantage for the system to reduce the generated magnetic demagnetization field by forming flux closure states [18, 122]. However, for a large lateral sample size, complex domain structures can occur (see Fig. 4.1) and a stronger confinement in the 2d-plane is introduced to favour simpler magnetic states. Hence geometrical device design has become possible with the advent of high quality thin film deposition combined with nanoscale lithography to achieve robust, tailored spin configurations. One particularly convenient and well-studied geometry is that of thin-film mesoscopic magnetic rings which exhibit particularly simple and robust spin-configurations. Such ring structures have received interest for potential applications such as MRAM elements [123] or magnetic logic [124, 125]. Provided the ring is narrow enough, the system is dominated by the magnetostatic and exchange energy contribution, thus, it is energetically preferable for the magnetization to track the edge of the structure, leading to the lowest energy configuration being the quasi-uniform flux-closure state which is termed the vortex state [126]. On relaxation from saturation the metastable so-called onion state can result, which is characterized by two magnetic domain walls on opposing sides of the ring [127–129]. For devices, the detailed spin structure of a domain wall is crucial for setting the relevant physical properties such as the dynamic behaviour including domain wall velocities and critical current densities for current induced domain wall motion [50, 130–132] and hence this can determine the ultimate performance and attainable data storage densities. Two types of domain wall are favored in such nanoscale planar wires; in general, in narrower and thinner structures, the transverse domain wall is observed where the magnetization rotates by 180° via a roughly triangular region where the magnetization is directed off-axis to the wire [50, 130, 131, 133] (see Fig. 4.2 (a)).

Conversely, for wider and thicker structures, the so-called vortex wall is preferred where the magnetization curls around a central vortex core region in which the magnetization is directed out of the plane of the structure [50, 130, 131, 133] (see Fig. 4.2 (d)). Furthermore for strip-like structures above a critical thickness of 55 nm of Permalloy, three-dimensional flux-closure domain wall spin structures have been reported showing distinct properties [134, 135]. Details of the transition to these more complex three dimensional domain wall spin structures and also domain walls in cylindrical wires, which are beyond the scope of this thesis, are provided in [136]. The energetically favoured state is determined by the interplay between dipolar and exchange energy contributions which scale differently with the geometry. Beyond such qualitative considerations, for the workhorse system Permalloy, the quantitative details of the phase diagram are well known [130, 131], however, the materials' parameters of the system also influence the range of sizes where the different domain wall types are stable as has been shown for the case of cobalt [130].
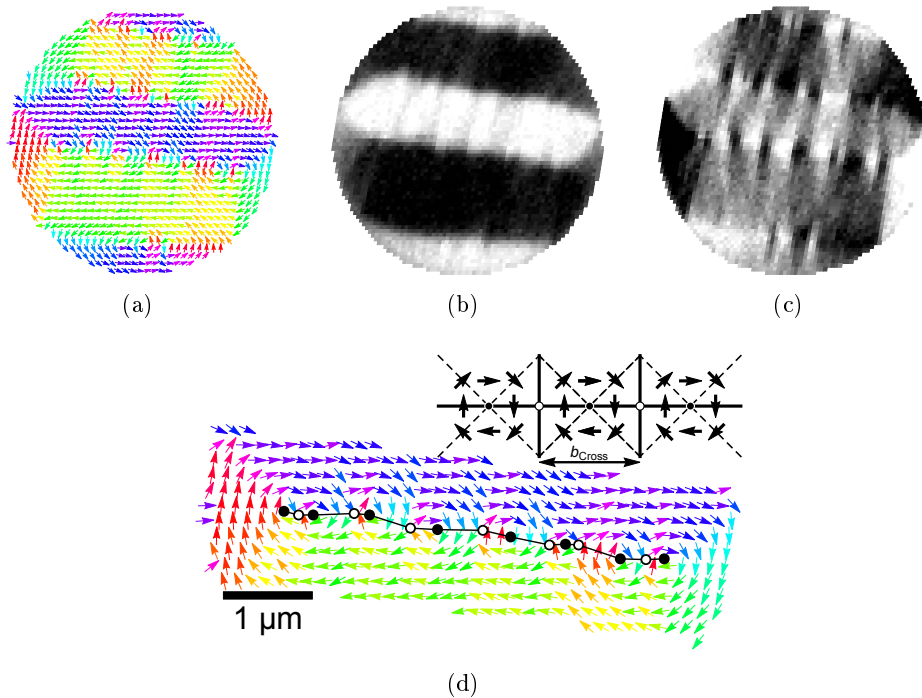
Figure 4.1: Domain structure of iron in a $14\,\mathrm{nm}$ thick disk structure with a diameter of $6\,\mu\mathrm{m}$ grown on a Si/SiO_2 substrate after saturating the magnetic state in an external field. Due to the loose geometrical restriction in the 2d-plane the magnetic state exhibits exhibits a complex domain state. Arrows in (a) depict the magnetization direction derived from the measured horizontal, (b), and vertical, (c), in-plane components and indicate stripe domains due to an uniaxial crystalline anisotropy. A close-up view, (d), of the spin configuration seen in (a) indicates a cross-tie domain wall. Along the domain wall (black line) eight vortices (black dots) with a clockwise rotation direction alternate with seven antivortices (white dots). The mean distance between successive vortices and antivortices is $b_{Cross}/2 \approx 0.3\,\mu\mathrm{m}$. The inset shows a schematic of a cross-tie domain wall (reproduced from [137]).

For spintronic devices based on domain wall motion, materials with a large spin polarization are desirable for large torques [138], while additionally low intrinsic magnetic anisotropies are required in order to reduce pinning effects and to provide a robust system where the magnetization configurations can be tailored via the geometry. Fe could be an attractive material in this regard, since it has a lower magnetocrystalline anisotropy than Co, while retaining a high spin polarization and the highest saturation magnetization of the elemental ferromagnets. Furthermore, while some recent research interest has shifted to more exotic materials such as highly spin polarized Heusler alloys [139] and oxides [140], there remain barriers to the industrial adoption of such systems due to the difficulty in obtaining reliable growth conditions on industrially relevant substrates for large scale production. Hence, there remains great potential for use of simple materials in real applications, however, surprisingly in the case of iron an in-depth characterization of the domain wall spin structures is so far lacking, despite the aforementioned advantageous magnetic properties of this material. While many studies just consider the two types of domain wall mentioned above, it has been predicted [131] and experimentally confirmed [141]
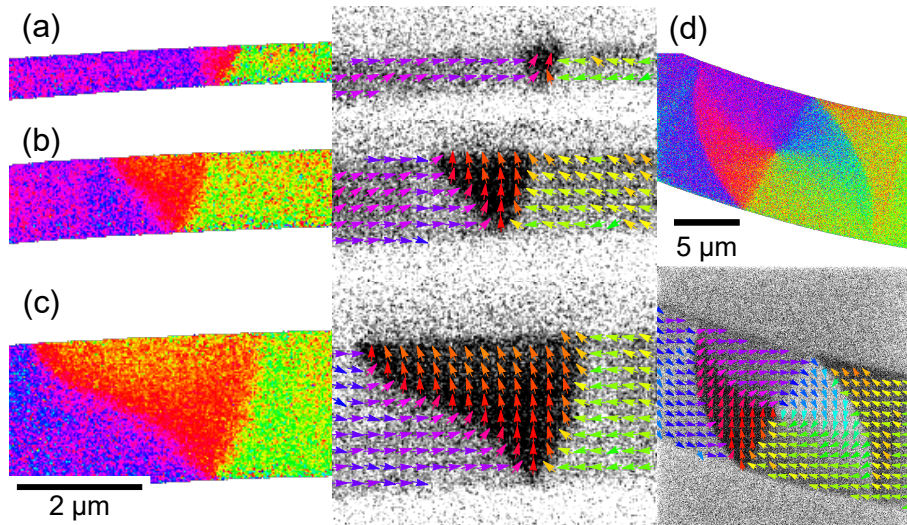
Figure 4.2: Domain wall spin configuration in Permalloy half-ring structures after nucleation in an external magnetic field. Transverse walls are present in structures (a)-(c), however, only the narrowest structure, (a), with 700 nm exhibits a symmetric transverse wall. In the wider structures (b)/(c) with 1300 nm and 2600 nm the domain wall structures are asymmetric and the asymmetry increases with the structure width. (d) shows a vortex domain wall in a 10 μm wide half-ring structure.

that the transverse domain wall can occur in both symmetric and asymmetric configurations (see Fig. 4.2 (a)-(c)), which are expected to have different properties. For example, it has recently been revealed that the symmetry of the transverse domain wall is important in determining the depinning process from domain wall traps [142] and wire kinks [143]. Additionally in the presence of transverse applied fields, asymmetric transverse domain walls were observed to exhibit new dynamic behaviours with the upper and lower edges of the wall propagating at different velocities during longitudinal field driven motion, leading to a gradual increase in the wall asymmetry [144]. This means that it is vital to also investigate the degree of asymmetry of the transverse domain walls with geometry, which has been previously neglected for most studies and requires suitably high-resolution magnetic imaging to discriminate the sometimes subtle differences between the wall types such as provided by SEMPA.

Within the simulations we systematically change the width, w, and thickness, t, of the structures and determine the resulting domain wall type with the lowest energy. The simulations provide a good qualitative understanding of the competing energy terms and show excellent agreement with an analytical model of the system, yet do not provide a good quantitative agreement with the experimentally observed wall types. For a fuller understanding we perform further simulations which include the process of domain wall nucleation on relaxing the spin structure from the initial state. A phase diagram of the different wall types is presented which we show can only be fully understood by taking into account the experimental domain wall initialization procedure in addition to the effects of thermal activation and sample defects.

4.1 Experimental and Numerics

In order to calculate the expected energetic stability of the different domain wall configurations in iron we employ to micromagnetic simulations using the MicroMagnum code [47]. Here, the Landau-Lifshitz-Gilbert (equation 2.4.2) is used in the form:

$$\frac{d\boldsymbol{M}}{dt}(\boldsymbol{r}) = -\gamma[\boldsymbol{M}(\boldsymbol{r}) \times \boldsymbol{H}_{Eff}(\boldsymbol{r})] - \frac{\alpha}{M_S}[\boldsymbol{M}(\boldsymbol{r}) \times \frac{d\boldsymbol{M}}{dt}(\boldsymbol{r})]. \qquad (4.1.1)$$

In contrast to the frequently studied straight wires, in this work curved structures are investigated which have particular merits in both experiment and applications. Such geometries facilitate the nucleation of domain walls at desired angular locations by the simple relaxation of the magnetization from a saturated state along a desired direction [130] and do not require the injection of domain walls from adjacent nucleation pad regions, which can be prone to stochasticity concerning the obtained spin structures within the wire.

Half rings were simulated on a two-dimensional grid with 800×400 rectangular cuboidal cells having in-plane edge length of 1.25 nm. The thickness of the half ring structure is simulated using a single 2-dimensional layer with height d, which is a good approximation for our samples where no significant variation of the spin structure across the sample thickness is expected. For significantly larger thicknesses, distinct Landau domain wall states have been reported in magnetic nano-strips [135] and magnetic multilayer systems [134]. However, for films in our thickness range, the magnetization is essentially uniform along the z direction and hence a single layer description is a reasonable assumption which helps to reduce the required simulation times.

The simulations in this work were performed for a range of half ring sizes for widths between $w = 30$ and 400 nm and thicknesses between $d = 5$ and 40 nm. In order to reduce the computation time the outer diameter (O.D.) was kept at 1 μm for all widths and instead of the experimentally studied full ring, a half ring shaped wire was simulated which does not change the results as checked for a few selected geometries. Standard materials parameters for iron were chosen equivalent to $M_s = 1.7 \cdot 10^6$ A/m and $A = 2.1 \cdot 10^{-11}$ J/m [145]. For each geometry two simulations were initially performed to find the lowest energy state, one starting from a vortex wall configuration and the other starting from a transverse wall. The states were then relaxed and the total energy of the final configuration calculated in each case to compare the relative stability. In a first stage of relaxation a small external field was applied along the y axis of $\mu_0 H \approx 2$ mT, in order to stabilize the position of the domain wall in the centre of the half ring and prevent it from migrating to the half ring ends where it can be expelled, resulting in a uniformly magnetized state. In real systems naturally occurring defects play an equivalent role and act as small pinning centres for the walls, providing an energy barrier between the metastable onion state and the lowest energy vortex state. In a second stage of relaxation the field is removed and the relaxation was then continued until the state was suitably converged, defined as a rate of change of magnetization of less than 0.01° per ns. In order to experimentally investigate the actually occurring domain wall types magnetic imaging of the domain wall configurations in iron rings was performed. For the imaging of the domain wall spin configurations in rings of other materials, previous work has employed electron holography [141] or Lorentz microscopy, which require that the samples are fabricated on delicate membranes for the transmission measurements [128, 146], photo-emission electron microscopy [130, 147], which is mainly available at large-scale facilities and can be limited in its resolution, or magnetic force microscopy (MFM) [127, 135, 148–150], which can modify the spin configuration of the sample and is however sensitive only to the demagnetization

field from a sample and therefore harder to relate directly to the spin structures obtained from simulations. The samples were fabricated on Si/SiO_2 substrates via a standard electron beam lithography procedure followed by lift-off. Iron was deposited by ultra-high vacuum thermal evaporation at rates around 4 nm/hour up to the desired thickness and a ~ 2.5 nm gold capping layer was employed, as needed, to counter oxidation of the magnetic material. In the case of the 20 nm thick rings we started from the measured 24.5 nm samples and reduced the thickness using 1 kV in-situ argon ion sputtering. For the thicker samples between 15 and 26 nm in thickness we chose rings of 2 μm O.D., however, for the thinner structures in the vicinity of the expected phase transition (thickness 10 nm $\geq d \geq$ 5 nm) we chose rings of a fixed outer diameter of 1 μm in order to provide a more direct comparison with the simulations. Different ring widths were prepared between 90 and 310 nm for the 1 μm O.D. rings or between 100 and 750 nm in the case of the 2 μm O.D. structures by changing the inner diameter. Whilst the simulations modelled isolated half ring structures the experimental structures are arrays of full rings each containing two domain walls following initialization. As such, in the experiments we also need to consider the possibility of demagnetization field interaction between adjacent domain walls both within and between rings, which can potentially lead to spacing-dependent transitions between domain wall types [151, 152]. In order to rule out such effects, neighbouring rings were separated by more than the ring diameter [153]. Furthermore the maximum studied ring width was limited to ~ 350 nm for the 1 μm O.D. in order to have a separation of several hundred nm between the two walls in the same ring, which avoids significant coupling effects taking into account a slightly higher demagnetization field interaction for domain walls in Fe as compared to that previously measured for Co due to the difference in magnetostatic energies ($\sim M_s^2$) [151].

Due to the extreme surface sensitivity of SEMPA the surface of the samples was necessarily cleaned before imaging using short periods of 1 kV argon ion milling at an Ar pressure of $7.5 \cdot 10^{-6}$ mbar in the preparation chamber of the UHV system. The sample was then transferred in UHV to the magnetization stage where the magnetic configuration was initialized at ambient temperatures by applying a magnetic field of 1.8 kOe in-situ and then relaxing the field in order to generate the onion state with two domain walls at opposing sides in the ring. The samples remained in UHV during the complete imaging, which is carried out at ambient temperature.

4.2 Results

We start with the theoretical modelling of the expected spin structures. The results of the lowest energy simulations are presented in Fig. 4.3. The inset depicts simulations of the two main wall types in 100 nm wide half rings, revealing a vortex domain wall for the thicker structure with $d = 20$ nm (top) and a transverse domain wall for the thinner structure with $d = 7$ nm (bottom). By comparing the calculated total energies for these two domain wall types for each ring size, the lowest energy state is extracted as represented in the phase diagram. The investigation of the stability of the different stable domain wall configurations in nanowires was first investigated by McMichael and Donahue via analytical modelling and micromagnetic simulation [133]. For the analytical calculation they assumed that the major contribution to the energy of the transverse domain wall was from the magnetostatic energy due to the off-axis magnetization region, while the vortex domain wall is assumed to be dominated by the exchange energy contribution from the closely circulating magnetization around the core. By equating expressions for these two
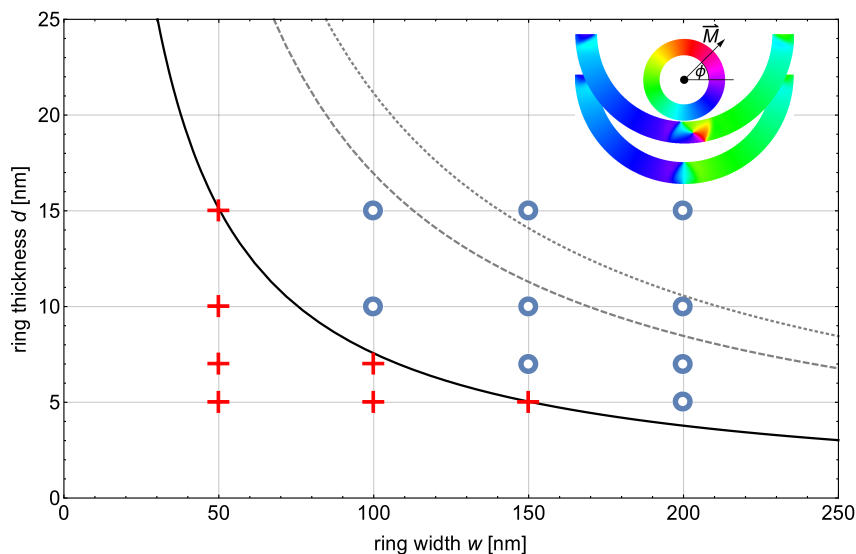
Figure 4.3: Phase diagram of the lowest energy domain wall configurations for different ring sizes from micromagnetic simulations (using MicroMagnum [47]). A red cross denotes transverse walls and a blue circle vortex walls. The solid black line is a fit to the data, with equation 4.2.2 using $C \times \delta^2 = 756 \pm 17 \, \mathrm{nm}^2$, following McMichael and Donahue [133]. For comparison the gray lines represent the lowest energy phase boundary for Permalloy (dotted) and cobalt (dashed) [130]. The inset depicts simulated head-to-head domain wall configurations in iron half rings of thickness $25 \, \mathrm{nm}$ (top) and $7 \, \mathrm{nm}$ (bottom), with an outer diameter of $1 \, \mu\mathrm{m}$ and a width of $100 \, \mathrm{nm}$. The colour wheel represents the magnetization direction which corresponds to a vector directed from the centre to the appropriate colour.

contributions, an analytical form of the width (w) vs. thickness (d) phase boundary was derived to be:

$$wd = 16\pi \ln\left(\frac{r_{\max}}{r_{\min}}\right) \frac{A}{\mu_0 M_s^2}, \tag{4.2.1}$$

where $r_{\max}$ represents the outer radius of the vortex and $r_{\min}$ the radius of the vortex core. μ_0 is the permeability of free space, M_s is the saturation magnetization and A is the exchange constant with the definition of the exchange length as $\delta = (A/\mu_0 M_s^2)^{1/2}$. Ignoring the weak logarithmic dependence, Eq. 4.2.1 is of the following form:

$$w \times d = C \times \delta^2, \tag{4.2.2}$$

where for Permalloy the constant, C, was determined from their simulations to be 128 [133]. For our results for iron the phase boundary has been fitted to this functional form, as shown in Fig. 4.3. The function can be seen to fit the phase boundary well and yields $w_{\mathrm{crit}} \times d_{\mathrm{crit}} = (756 \pm 17) \, \mathrm{nm}^2$. If we calculate the expected value using the material parameters for iron of $A = 2.1 \cdot 10^{-11} \, \mathrm{J/m}$ and $M_s = 1.7 \cdot 10^6 \, \mathrm{A/m}$ and the value of C from the work of McMichael and Donahue we get $w_{\mathrm{crit}} \times d_{\mathrm{crit}} = 740 \, \mathrm{nm}^2$ which is in excellent agreement with our results.

In comparison to other systems, the stability of the vortex domain wall is pushed to narrower and thinner structures than for either Py or Co [130] as shown by the gray lines in Fig. 4.3, which can now be directly understood as arising from the materials properties dependence of equation 4.2.2 via the contribution from the exchange length: the increased saturation magnetization in Fe favours the low magnetostatic energy vortex domain wall,
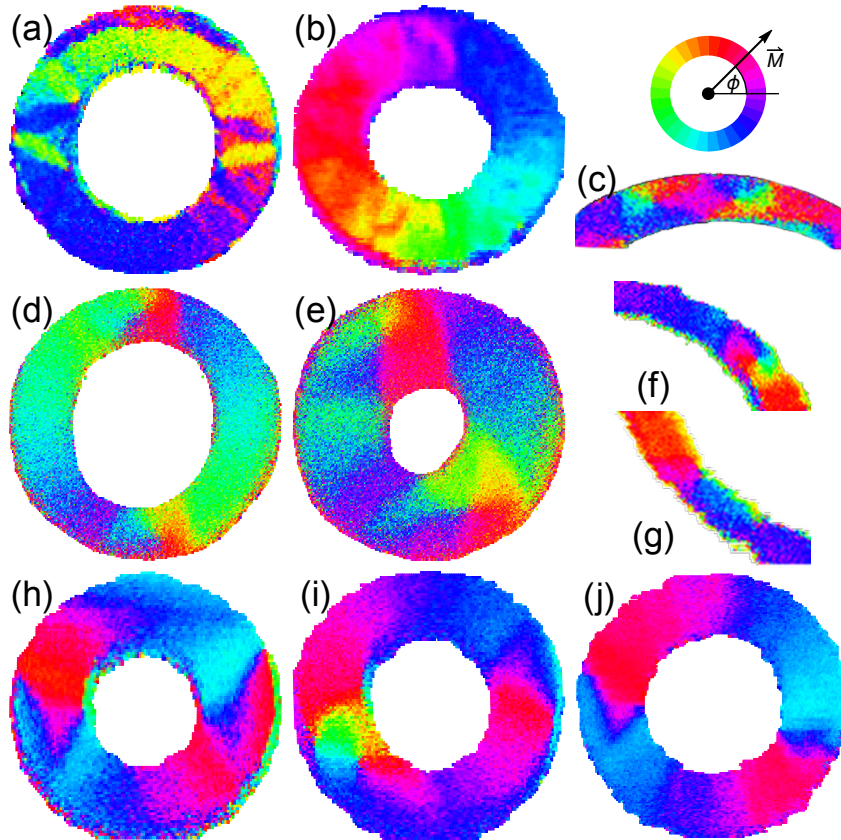
Figure 4.4: Selected SEMPA images of domain wall configurations. Ring (a) has an O.D. of $3.5\,\mu$m. The rings (b)-(e) have O.D.$=2\,\mu$m and all the remaining rings have an O.D.$=1\,\mu$m. The thicknesses of the rings are (a) $17\,$nm, (b) $12\,$nm, (c) $15\,$nm, (d)/(e) $24.5\,$nm, (f)-(i) $10\,$nm and (j) are $5\,$nm thick. The widths of the rings are (a) $750\,$nm, (b) $550\,$nm, (c) $300\,$nm, (d) $400\,$nm, (e) $650\,$nm, (f) $110\,$nm, (g) $90\,$nm, (h) $290\,$nm, (i) $270\,$nm and (j) $230\,$nm. The magnetic contrast direction is indicated by the colour wheel inset.

so that it remains the lower energy wall type down to narrower and thinner structures compared to cobalt and Permalloy. We then image the domain wall spin structures of different ring geometries. A selection of SEMPA images can be seen in Fig. 4.4. The two simultaneously measured in-plane asymmetry components of the magnetization have been combined to give the full in-plane information of the magnetization vector as represented in the colour images here. The colour wheel inset represents the local magnetization direction, which corresponds to a vector directed from the centre of the wheel to the appropriate colour. Due to our initialization procedure, most rings were observed to be in the onion state and contain two domain walls, one head-to-head and one tail-to-tail, which are roughly aligned with the axis of the initializing field (along the x-direction for ring (a) and (f)-(j), but along the y-direction for the remaining rings). However, the precise positioning of the walls is determined by local defects and hence the location of the walls in the experimental images is not always completely symmetric as would be expected for an ideal ring.

First we consider the larger structures as depicted in Figs. 4.4 (a)-(e) where the dimensions of the rings are far away from the expected phase transition region. For the largest structure of $750\,$nm width in (a) it can be seen that a fairly complicated domain structure

is observed. In particularly wide annular structures it is expected that the simplest domain wall configurations are no longer the only accessible stable magnetic states and more complicated spin-structures have been predicted and observed experimentally due to the reduced shape anisotropy [130, 147, 154]. In some structures ripple domains were observed as can be noticed in Fig. 4.4 (b) which is also one of the few cases where annihilation of the two domain walls resulted in the vortex state with continually circulating magnetization around the ring and here the ripple domains are clearer to see. In the case of Permalloy, such ripple contrast is not found for these geometries due to the low intrinsic magnetocrystalline anisotropy, however, for Fe the magnetocrystalline anisotropy is significant albeit not as large as for Co. Since the structures are polycrystalline the effect of this anisotropy should cancel out over the whole structure, unlike with epitaxial samples [155], but at a local scale statistical variations in the anisotropy of individual grains lead to such characteristic contrast [156]. Ring (c) shows an example of a more complicated double vortex structure in a 15 nm thick ring which has previously been seen in Fig. 4.4 (b) of [130] for Py as a result of current induced wall transformations [157] and recently predicted as one of a variety of more complicated (meta)stable wall structures comprising multiple vortices and antivortices in wide strips [154]. Rings (d) & (e) show vortex domain wall states in 24.5 nm thick rings with widths of 400 and 650 nm, respectively, where the vortex wall can be seen to spread out in the wider rings due to reduced geometrical confinement. Overall the domain walls observed in this size range are of vortex type or are more complicated, which is consistent with the predictions of Fig. 4.3.

We now consider the domain walls observed in smaller and thinner rings, as represented by the second range of images (f)-(j) presented in Fig. 4.4. All of these rings show onion states with either vortex walls [(f) and left side of (i)] or transverse walls with varying symmetry. In the narrowest structures there is a tendency for symmetric transverse walls [e.g. (g)], while the transverse walls in the wider structures become very asymmetric [e.g. (h)]. However, it is immediately apparent that the phase boundaries are not completely well defined since in ring (i) both a vortex and asymmetric transverse wall are shown in the same structure and in ring (j) both a symmetric and asymmetric transverse wall are seen in the same structure.

Figure 4.5 (a) shows the distribution of all the observed domain wall types. The symmetric transverse walls are depicted as red crosses, asymmetric transverse walls as black dots and vortex walls as blue circles. The black curve represents the expected lowest energy phase transition as already presented in Fig. 4.3. Each studied Fe ring with a thickness of 15 nm or more showed a vortex domain wall, whereas for structures with a thickness of 10 nm only rings with widths of 110, 270 and 275 nm exhibited vortex walls. The remaining structures at this and lower thicknesses showed either symmetric or asymmetric transverse walls. The distribution of these two domain wall types shows pronounced overlap, with both types seen in a range between 150 and 220 nm for 10 nm thick rings and a wider overlap region between 130 and 260 nm for the thinnest 5 nm thick rings. Furthermore, if we compare the observed types of domain wall to the predictions of the phase diagram in Fig. 4.3, serious quantitative discrepancies are apparent. Firstly, the observed asymmetric transverse walls are not covered at all by the analytical model and are not well represented by the simulations which calculated and compared the energies of just the two principal domain wall configurations which were set as the initial states. Secondly, while the observation of a vortex wall in Fig. 4.4 (g) fits well with the lowest energy phase boundary, many of the observed transverse walls are at much larger widths and thicknesses than would be expected. The asymmetric wall type is not able to account for the discrepancy,

since Ref. [131] found that the asymmetric transverse wall phase belongs to an area below the vortex-transverse phase boundary and hence would not explain the occurance of transverse walls of either symmetric or asymmetric type in larger structures [131].
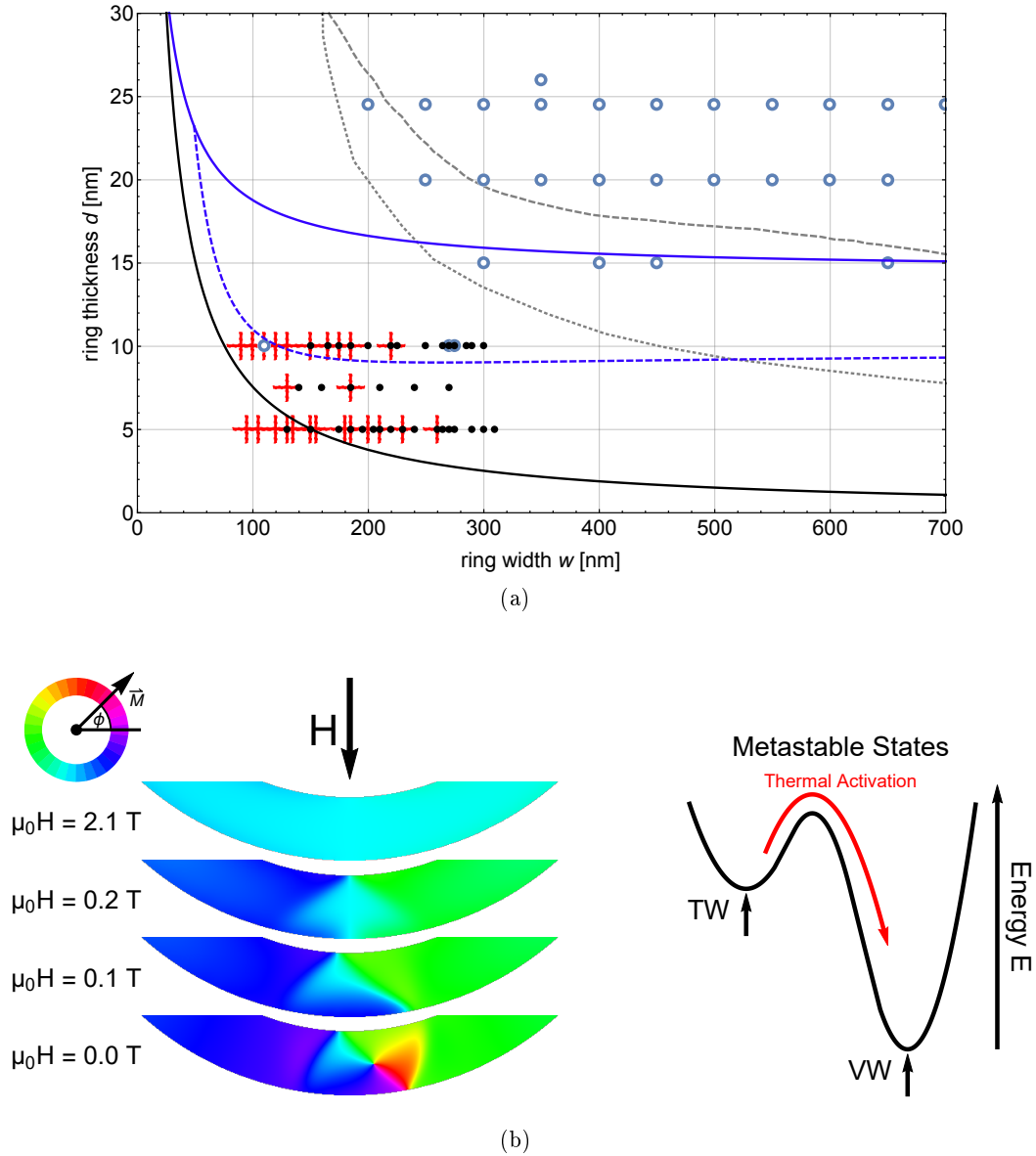
(a)

(b)

Figure 4.5: (a) Experimental phase diagram comparing the different observed spin structures and simulated phase boundaries. A red cross denotes symmetric transverse walls, a black dot asymmetric transverse walls and a blue circle vortex walls. The lowest energy transition is represented by the black solid line. The blue solid line represents the transition from a metastable transverse wall to a stable vortex domain wall by relaxing a field-saturated magnetic half ring, whereas the blue dashed line represents the transition from a symmetric to an asymmetric transverse wall under the same conditions. For comparison the experimental phase boundary from a vortex to a transverse domain wall state for Permalloy (dotted gray) and cobalt (dashed gray) are depicted [130]. (b) shows the nucleation of a vortex domain wall in an Fe half ring with a width of $100\,\mathrm{nm}$ and a thickness of $25\,\mathrm{nm}$ shows a transition through an asymmetric transverse wall at finite external magnetic field as shown in the $0\,\mathrm{K}$-simulations (left). In half ring structures with a lower thickness metastable asymmetric transverse walls can occur for $0\,\mathrm{K}$-simulations. For finite-temperature experiments thermally-driven magnetic fluctuations occur which can trigger a transition from such a metastable transverse wall (TW) to an energetically favorable vortex wall (VW) as seen in the schematic diagram (right).
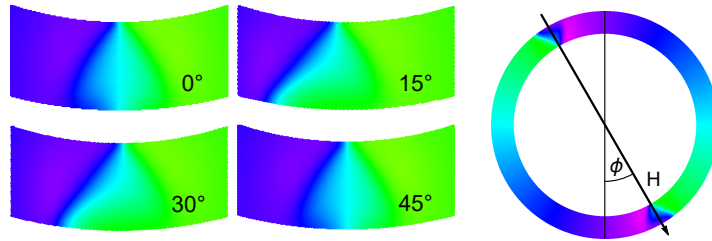
Figure 4.6: The schematic shows the external field direction, ϕ, during a nucleation process. The resulting domain wall state at zero field is influenced by the edge roughness at the nucleation position. For a 100 nm wide and 10 nm thick ring two distinct transitions are observed between 0 and 90°. Here, the final domain wall states for $\phi = 0°$, 15°, 30° and 45° are depicted (The ring structures were rotated accordingly to enable a direct comparison).

4.3   Discussion

Whilst the simulated results provided a good fit to the analytical theory of McMichael and Donahue, the observation of the different types of transverse walls and the observation of transverse domain walls in the region of the phase diagram where the analytical model predicts that the vortex domain wall should be the lowest energy state indicates that there is more going on. Firstly, note that a direct comparison of the experimentally observed states with the analytical model requires that the occurring state is the global energy minimum of the system. However, in practice this would not always be expected to be the case. As mentioned above, the experimental domain wall states are initialized by relaxing the spin structures from saturation. Under these conditions, simulations show that the symmetric transverse wall forms initially [149] and for a range of geometries this domain wall configuration can be a metastable state with an energy barrier that must be overcome in order to nucleate the vortex core as shown in Fig. 4.5 (b), leading to hysteretic switching between the two domain wall types with field [158]. Secondly, the observation of asymmetric transverse walls in addition to symmetric ones demonstrates that the domain wall potential landscape is more complicated than just the simple picture of two stable spin structures, introduced above.

In order to investigate these issues in more detail we performed a new set of simulations where we saturated the half ring along the symmetry axis, y, and gradually relaxed the field in logarithmic steps to obtain the stable zero field states. To gauge the influence of the rectangular grid-induced edge roughness on the domain wall spin configuration we simulated a magnetic state within a full ring and nucleated domain walls by applying the field in four different directions each with distinct edge roughness for the expected nucleation sides (see Fig. 4.6). A comparison with a domain wall nucleated along the y-axis in a half ring with the same width and thickness did not show significant differences, suggesting a minor influence of the reduced symmetry and the subsequent formation of closure domains due to the restriction to a half ring structure [159]. However, the discretization-induced edge roughness depends on the orientation and for nucleations along 15 and 30° altered domain wall states were formed highlighting the importance of magnetic surface modes in the nucleation process. By introducing a refined rectangular grid in the vicinity of a sample edge, effects can be mitigated [160], nevertheless, here we limit simulations to nucleations along the $\phi = 0°$-direction for which the formation of asymmetric domain walls is not favoured.
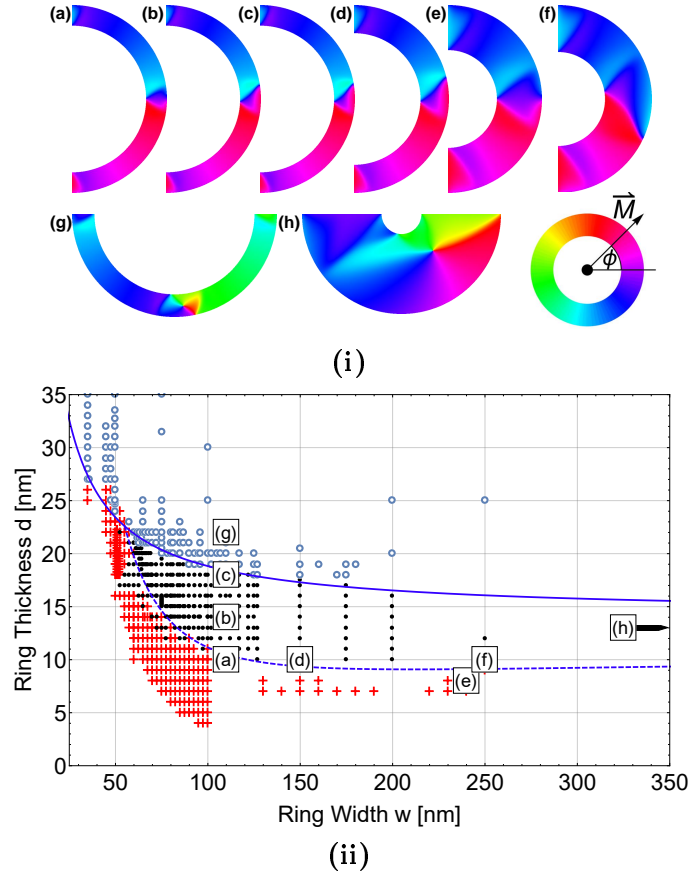
48

Figure 4.7: The simulated spin structures obtained on relaxation of the magnetization from saturation, mimicking the experimental procedure. Three types of domain wall are observed, the vortex [(g) and (h)], symmetric transverse wall [(a) and (e)] and asymmetric transverse wall [(b)-(d) & (f)] as depicted in the selected simulations. (a)-(c) & (g) have width 110 nm, (d) has width 150 nm, (e)-(f) have widths of 240/250 nm and (h) is 400 nm wide. The thicknesses are as follows: (e)-8 nm, (a), (d) & (f)-10 nm, (h)-13 nm, (b)-14 nm, (c)-18 nm and (g)-22 nm. The locations in the phase diagram of the magnetic states (a)-(h) are indicated in the graph (i). The graph furthermore shows the resulting domain wall phase diagram showing three clear regions of stability for the different domain wall types, evolving from symmetric transverse walls for smaller structures to vortex walls in larger structures, through an asymmetric transverse wall for certain intermediate dimensions.

The results of the second set of simulations are presented in Fig. 4.7. Pictures (a)-(h) display typical results across a range of geometries with the wall orientation and colour-code adjusted to enable ease of comparison with the experimental results. Firstly, for the smallest structures such as the 10 nm thick 110 nm wide ring in (a) we see a symmetric transverse wall. On increasing the thickness [(b), (c)] or width [(d), (f)], this then transforms into an asymmetric transverse wall with gradually increased asymmetry. For thinner structures [(e)], meanwhile, the symmetric transverse wall is stable up to higher widths. Finally for the thickest [(g)] and widest [(h)] structures the vortex domain wall emerges. This trend and the form of the spin structures show excellent agreement with the structures observed experimentally. This is clear on comparing e.g. Fig. 4.7 (e) with the
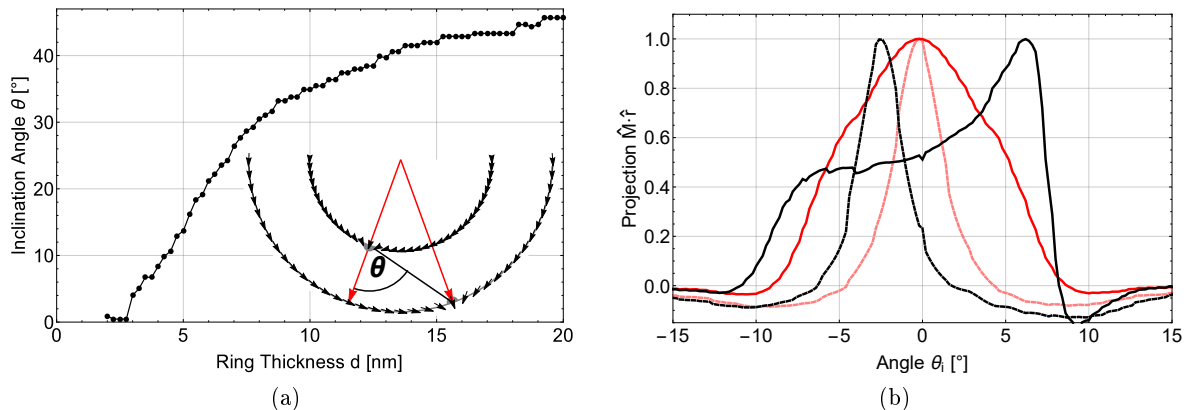
Figure 4.8: (a) displays the change in the inclination angle of the asymmetric transverse wall in a half ring structure as the thickness is reduced from 20 to 2.0 nm for a fixed width of 100 nm omitting a transition to a symmetric transverse domain wall at $d = 11$ nm seen for field relaxed states observed in Fig. 4.7 (i). The inset shows a schematic of the inclination angle, θ, being the angle between the connection line of the extrema in the radial components of the in-plane edge magnetization on the inner and outer perimeters of the ring structure and the radius vector of the inner extreme. (b) shows the projection of the in-plane magnetization at the inner (dashed) and outer edge (solid) of 100 nm wide half rings onto the radial vector. The radial component of the edge magnetization of a symmetric transverse wall (red) in a 10 nm thick half ring shows two coinciding maxima whereas the radial component of the edge magnetization of an asymmetric transverse wall (black) in a 15 nm thick half ring shows a visible difference in the position of the two maxima.

right side of Fig. 4.4 (j) for the symmetric transverse wall, Fig. 4.7 (d)/(f) with Fig. 4.4 (h) and the right of (i) for the asymmetric transverse walls and Fig. 4.7 (g)/(h) with Fig. 4.4 (d)/(e) for the vortex walls.

For a more quantitative treatment the observed domain wall types for all simulations are presented in the graph of Fig. 4.7 (i). When comparing with the previous simulations the first point to note is that now there are two phase boundaries; a principal upper boundary which separates the vortex domain walls from the transverse walls, as before, and a second sub-phase boundary which separates the symmetric transverse walls from the asymmetric ones. The main phase boundary now corresponds to much larger $w \times d$ than before, resulting in a larger range of geometries where the transverse domain walls occur, reflecting the incorporation of states where this spin structure is a metastable state. The new sub-phase boundary is similar in shape to that presented for Py in [131], however, it should be noted that the phase boundary presented in that reference represents the lowest energy configurations on comparing the energies of the three domain wall types. For our Fe phase diagram, which mimics the experiment, we find a larger region where the asymmetric transverse wall is expected and find the asymmetric walls for narrower rings down to $w = 50$ nm as compared to $w = 150$ nm in the previous case of Py.

For the newly observed asymmetric transverse domain walls, Fig. 4.8 depicts the thickness dependence of the inclination angle of relaxed magnetic states in 100 nm wide half ring structures after being initialized with the relaxed asymmetric transverse wall spin structure from the next simulated half ring with larger thickness. The asymmetric trans-

verse domain wall of the 20 nm thick half ring was nucleated using an external magnetic field mimicking the experiment. The asymmetry, θ, of the transverse wall is derived from the difference in angles, $\theta_{Out} - \theta_{In}$, of the two extrema in the radial component of the magnetization at the outer and inner edges of the ring, as shown in Fig. 4.8 (b)/(c) for an asymmetric and symmetric transverse wall, respectively. The asymmetry is then described by:

$$\cos(\theta) = \frac{R_{Out}\cos(\theta_{Out} - \theta_{In}) - R_{In}}{\sqrt{R_{Out}^2 + R_{In}^2 - 2R_{Out}R_{In}\cos(\theta_{Out} - \theta_{In})}} \tag{4.3.1}$$

In the case of $R_{Out}/R_{In} = 1 + w/R_{In}$ being close to 1, the asymmetry, θ, can be reduced to $\cos(\theta) \simeq w/\sqrt{w^2 + b^2}$ with b being the width of the transverse domain wall along the magnetic strip. The angle in the 100 nm thick half ring is observed to undergo a monotonic decrease with decreasing thickness until it drops below 15°. For wider structures the nucleated asymmetric transverse wall can show inclination angles larger than 45° corresponding to a domain wall being bent around the curved ring structure. The thickness dependence can be understood from the different thickness dependencies of the contributing energy terms. The increased asymmetry of the wall reduces the component of magnetization directed normal to the wire edge and hence reduces the demagnetization field, at the expense of an increase in exchange energy. In this sense, the increasing asymmetry of the wall is a precursor to the formation of the full vortex wall. Since the exchange energy is linear in thickness while the magnetostatic energy is quadratic, the energy gain in reducing the demagnetization field becomes more significant with increasing film thickness, resulting in the observed behaviour.

To quantitatively compare the experimental results with the collected simulation results, Fig. 4.5 (a) also includes the phase boundaries from this second set of simulations as represented by the blue lines. What is apparent is that both vortex and transverse domain walls are still observed in the region between the principal solid-line boundaries from the two calculation methods which means that *neither* boundary is a good fit to the experiment. However, one of the remaining factors that we need to consider is the influence of thermal effects, since the simulations only provide the 0 K states, while the experiments are performed at ambient conditions (293 K). While the transverse wall initially forms on relaxation from saturation, it is only a metastable state in the region between the two main phase boundaries and hence thermal activation is able to transform the wall to the vortex configuration which is the lowest energy state, as depicted schematically in Fig. 4.5 (b). Whether this occurs experimentally depends on the measurement temperature and the time profile of the magnetic field sweep as well as the height of the energy barrier, which in the absence of pinning is influenced by the geometrical parameters of the system and the energy costs of available magnetization transformations connecting the initial and final magnetic state. Taking all the experimental and theoretical data together we come to the key result that we can divide the phase diagram into three main regions. Firstly, below the lower principal phase boundary, is a region where transverse domain walls should always be observed in the experiment. Secondly, in the region between the two main boundaries represented by the solid curves, we have a region where either type of wall may be observed, depending on the temperature. As the temperature is increased the effective experimental transition between wall types is expected to move from the upper boundary to the lower one, although due to thermal fluctuations this is not expected to be a rigid boundary at any given temperature and in the vicinity of this effective boundary both types of wall may be observed for the same geometry. Finally, above the upper boundary, is a third region where vortex or more complicated domain walls would always

be expected. This is in agreement with the experimental observations. For our room temperature measurements we observe two vortex domain walls for the 10 nm thick samples at similar widths of 270 and 275 nm, suggesting that the room temperature transition is close to this point. This is also consistent with the fact that we did not observe vortex walls in the thinner samples since this vortex wall would be expected to be stable only for larger widths than for the thicker samples (for such geometries no experimental data were recorded due to the demagnetization field considerations outlined above). We note that whilst we also observe a vortex domain wall for the 110 nm wide, 10 nm thick ring, this is at a much lower width than the other experimentally observed vortex states, suggesting that thermal activation is unlikely to be the only influence in this particular case, as elaborated below.

The final ingredient that needs to be taken into consideration in the experimental work, that is not present in the simulations, is the effect of magnetization pinning due to defects, surface and edge roughness as well as the local influence of magnetocrystalline anisotropy from the small crystallites that compose the polycrystalline layers. Indeed, the latter effect is already evidenced in some of the images due to the emergence of ripple domain contrast, as mentioned above. Such pinning effects can also lead to the stabilization of higher energy metastable spin configurations [161].

To get more insight into the influence of defects we have analyzed a ring structure with a particularly strong edge roughness, which we can gauge from the images of the sample topology which are automatically acquired during the SEMPA imaging (not shown). The domain configurations for opposite sides of this same structure are depicted in Fig. 4.4 (f) & (g), with a vortex wall seen on the wider side of the ring but a transverse wall on the narrower side. Whilst this vortex wall is not inconsistent with the lowest energy calculations, as mentioned above, it is far from the other regions of observed vortex walls. The roughness induced variations in wire width, however, can significantly affect the domain wall energy potential landscapes as seen for artificially defined domain wall traps [141, 142], thereby influencing the observed wall type. Alternatively material defects or a local change of the saturation magnetization [162], for example, could help to favour the vortex wall by acting as preferential nucleation sites for the vortex core in such a structure. The effect of defects varying in kind, strength and position, would also explain the nature and position of the observed experimental phase boundaries. In the previously determined phase diagram for Py the experimental room temperature phase boundary was found to be close to the predictions of the analytical model, indicating that thermal activation is able to have a large effect in that system [130]. Here, however, the experimental phase boundary seems to be in the middle of the region of metastability which can be attributed to the increased pinning in the polycrystalline Fe system showing that the materials properties influence this very strongly. The experimental phase boundaries for Co and Py are included in gray in the figure for comparison. An even more extreme effect of pinning was observed in the Co system where the experimental phase boundary was found to be very close to the upper 0 K limit [130] and more generally it would be expected that it is not only the material that will affect the location of the observed boundary, by way of the intrinsic magnetocrystalline anisotropy, but also the particular growth conditions. Finally, the presence of defects can also explain the broadness of the experimentally observed phase boundary between symmetric and asymmetric transverse walls where for a given geometry both types of walls are found. Such defects are likely to promote asymmetry in the walls, stabilizing the asymmetric configuration over a larger range of geometries than in the simulations of defect free systems and leading to a range of

widths where, depending on the individual structure, either an asymmetric or symmetric transverse wall may form.

4.4   Conclusion

In conclusion, we provide a comprehensive investigation of the complex phase boundaries of different domain wall types by varying the energetic contributions to the stable domain wall spin structures in mesoscopic Fe rings via micromagnetic simulations and high resolution magnetic imaging using SEMPA. The lowest energy domain wall states are well described by the previously developed analytical model of McMichael and Donahue taking into account the competition between exchange and dipolar energy. In order to mimic the experiment, simulations are performed that relax the magnetization states from saturation, revealing in addition to the frequently studied vortex domain wall and symmetric transverse wall, regions of stability of asymmetric transverse domain walls under experimentally relevant initialization conditions.

Here, the general trend from symmetric transverse domain wall for thin and narrow rings, to an asymmetric transverse domain wall with gradually increasing tilt angle for thicker and wider structures and finally to a vortex domain wall for the thickest and widest rings, can be understood as arising from the competition between exchange and dipolar energy contributions which evolve with the geometry. Since domain walls of different type and degrees of asymmetry often display very different dynamic behaviours, it is crucial to understand how different factors can be used to tailor the spin structure and through this the properties of a device. As this present study shows, the experimentally observed domain wall configurations are actually the result of a complex interplay of several factors which all need to be considered.

In comparison to the previously studied Co and Py systems, the $0\,\mathrm{K}$ and room temperature transverse to vortex wall phase transition is shifted to smaller thicknesses and widths, providing more flexibility for the creation of small domain wall devices. Furthermore due to the attractive magnetic properties of iron including a relatively large spin polarization and a lower magnetocrystalline anisotropy than Co, as well as a simple growth procedure, the results presented here show the promise for using Fe in devices based on domain wall motion. For robust device operation it is necessary to find regions of the phase diagram where reproducible domain wall types are observed and our study shows the width and thickness ranges where this is possible. The diffuse boundary regions, for example, would likely be detrimental for reliable device performance, whereas away from these boundaries stable spin states can be expected. Whilst vortex walls are stable for a wide range of geometries at particularly large ring widths and thicknesses, the symmetric transverse walls are only reproducibly seen in very narrow and/or thin structures.

CHAPTER 5

Non-Adiabaticity and Current-Induced Vortex Core Displacement

In chapter 4 we investigated the static spin structures that occured in a particular geometry following a domain wall nucleation process. However, for applications a second key area of research is the dynamic manipulation of magnetic states. Inspired by early experimental and theoretical studies on domain wall dynamics and possible implementations in data processing and storage the influence of the spin current-induced spin-transfer torque on magnetic states became a focus in the field of spintronics [51, 163].

In the case of Bloch and Néel-like domain walls as well as for head-to-head domain walls the spin current-induced average terminal velocity below the Walker-breakdown in the absence of a non-adiabatic spin transfer torque and an external magnetic field, i.e. $\xi = 0$ and $H_{ext} = 0$, has been shown to be zero [52, 164] with a maximum domain wall displacement in the charge current direction of

$$r_{\parallel,max} = -\frac{\mu_B P j_e / e M_S}{4\pi\alpha\gamma M_S},$$

with the gyromagnetic ratio, γ, the saturation magnetization, M_S and P being the spin polarization of the charge current, j_e. After being displaced, the domain wall is found to be distorted at the new equilibrium position and furthermore returns to its original position after the current is reduced to zero. The relaxation to its original position can be circumvented by applying a small oscillating magnetic field during the on-current phase, causing a non-zero terminal velocity in the opposite direction [165, 166], or applying a constant magnetic field while driving the domain wall with a spin current below the Walker breakdown [164]. Above the breakdown current density, periodic transformations of the domain wall are induced by the absorption of angular momentum, causing a finite average terminal velocity approaching $u = \mu_B P j_e / e M_S$ for high current densities [53]. For domain wall-based applications, a high average terminal velocity is required for the desired fast device operation and hence this is considered a figure-of-merit. However in this case, domain wall velocities are increased either by increasing the spin current density or by applying an external magnetic field, both resulting in a higher power consumption and/or increasing device complexity.

The dynamics change dramatically when we consider the effect of a non-adiabatic spin transfer torque on the magnetization dynamics of our system, i.e. $\xi \neq 0$. At least two ξ contributions can be distinguished [167–169]:

$$\xi = \xi_{sr} + \xi_{na}. \tag{5.0.1}$$

The first contribution, ξ_{sr}, is associated with a spin relaxation process of non-equilibrium conduction electrons in the presence of localized electrons which are considered to possess a slow spin dynamics compared to the former [51]. The interaction between the itinerant electrons and the local magnetization is modeled using a s-d Hamiltonian with an exchange interaction strength, J_{sd} [51]. Additionally, its derivation assumes that a change of the spatially varying magnetization, $\boldsymbol{M}$, occurs on a length scale significantly larger than the diffusion length, l_{sf}. Using the diffusion constant, D_S, the transport length can be connected by $l_{sf} = \sqrt{D_S \tau_{sf}}$ [51, 170] to the spin-flip relaxation time, τ_{sf}, of the conduction electrons which is about 10^{-12} s for Permalloy [171]. This results in a diffusion length of $\sim 3 - 6$ nm [172–175], while higher values are reported for unalloyed Ni with 21 ± 2 nm at 4.2 K [176]. Hence, for a system with a small gradient of the local magnetization, e.g. a wide domain wall structure[1], the spin of the non-equilibrium conduction

---

[1]Depending on the film thickness and the domain wall type the domain wall width can be over 100 nm for Permalloy [177–179] and thus significantly larger than the diffusion length. However, the internal spin

electrons mistracks slightly the non-uniform magnetization within τ_{sf} and exerts a torque on the system with a coupling strength of $\xi_{sr} = \hbar/J_{sd}\tau_{sf} \equiv (l_{sd}/l_{sf})^2$ [51]. Assuming $l_{sd} = 0.8\,\text{nm}$ [180] and $l_{sf} \approx 4.5\,\text{nm}$ this expression results in $\xi_{sr} \approx 0.03$ for Permalloy. Although the spin-flip relaxation time was introduced as a phenomenological parameter in Ref. [51], different mechanisms are known to induce spin relaxation as well as a non-adiabatic spin transfer torque and thus modify ξ [181–183], e.g. scattering with impurities and electrons, or spin-orbit interaction.

The second contribution of the non-adiabatic spin transfer torque, ξ_{na}, is associated to effects present in systems with high magnetization gradients on small length scales, e.g. narrow domain wall structures. In these systems the mistracking of a conduction electron spin extends outside the high gradient region which leads to a non-local feedback on the magnetization [184, 185] and a decrease of the non-adiabatic torque strength with the domain wall width [184, 186]; however, a sharp domain wall structure stifles the decrease which highlights the importance of the spin structure [184]. Two mechanisms have been proposed to describe this non-adiabatic spin transfer torque contribution and involve the precessional motion of single-electron spins around the effective magnetic field [184] and the dephasing and relaxation of the itinerant spin in the presence of spin-independent disorder [186]. For instance, in Py the latter mechanism of the dephasing and relaxation is expected to enhance ξ_{na} considerably for magnetic vortex structures due to the spin diffusion in the vicinity of the vortex core which leads to a reduction of the renormalized effective spin diffusion length [186]. However, for transverse domain walls with a width over $5\,\text{nm}$ the mechanism leads to moderate to no increase in the domain wall velocity and the non-adiabaticity [186]. The influence of the precessional motion of single-electron spins on this magnetic structure is comparably small for Py and is expected to have an effect at sharper domain wall spin configurations [186]. For domain walls with widths of a few lattice constants an additional linear momentum transfer occurs due to a reflection of the itinerant electrons and is proportional to the electrical domain wall resistivity [187, 188]. The resulting contribution to the equation of motion resembles in its appearance the non-adiabatic spin transfer torque [189].

Although the non-adiabatic torque contributions differ in the originating mechanism, the local or non-local effects can be captured by effective local parameters "for all but extreme cases" [185] and the Landau-Lifshitz-Gilbert equation can be used to describe the magnetization dynamics. The torque, $\boldsymbol{T}$, acting on the magnetization, $\boldsymbol{M}$, generated by a spin polarized current, $P\boldsymbol{j}_e$, P being the spin polarization of the charge current, can be written as

$$\boldsymbol{T}(\boldsymbol{r}) = -\frac{P}{eM_S}(\boldsymbol{j}_e \cdot \boldsymbol{\nabla})\boldsymbol{M}(\boldsymbol{r}) - \xi\frac{P}{eM_s^2}[\boldsymbol{M}(\boldsymbol{r}) \times (\boldsymbol{j}_e \cdot \boldsymbol{\nabla})\boldsymbol{M}(\boldsymbol{r})]. \tag{5.0.2}$$

Restricting considerations to a shallow pinning potential and spin polarized currents above the depinning threshold and below the critical current density, the terminal velocity, $\boldsymbol{v}_{DW}$, of a domain wall [169] is given by

$$\boldsymbol{v}_{DW} = \langle \dot{\boldsymbol{r}}_{DW} \rangle = \frac{\xi}{\alpha}\frac{\mu_B P}{eM_S}\boldsymbol{j}_e = \frac{\xi}{\alpha}\boldsymbol{u}. \tag{5.0.3}$$

For a given combination of $\boldsymbol{u} = \mu_B P\boldsymbol{j}_e/eM_S\alpha$, a higher domain wall velocity can therefore be achieved by increasing the non-adiabatic coefficient, ξ, resulting in a faster angular momentum transfer from the spin current to the domain wall.

---

structure of a domain wall can feature high gradient regions which are possibly the determining factors for the strength of the non-adiabatic spin transfer torque.

Measurement	Ref.	$10^2\xi$	$10^2\alpha$	ξ/α
Spin wave	[190]	3.3 ± 1.2	0.82	4.0 ± 1.5
	[191]	3.5 ± 1.1	0.75 ± 0.3	4.7 ± 1.5
Nano bridge	[192]	2.7 ± 0.1	0.8	3.4 ± 0.1
Transverse wall hopping	[193]	1.0 ± 0.4	0.8	1.3 ± 0.5
Vortex wall hopping	[193]	7.3 ± 2.6	0.8	9 ± 3
Vortex wall excitation	[194]	1.8	0.9	2.0
Domain wall depinning	[195]	40 ± 1.8	n.a.	n.a.
Walker breakdown field	[196]	~ 0.8	~ 1.0	~ 0.8
Domain wall velocity	[197]	~ 0.7	~ 1.0	~ 0.7
Double vortex wall displacement	[198]	n.a.	n.a.	0.96 ± 0.02
Vortex wall displacement	[199]	13 ± 1	0.8	16 ± 1
	[200]	~ 2.6	0.8 ± 0.2	~ 3.2
Vortex core precession	[200]	~ 2.6	0.8 ± 0.2	~ 3.2
	[201]	15 ± 2	1.6 ± 0.1	9.2 ± 0.8
	[202]	6.1 ± 0.6	0.6 ± 0.1	10 ± 2
Vortex core displacement	[203, 204]	12 ± 6	0.8	15 ± 7.5
	[205]	12.1 ± 2.3	0.85 ± 0.06	14 ± 3

Table 5.1: Summary of experimental estimates of non-adiabaticity, ξ, and damping parameters, α, for Py-based systems derived using different measurement schemes.

Theoretical considerations show that one contribution to ξ depends on the spin-flip relaxation time, τ_{sf}, of the conduction electrons [51] and the gradient of the magnetization [184, 206] can be used to tailor the local non-adiabatic coefficient, e.g. the ξ for a magnetic vortex core is found to be significantly higher than that in wide domain walls with a slowly varying magnetization which can be attributed to the vortex core region in the former case [193]. Thus, for a given magnetic material the effective ξ can be modified by the shape and size of magnetic structures. Furthermore, in experiments dopants have been observed to influence ξ, e.g. for vanadium and holmium-doped Permalloy an increase in ξ on increasing dopant-concentration has been observed [199, 207].
However, the relationship between ξ and the damping coefficient, α is still under debate [164, 183, 208, 209] and detailed experimental studies are required to discriminate between existing models, e.g. for itinerant ferromagnetism different spin-relaxation processes for the conduction electrons due to magnetic and spin-orbit impurities imply $\alpha \neq \xi$ [210]. Specifically for a weak influence of the impurity potentials, α and ξ are of the same order [208] and have been shown to be similar for certain models [163, 183, 211].
Various methods are employed to determine ξ experimentally for different magnetic systems and to compare it to the damping coefficient. Initially reported ξ values were derived from the observed current-induced vortex domain wall displacement below the Walker breakdown and from the critical magnetic field for the field-induced Walker breakdown in straight Permalloy nanowires. The observations suggested that ξ and α are similar, e.g. $\xi \sim 0.007 \sim 0.7\alpha$ [197] and $\xi \sim 0.008 \sim 0.8\alpha$ [196]. However, subsequent current-induced vortex domain wall displacement measurements indicated that ξ is larger than α, e.g. $\xi = 0.13 \pm 0.01 = (16 \pm 1)\alpha$ [199] and $\xi \sim 0.026 \sim 3.2\alpha$ [200]. A close examination of thermally activated domain wall hoping between pinning sites in the presence of small charge currents ($\|j_e\| \lesssim 3 \cdot 10^9 A/m^2$) in Permalloy nanowires implied $\xi = 0.073 \pm 0.026$ and $\xi = 0.010 \pm 0.004$ for vortex domain walls and transverse domain walls, respec-

tively [193]. Moreover, by determining the current-dependent switching field of a Permalloy nanobridge via measurement of the electrical resistance at constant charge currents while performing major hysteresis loops, a value of $\xi = 0.027 \pm 0.001 = (3.4 \pm 0.1)\alpha$ was determined [192]. Another measurement scheme to determine the non-adiabaticity is based on current-induced spin wave excitations in thin films and their time-domain characteristics which enable the simultaneous measurement of ξ and α, e.g. Sekiguchi et al. [190] reported $\xi = 0.033 \pm 0.012 = (4.0 \pm 1.5)\alpha$. More recent studies investigated the alternating current-induced gyration of the vortex core within a Landau state and a vortex domain wall and deduced $\xi = 0.15 \pm 0.02 = (9.2 \pm 0.8)\alpha$ [201] and $\xi = 0.061 \pm 0.006 = (10 \pm 2)\alpha$ [202], respectively, and thus support $\xi > \alpha$.

Overall, it can therefore be seen that there is a large range in the reported values of both ξ and ξ/α. In general the published results support the existence of higher ξ values for higher magnetization gradients, yet this does not adequately describe all results on its own. A recent paper suggested an additional topological contribution to ξ which goes same way to resolve the some of the discrepancies. Nevertheless, it is difficult to disentangle the relation between ξ and α due to the other contributions when comparing different measurement techniques and different spin configurations. It is therefore highly desirable to obtain ξ by the same method for two or more comparable states with different α.

In this work, we follow a proposed measurement scheme for the non-adiabatic coefficient [212]. In disk-shaped thin film elements, we observe the displacement, $\boldsymbol{r}$, of the core region of vortex states as a function of an applied current for different current directions and vortex state configurations with chiralities[2], c, and polarities, p. Previous measurements based on this scheme suggest $\xi = 0.12 \pm 0.06 = (15 \pm 7.5)\alpha$ [203, 204] and $\xi = 0.121 \pm 0.023 = (14 \pm 3)\alpha$ [205] for vortex states in disk-shaped and for Landau states in square-shaped thin film elements of undoped Permalloy, respectively.

Thus, the purpose of this work is to extend previous studies, investigate the effect of a dopant on ξ and shed further light on the relationship between ξ and α. In the following, we introduce the used theoretical model.

5.1 Theoretical Description of Current-Induced Vortex Core Displacement

The displacement of the vortex core due to a force, $\boldsymbol{F}$, for an elastically deformed vortex state can be modeled using the Thiele equation [54, 212, 213]

$$0 = \boldsymbol{F} + [\boldsymbol{G}_0 \times (\dot{\boldsymbol{r}} + \boldsymbol{u})] + D_\Gamma \alpha \dot{\boldsymbol{r}} + D_0 \xi \boldsymbol{u}.$$

Here, the non-adiabatic coefficient ξ is connected to a related coefficient, β, via

$$\beta = \frac{\xi}{1 + \xi^2}. \tag{5.1.1}$$

The dissipation of energy in the system is described by the two related coefficients D_Γ and D_0. D_0 is the diagonal element of the dissipation tensor and depends on the magnetic state. The phenomenological constant, D_Γ, is attributed to the spatially non-homogenous behavior of magnetic moments due to the deformation of the magnetic state, e.g. the velocity of the vortex core to the center of the disk compared to the velocity of magnetic

---

[2]Here, c denotes the sense of rotation of the magnetic moments and p the orientation of the vortex core. A schematic representations of three vortex states are depicted in Fig. 5.1

moments near the edge of the sample [212]. The gyrovector, $\boldsymbol{G}_0$, points in the opposite direction to the vortex core and together with the current direction, $\boldsymbol{j}_e = eM_S/P\mu_B\boldsymbol{u}$, defines a right handed basis

$$\boldsymbol{e}_\parallel = \boldsymbol{j}_e/\|\boldsymbol{j}_e\|$$
$$\boldsymbol{e}_\perp = [\boldsymbol{e}_z \times \boldsymbol{e}_\parallel]$$
$$\boldsymbol{e}_z = -p\boldsymbol{G}_0/\|\boldsymbol{G}_0\|.$$

In this basis, the force acting on the vortex core with a small deviation from its zero-current equilibrium position can be written as [212, 214]

$$\boldsymbol{F} = -(m\omega^2 r_\parallel + \mu_0 M_S HDdc)\boldsymbol{e}_\parallel - m\omega^2 r_\perp \boldsymbol{e}_\perp. \tag{5.1.2}$$

Here, $\mu_0 M_S HDdc$ describes the influence of an unbalanced Oersted-field on a vortex state with chirality, c, due to an inhomogeneous charge current flow through a sample with thickness, d, and diameter, D. In the case of $\boldsymbol{j}_e = 0$, this force, $\boldsymbol{F}$, reduces to a simple confining potential with stiffness, $m\omega^2$. The on-current equilibrium position of the vortex core is reached for $\dot{\boldsymbol{r}} = 0$ and can be derived from the extended Thiele equation

$$0 = \boldsymbol{F} + [(-p\|G_0\|)\boldsymbol{e}_z \times u\boldsymbol{e}_\parallel] + D_0\xi u\boldsymbol{e}_\parallel$$
$$= (-\mu_0 M_S Hldc - m\omega^2 r_\parallel + D_0\xi u)\boldsymbol{e}_\parallel + (-m\omega^2 r_\perp + pG_0 u)\boldsymbol{e}_\perp,$$

which can be rewritten as

$$r_\parallel = -\frac{\|G_0\|}{m\omega^2}\left(\mu_0 M_S Hldc + \frac{\|D_0\|}{\|G_0\|}\xi u\right) \tag{5.1.3}$$

$$r_\perp = -\frac{\|G_0\|}{m\omega^2}(pu) \tag{5.1.4}$$

and the dependance of $\boldsymbol{r}$ on the polarity, p, and chirality, c, can be used to separate the contributions of Oersted-, adiabatic- and non-adiabatic torque (see Fig. 5.1) and determine the non-adiabatic coefficient [204, 205, 212],

$$\xi = \frac{p}{2}\frac{\|G_0\|}{\|D_0\|}\frac{r_\parallel(c, p, \boldsymbol{j}) - r_\parallel(-c, -p, -\boldsymbol{j})}{r_\perp(c, p, \boldsymbol{j})}. \tag{5.1.5}$$

The prefactor $\|G_0\|/\|D_0\|$ is determined for the specific geometry realized in the sample fabrication process using the micromagnetic simulator, MicroMagnum [47]. Here, a disk structure of 4300 ± 2 nm in diameter is simulated on a two-dimensional grid with 1434×1434 rectangular cuboidal cells having in-plane edge length of 3 nm and a thickness of 25 nm. Assuming an uncertainty of one cell for the vortex core position we derive $\|D_0\|/\|G_0\| \approx 3.24 \pm 0.01$. Alternatively, an analytical expression,

$$\|D_0\|/\|G_0\| = 0.5 ln(2d_{Disk}/d_{VC}),$$

depending on the disk diameter, d_{Disk}, and the vortex core diameter, d_{VC}, and evaluates to ≈ 3.26 for the realized sample geometry with d_{VC} being derived using previously reported theoretical models [215]. Thus, $\|G_0\|/\|D_0\|$ shows the same exemplary agreement with the numerical simulation as reported for a 30 nm thick Py film [216].
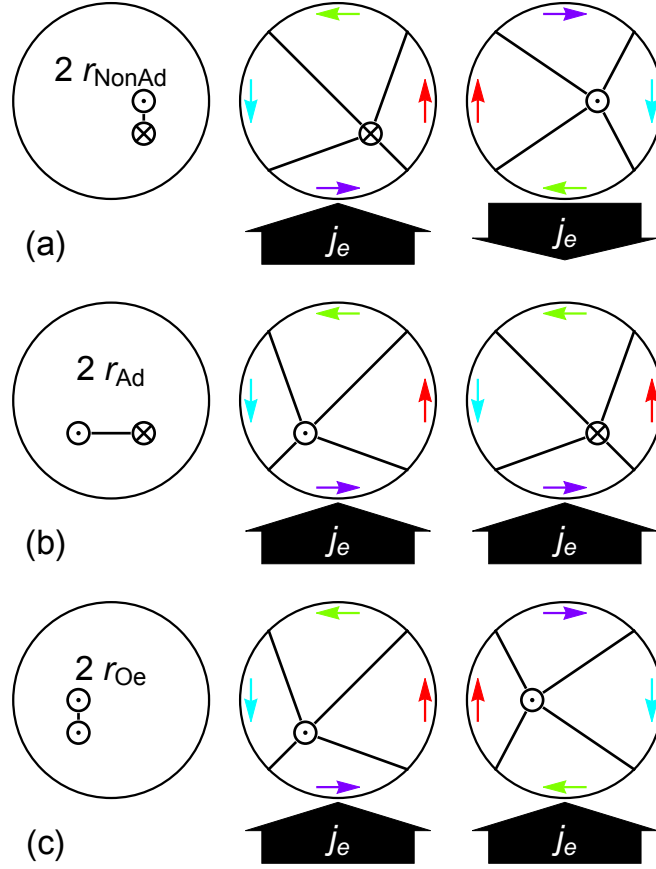
Figure 5.1: Schematics of current-induced displacement of the out-of-plane magnetized core region in magnetic flux-closed vortex states. The displacement direction corresponds to the expected displacement of the core region in a magnetic vortex state used in our experimental setup. By combining the core displacements found in states with distinct chiralities, c, and/or polarities, p, different contributions of the displacement can be separated. Here, the rotation direction of the magnetic flux is indicated by arrows. A counterclockwise rotation is assigned with a chirality of $c = +1$; $c = -1$ denotes the opposite rotation direction. A positive polarity, $p = +1$, of the core region is depicted with a dot, whereas a negative polarity, $p = -1$, is depicted as a cross. The theory is valid for small displacements where the confining potential leads to a linear force. (a) The non-adiabatic contribution, r_{NonAd}, can be extracted by measuring the difference in displacement for opposing current directions in states differing both in polarity and chirality. (b) The net displacement perpendicular to current direction, $2r_{Ad}$, of two states with the same chirality and current density, i.e. which differ only in polarity, can be used to extract the adiabatic contribution. (c) Under the influence of the same current density, the difference in displacement, $2r_{Oe}$, in two states with identical polarity, but with opposing chirality, can be attributed to the Oersted-field. In accordance with equation 5.1.3, the net displacement of (a)/(c) is along the current direction which can be used to eliminate the Oersted-field contribution and extract the non-adiabatic coefficient (see equation 5.1.5). Adapted from [212].

5.2 Preparation and Characterization of Dysprosium-doped Permalloy Thin Films

The dynamic behaviour of a spintronic device depends on a set of material properties among which are the saturation magnetization, the magnetic anisotropy, the damping coefficient, α, and the non-adiabatic coefficient, ξ. Hence, tailoring these properties is of particular interest and different techniques have been investigated to allow parameters to be changed independently. For the investigated host material, Permalloy, the saturation magnetization can be tuned by implanting Gd or Eu without altering the damping [16] and the magnetic anisotropy can be altered without influencing the saturation magnetization by changing the shape, size and growth conditions [217, 218]. This section reports magnetic properties and damping coefficients for our thin film samples.

Implanting dopants into a host material is a common technique for altering material properties. In particular, the introduction of rare-earth dopants into Permalloy enables a systematic study of the relation of the non-adiabaticity, ξ, and the damping coefficient, α. First systematic studies of the ferromagnetic resonance signal (FMR) for certain materials indictated a linear increase of α with the dopant concentration [16, 219].

Based on measurements of the ferrimagnetic linewidth broadening of doped yttrium iron garnet, the slow relaxing impurity model has been proposed, assuming a splitting of the $4f$ shell of the rare-earth element due to the exchange field of the $5d$ shells of the iron sublattice [15]. Due to an exchange interaction between the $3d$ and $5d$ shell within the $Ni_{80}Fe_{20}$ alloy, a precession of the magnetic moments induces a change of the $4f$ level splitting and subsequently generates an effective transverse magnetic field acting on the $3d$ shell of the alloy [16]. The strength of the effect depends on the dopant concentration as well as the dopant material ranging from little to no effect for gadolinium and europium to a strong influence for terbium and dysprosium [16, 219].

Here, we restrict our study to the rare-earth element dysprosium with a reported induced α increase of 0.036 /at.% [16] and prepare four thin film samples on silicon and sapphire substrates with different dopant concentrations concurrently with our doped-Py disk structures (see section 3.7 for the production steps). The film synthesis is done using simultaneous deposition from two evaporators via molecular beam epitaxy (MBE) in a UHV chamber with a base pressure of $\sim 10^{-9}$mbar. Low Dy doping levels are obtained by decreasing the deposition rate-ratio for Dy and Py prior to the film fabrication. Due to the chamber geometry, two separate deposition rates for the evaporators can not simultaneously be measured and are therefore determined by sequentially interrupting the Dy and the Py evaporation. First, suitable parameters for a high deposition rate between $8 - 14$ nm/h for Py^3 are obtained followed by a measurement of the Dy deposition rate for $1.0 - 1.5$ h to obtain a low reliable rate of $\lesssim 1$ nm/h. Now, the Py evaporation is initiated again and a ~ 26 nm thick thin film is deposited and a gold capping is added to prevent oxidation of the samples. Following the procedure, we obtained four Py thin films with 0.00 at.%, 1.49 at.%, 1.96 at.% and ~ 8 at.% dysprosium concentration[4].

The influence of the dopant concentration on the magnetic hysteresis of thin film samples is investigated using longitudinal magneto-optical Kerr magnetometry (MOKE).

---

[3]The undoped Py thin film was deposited with a lower rate of ~ 4 nm/h.

[4]We thank Prof. Dr. Jürgen Fassbender, Dr. Julia Osten and Jonathan Ehrler from the Helmholtz Zentrum Dresden Rossendorf for determining the dopant concentration using Rutherford-backscattering spectrometry (RBS) measurements on the 1.49 at.% and the 1.96 at.% thin film samples. The dopant concentration of the ~ 8 at.% thin film was determined using energy dispersive x-ray (EDX) spectroscopy.

(a)   (b)
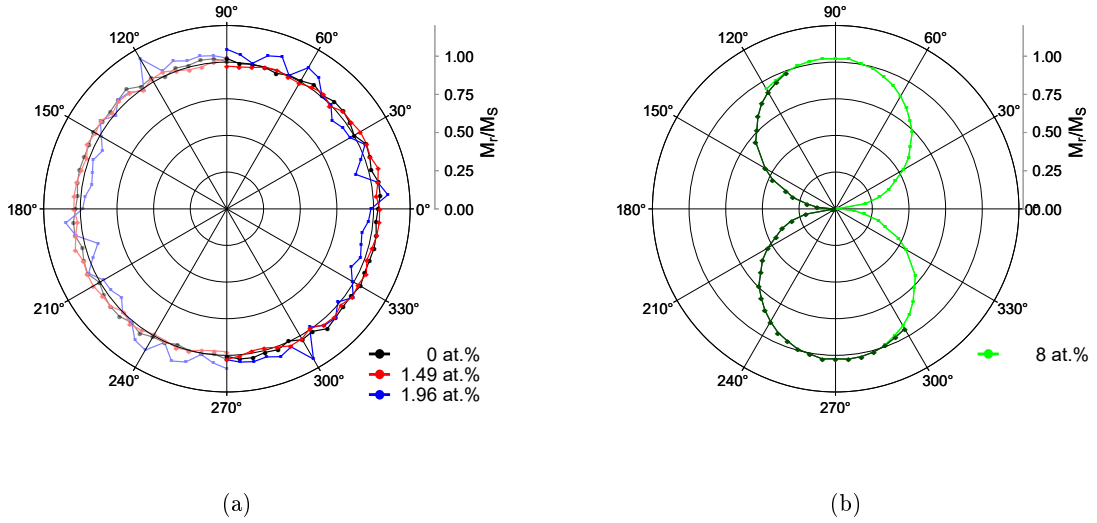
Figure 5.2: The graphs show the angular dependence of the normalized remanent magnetization, M_r, for various thin films after saturating them in an external field pointing in the indicated direction, as measured with MOKE. Each thin film was grown on a sapphire substrate and is protected against oxidation with a thin Au capping layer. (a) depicts the derived values for 0 at.% (black), 1.49 at.% (red) and 1.96 at.% (blue) Dy dopant concentration in a 27 nm (black) and two 26 nm (red/blue) thick Permalloy films. In contrast to the flat angular curves seen in (a), a $\sim 8\,\%$-doped Py film with a thickness of 28 nm in (b) shows a pronounced uniaxial anisotropy which affected the remanent magnetic states of the associated contacted disk structures grown on Si/SiO_2 substrates (Dark green points are generated by rotation of the derived M_r/M_S values indicated by light green).

At room temperature, the samples are saturated using an in-plane magnetic field up to 50 mT and the normalized remanent magnetization is estimated from the signal trend close to zero field (see Fig. 5.2). The data shows no significant magnetic anisotropy for the low-doped Permalloy thin films, however, from Fig. 5.2 (b) it can be seen that a strong uniaxial anisotropy exists for thin films with a higher dopant concentration and the corresponding hysteresis loops yielded an uniaxial anisotropy field, H_K, of ≈ 4 Oe. This observation is consistent with measurements on epitaxial-grown iron thin films which indicated an increase of the uniaxial anisotropy with the dysprosium concentration [220]. Additionally, a small uniaxial field of less than 5 Oe was reported for a series of poly-crystalline Dy-doped Py thin films with thicknesses between $10 - 30$ nm grown on glass substrates with Ta seed layers [16]. In both cases, a reduction of the saturation magnetization was observed which is associated which the antiferromagnetic coupling between the $4f$ electrons of the rare earth element and the $3d$ electrons of the transition metal alloy, Permalloy. Subsequently, we investigate the saturation magnetization for temperatures down to 10 K using a superconducting quantum interference device (SQUID) and observe a strong temperature dependance for 8 at.% dopant concentration (see Fig. 5.3). The inset shows the corresponding remanent magnetic states for 8 at.% doping in a nanostructured disk indicating a decreasing signal-to-noise ratio at lower temperatures. The initial dynamics and especially the transient oscillation of a magnetic vortex state before
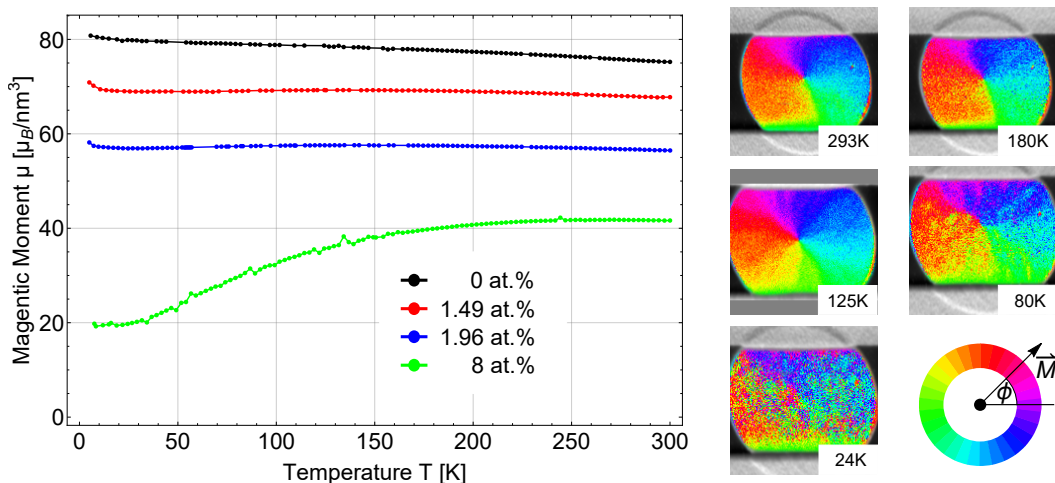
Figure 5.3: Temperature dependance of the saturation magnetization, M_S, for Permalloy with different dopant concentrations measured every $3\,\mathrm{K}$ during a temperature sweep from 300 to $10\,\mathrm{K}$. At $300\,\mathrm{K}$, the saturation magnetization of the doped thin films is reduced with respect to the undoped samples by $\sim 10\,\%$ for $1.49\,\mathrm{at.\%}$ (red line), by $\sim 25\,\%$ for $1.96\,\mathrm{at.\%}$ (blue line) and by $\sim 45\,\%$ for $8\,\mathrm{at.\%}$ dysprosium (green line). While the undoped (black line) and the two slightly doped samples exhibit small variations in M_S of less than $7\,\%$ within the displayed temperature range, a drop of more than $50\,\%$ is observed for a dopant concentration of $8\,\mathrm{at.\%}$. The inset shows the corresponding color-coded in-plane magnetization via SEMPA of the remanent state for the strongly doped sample in an electrically contacted $4.3\,\mu\mathrm{m}$ diameter disk grown on a Si/SiO_2 substrate.

reaching its quasi-equilibrium configuration is influenced by the damping coefficient, α. However, this time regime is not accessible for our measurement setup. To measure α we rely on the external magnetic field-induced collective precession of the magnetic moments. Here, the magnetic field, H_{Ext}, is applied in a direction parallel to the film surface and the field-dependent ferromagnetic resonance (FMR) is detected[5] (see Fig. 5.4). The field-dependent FMR position for a low anisotropy material is described by the Kittel-precession mode [107, 221]:

$$f = (2\pi)^{-1}\gamma\sqrt{H_{Ext}(H_{Ext} + M_S)}. \tag{5.2.1}$$

Here, the resonance line shape has a FWHM linewidth, ΔH, described by

$$\Delta H = \Delta H_0 + 4\pi\alpha\gamma^{-1}f_{FMR}. \tag{5.2.2}$$

It depends on the intrinsic Gilbert damping coefficient, α, and an inhomogeneous broadening, ΔH_0, due to a spatially dependent resonance condition and a possible magnon-magnon scattering contribution [109–111]. By extrapolating the observed linewidth behaviour to zero excitation frequency, a small inhomogeneous broadening contribution of $0.4\,\mathrm{Oe}$ is found. For the doped thin films a large increase in the linewidth at $4.5\,\mathrm{GHz}$ is seen for an increasing doping concentration. However, a full frequency scan was not possible due to the reduction in peak height at higher frequencies; hence the resulting signal could no longer be accurately be measured in the used setup.
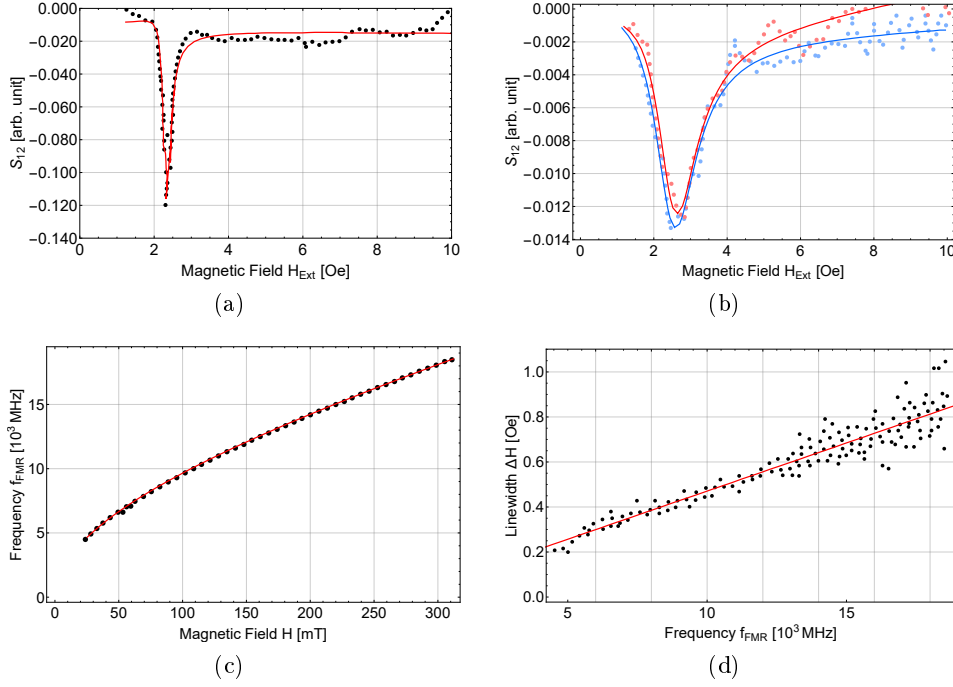
Figure 5.4: FMR absorption spectra at an excitation frequency, f_{FMR}, of 4.5 GHz for (a) 27 nm and (b) 26 nm thick doped Permalloy films with (a) 0.00 at.%, (b) 1.49 at.% (red) and 1.96 at.% (blue) dysprosium content. The corresponding FWHM linewidths are (a) 0.2 ± 0.01 Oe, (b) 1.24 ± 0.15 Oe (red) and 1.32 ± 0.15 Oe (blue). The saturation magnetization, M_S, of the undoped Permalloy film is derived using the data depicted in (c) and equation 5.2.1. Using equation 5.2.2, (d) allows a more precise determination of the damping constant, α, for the undoped film.

We assume a negligible inhomogeneous broadening contribution and, thus, derive the damping coefficient using $\alpha = \gamma \Delta H/(4\pi f)$. For the doping levels used, this is a reasonable assumption based on the measurements in [16], although there an increased inhomogeneous contribution was found for higher doping levels. The measured and derived values are summarized in table 5.2.

5.3   Changing the Magnetic State via External Magnetic Fields

The experiment relies on the difference in response of the four possible magnetic vortex state configurations under applied current (see Fig. 5.1). Hence, to ensure comparability between magnetic states, the chirality and/or polarity of a state in a specific disk structure is changed in-situ. The polarity can efficiently be switched with a short burst of alternating magnetic fields [222, 223] while a specific chirality can be favoured by tailored inhomogeneous magnetic fields [224]. However, we are restricted to quasi-static homogeneous fields with up to ≈ 180 mT preventing a sophisticated control of the magnetic state. Therefore, an in-plane field is applied to expel the vortex core region from the disk structure (see Fig. 5.5) followed by a 90° turn of the sample resulting in an out-of-plane field. After decreasing the field to zero, the sample is turned back to its original orientation followed by an alternating in-plane field with decreasing amplitude to demagnetize the sample. The chirality of the emergent magnetic state is observed directly, however, the polarity is inferred during the measurement using the response under applied current.
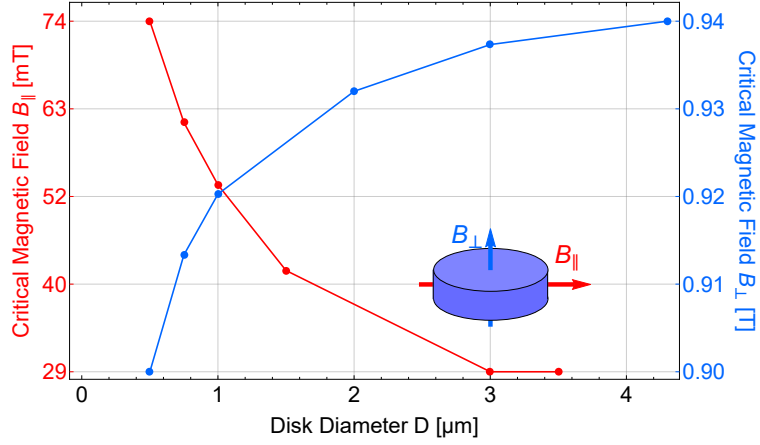
Figure 5.5: Simulated critical external magnetic field necessary for vortex core expulsion in disks. The structure was simulated on a grid with rectangular cuboidal cells having an in-plane lattice constant of 3 nm and a single 25 nm thick cell in the out-of-plane direction. The external field was increased by 1 mT till the core region was expelled. The critical out-of-plane field approaches the thin film limit with $B_\parallel = \mu_0 M_S$. The inset shows the field direction for two considered cases.

Figure 5.6: Contact structures in different conditions after measurement. (a) shows a sample which has retained its initial structure while (b) shows a trench in the Permalloy (purple) at the gold (yellow) edge creating two separate Permalloy structures with altered shape anisotropies and non-vortex state remanent spin configurations. (c) shows the outcome of a stronger electromigration event.
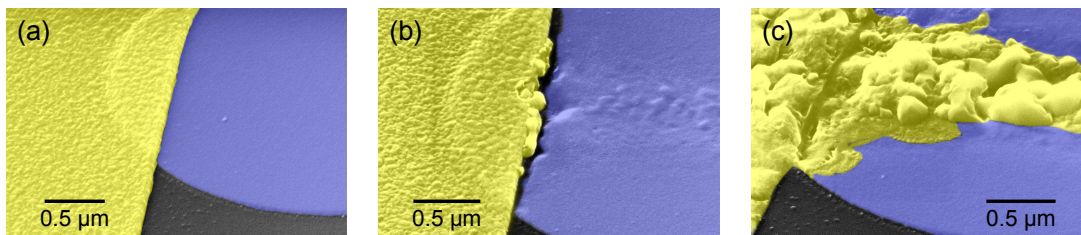
5.4 Results

Due to limitations of our SEMPA setup, we are bound to observation of vortex core displacement under constant current instead of a pulsed approach[6]. Due to Joule heating the disk structure is subject to a large thermal load due to the high employed current densities necessary to observe appreciable vortex core displacement. The electrically contacted disks are deposited on a Si/SiO_2 substrate and the low thermal conductivity of the thin naturally grown SiO_2-layer [117–119] hampers a fast heat transfer to the substrate. Therefore in order to prolong the lifetime and thermal stability of the element [102, 225], we cool the substrate down to a temperature of $\approx 24\,\mathrm{K}$ resulting in a reduced sample resistance of $16 - 25\,\Omega$ [7]. However, the thermal resistance of the insulating SiO_2-layer is strongly increased below $50\,\mathrm{K}$, causing a heat accumulation. Nonetheless the sample temperature is stabilized due to the negative slope of the thermal conductivity of SiO_2 [227]. Previous experiments were performed at higher temperatures and required a substrate with a high thermal conductivity, e.g. single crystalline diamond [205], or restricted the current application by using current pulses [204] to counteract the high base temperature and/or a high sample resistance. The structural integrity of our samples was confirmed for current densities of $1.1 \cdot 10^{12} A/m^2$ (over a period of hours) and $\approx 1.5 \cdot 10^{12} A/m^2$ (for several minutes with a steady increase in temperature; see Fig. 5.6 for contact structures in different states of deterioration).

However, for current densities above $\approx 0.8 \cdot 10^{12} A/m^2$ (undoped Permalloy), $\approx 0.5 \cdot 10^{12} A/m^2$ ($PyDy(1.49\,\mathrm{at.\%})$) and $\approx (0.4-0.5) \cdot 10^{12} A/m^2$ ($PyDy(1.96\,\mathrm{at.\%})$) the vortex states were observed abruptly to transform to other metastable states, and thus the magnetic systems require reinitialization. Nevertheless, below these current densities reproducible state transformations are predominant at low temperatures and enable the investigation of the current-dependent vortex core displacement. The vortex core position is determined with sub-pixel precision using a noise-resistant cross-correlation algorithm (see section 7.2). However, a reasonable comparison with an analytical vortex state requires a correction of the measured in-plane asymmetry which leads to an additional uncertainty in the position (see section 7.3).

---

[6]See Chapter 6 for descriptions of ongoing adaptions to the system which will permit more flexible imaging modes.

[7]The reported resistances include $\approx 8 - 10\,\Omega$ originating from the external contacts of the measurement setup. Excluding every resistance beside the contributing disk, we expect the undoped Py structure to have a resistance of $\approx 16\,\Omega$ at room temperature assuming a specific resistivity of $3.5 \cdot 10^{-7}\,\Omega\mathrm{m}$ [226].
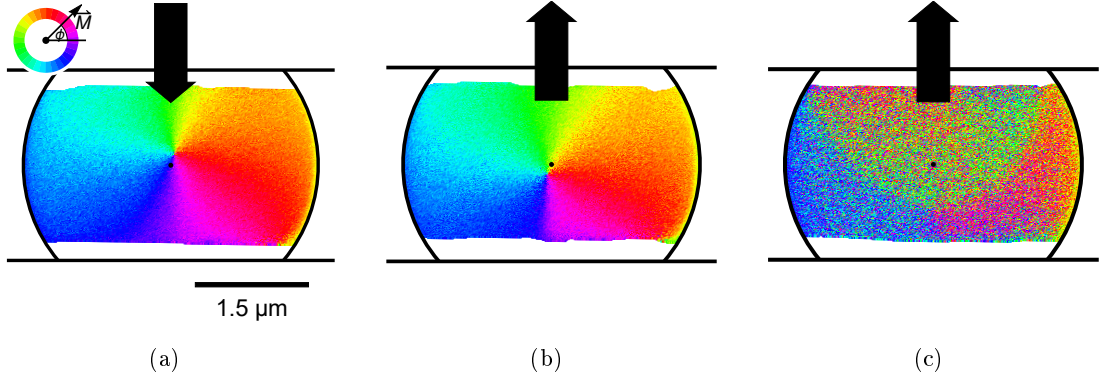
Figure 5.7: Current-induced modification of a magnetic vortex state with $c = +1$ and $p = +1$ in a single undoped-Permalloy disk for (a) $j_e = -0.5 \cdot 10^{12}\,\text{A/m}$, (b) $j_e = +0.5 \cdot 10^{12}\,\text{A/m}$ and (c) $j_e = +1.1 \cdot 10^{12}\,\text{A/m}$. (a)/(b) show asymmetric magnetic states with vortex cores at positions approximately connected by a point reflection through the center of the disk. The transformed magnetization in (c) is retained after decreasing the current to zero. The current direction is indicated by the black arrow and the geometrical center of the disk is marked with a black dot.

The vortex core displacement is carefully examined using a series of current densities for the two current directions, e.g. typically $j_e = 0 j_{e;0}$, $\pm j_{e;0}$, $\mp 2 j_{e;0}$ and $0 j_{e;0}$ with $j_{e;0} = 2.7 \cdot 10^{11}\,\text{A/m}^2$ for Py, to exclude the influence of magnetic pinning sites and local inhomogeneities which have been shown to affect the vortex core position and thus the estimated non-adiabaticity [204, 228]. To reduce the influence of sample drift on the measured data multiple short images ($\sim 30 - 40\,\text{s}$ each) are taken of each magnetic state with a combined pixel dwell time of $10 - 50\,\text{ms}$ and a spatial resolution of $20 - 30\,\text{nm/Pixel}$. Using a coordinate system established through the disk and contact structure, see equation 7.3.3, a linear regression is performed on robust trajectories to extract the slope (see Fig. 5.8 (b)) and identify the coefficients in equation 5.1.3.

A collection of the considered vortex core positions can be found in Figs. 5.8 (a), (c) and (d) indicating four distinct displacement directions for $PyDy(0.00\,\text{at.\%})$ and $PyDy(1.49\,\text{at.\%})$. Due to a smaller number of available samples size and a higher fraction of discarded states due to increased pinning, the directionality of the displacement is less clear in (d). From the measured sample sets, we estimated that $76 \pm 4\%$ ($PyDy(0.00\,\text{at.\%})$), $72 \pm 8\%$ ($PyDy(1.49\,\text{at.\%})$) and $64 \pm 14\%$ ($PyDy(1.96\,\text{at.\%})$) of the vortex core positions are not dominated by pinning sites and show consistent behavior suitable for reliable extraction of ξ.
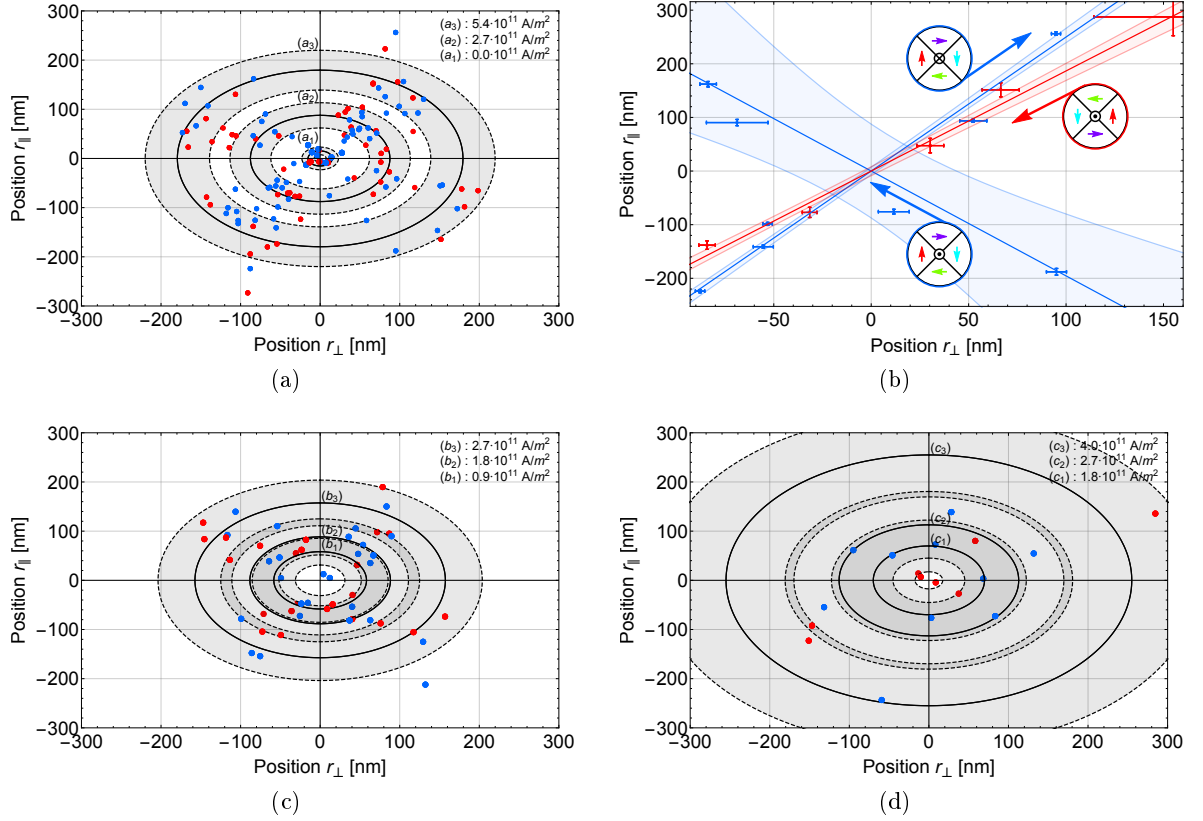
Figure 5.8: (a), (c) and (d) show the collected vortex core positions for various disk structures and applied charge currents relative to the zero current position. The corresponding film thicknesses are (a) 27 nm (undoped Permalloy), (c) 26 nm ($PyDy(1.49\,\mathrm{at.\%})$) and (d) 26 nm ($PyDy(1.96\,\mathrm{at.\%})$). Magnetic states dominated by pinning sites have been removed from the plots. The color differentiates between the two vortex state chiralities $c = +1$ (red) and $c = -1$ (blue). The superimposed solid circles indicate the mean magnitude of displacement for a given current density with the shaded region being the associated 1σ-area. (b) shows the current-induced vortex core displacement of three distinct vortex states in a specific undoped Permalloy disk described by equation 5.1.3. The polarity of a vortex state can be inferred by the perpendicular component of the slope, $\partial r_\perp / \partial j \propto p$. The opening angle between the displacement direction of two magnetic states with opposing chirality and polarity is related to the non-adiabatic coefficient, ξ.

5.5 Discussion

First, we restrict considerations to undoped samples that show four distinct displacement directions which exhibit statistically significant correlations with the state chirality as predicted by equation 5.1.3 (see Fig. 5.8 (a)). As shown in Fig. 5.8 (b), we varied the current density for distinct magnetic states in each sample before determining the weighted-average slopes for the two chiralities and extracted the corresponding non-adiabaticity by employing equation 5.1.5. Here, we conclude a weighted-average value of $\xi = 0.067 \pm 0.015 = (11.0 \pm 2.5)\alpha$. As mentioned before, a wide range of ξ values have been reported for undoped Permalloy which show a dependance on the magnetic state and thus we restrict our comparison to other systems considering vortex cores (see table 5.1).
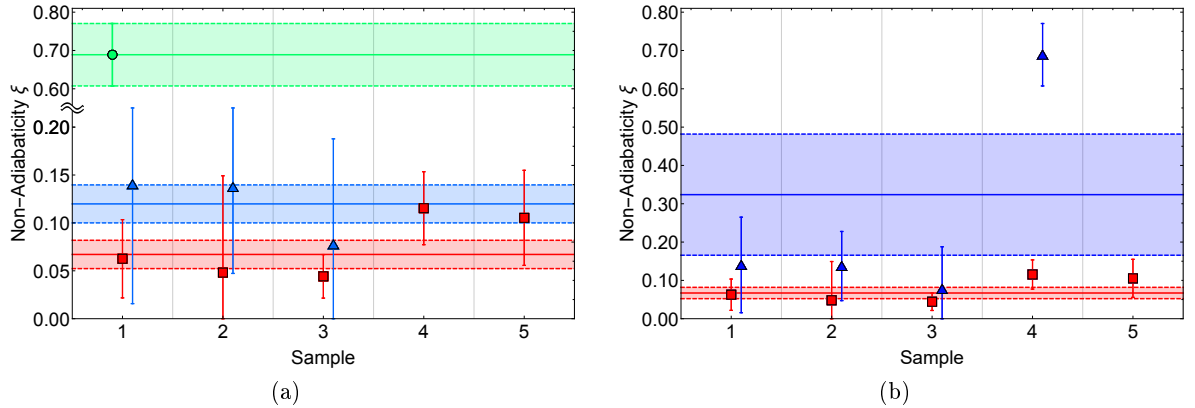
Figure 5.9: Non-adiabatic coefficient, ξ, derived from the observed vortex core displacement in individual samples with Dysprosium dopant concentrations of $0.00\,\mathrm{at.\%}$ (red squares), $1.49\,\mathrm{at.\%}$ (blue triangles) and $1.96\,\mathrm{at.\%}$ (green dots). (a) shows the mean non-adiabatic coefficient derived for each Dy doping level as indicated by the solid lines. For (b), the derived ξ-values of doped samples are treated as a single sample set with a mean dopant concentration of $1.73\,\mathrm{at.\%}$.

For these systems, the reported ξ values still range from 0.061 to 0.15, with our value comparable to previous results based on the same measurement scheme [203–205] and with vortex core precession orbit measurements [201, 205]; in particular, the ξ-α ratios are identical within error and it is consistently observed that $\xi > \alpha$. For our case, the ratio is determined to be $\langle\xi\rangle/\alpha = 11.0 \pm 2.5$ which is comparable to values from literature with similar measurements.

Nevertheless, these results deviate from ξ values determined using schemes which rely on spin wave excitations or on other spin structures and thus probe different length scales in magnetic systems (see section 5.2). Next, we consider the influence of the rare-earth doping on the magnetic properties of the system using the same methodology as before. For the lower doped samples we can extract three values of ξ, whereas due to the increased pinning only a single sample showed robust behaviour in the highly-doped case. We separately determined weighted-mean values of ξ as 0.119 ± 0.02 and 0.69 ± 0.08 for a Dy content of $1.49\,\mathrm{at.\%}$ and $1.96\,\mathrm{at.\%}$, respectively. However, due to a thermally activated redistribution [229] of the mobile rare earth element within the host material which causes a higher Dy concentration at the sample surface and a considerable amount in the Au capping layer as suggested by RBS we expect a similar behaviour for the two dopant concentrations. Additionally, the FMR measurements showed similar values for these two sample sets. Thus, this lends itself to the conclusion that the averaged non-adiabaticity, damping parameter and dopant concentration of these two sample sets can be considered as robust parameters, i.e. $\xi = 0.32 \pm 0.16$, $\alpha = 0.0398 \pm 0.0012$ and $1.73\,\mathrm{at.\%}$, respectively. The general trend from both methods of analysis indicate that ξ increases with α (see table 5.2). Furthermore, the combined data from the averaged sample is consistent with a common scaling constant of ξ and α which is in good agreement with previous studies using Ho-doped Permalloy [199].

	Py	$PyDy$	$PyDy$	$PyDy$
	(0.00 at.%)	(1.49 at.%)	(1.96 at.%)	(1.73 at.%)
M_S [kA/m]	878.4 ± 0.3	791.2 ± 0.3	659.4 ± 0.2	713 ± 33
ΔH_0 [Oe]	0.4 ± 0.1	n.a.	n.a.	n.a.
ΔH [Oe] at 4.5 GHz	0.2 ± 0.01	1.24 ± 0.15	1.32 ± 0.15	1.28 ± 0.04
$10^2 \alpha$ at 293 K	0.61 ± 0.01	3.9 ± 0.5	4.1 ± 0.5	3.98 ± 0.12
$10^2 \xi$ (Sample 1)	6 ± 4	14 ± 12	69 ± 8	14 ± 12
$10^2 \xi$ (Sample 2)	5 ± 10	13 ± 9	n.a.	13 ± 9
$10^2 \xi$ (Sample 3)	4 ± 2	8 ± 11	n.a.	8 ± 11
$10^2 \xi$ (Sample 4)	12 ± 4	n.a.	n.a.	69 ± 8
$10^2 \xi$ (Sample 5)	11 ± 5	n.a.	n.a.	n.a.
$10^2 \langle \xi \rangle$	6.7 ± 1.5	11.9 ± 2	69 ± 8	32 ± 16
$10^2 \alpha$ at 293 K	0.61 ± 0.1	3.9 ± 0.5	4.1 ± 0.5	3.98 ± 0.12
$\langle \xi \rangle / \alpha$	11.0 ± 2.5	3.1 ± 0.6	16.8 ± 2.8	8.1 ± 4

Table 5.2: Summary of experimentally determined coefficients derived in FMR and current-induced vortex core displacement measurements. The sample number refers to a sample within a sample batch, e.g. "Sample 1" exists for each dopant concentration. The last column lists the properties of the "virtual" sample batch derived from the two sample batches with finite Dy dopant concentration.

Hence, we observe a strong increase of the non-adiabaticity and the damping parameter at 1.73 at.% dysprosium content and a ξ-α ratio which is within the error identical to the undoped system; therefore indicating a similar scaling of α and ξ with the dopant at low concentrations.

In spite of α being only weakly temperature dependent for the undoped Permalloy film [230] the doped films are expected to exhibit enhanced damping at low temperatures [16]. A previous study on transverse domain wall depinning deduced that ξ exhibits only a weak temperature dependance between 80 K and 340 K for undoped Permalloy [231]. Here, we use a low sample base temperature of ≈ 24 K; however, due to resistive heating an increase in temperature of $\approx 75 - 150$ K is present which is estimated from the measured increase in resistance and thus ξ is determined at $T > 24$ K. Nevertheless, we expect the non-homogeneous heating to be mainly localised in the vicinity of the interface regions between the contact pads and the disk structure [232, 233], so not at the vortex core position. However, the reported ξ/α is significantly higher compared to schemes based on the hysteretic behaviour or on spin wave measurements [190, 192] which offer notably different spin configurations, thus highlighting the importance of the involved magnetic state and supporting a ξ value modified in the vicinity of features with high magnetization gradients such as the vortex core [206].

5.6 Conclusion

We separated the non-adiabatic spin torque contribution using the current-induced vortex core displacement and derived the non-adiabatic coefficient, ξ, for undoped and Dy-doped Permalloy, respectively. The undoped host material exhibited an α value and a ξ-α ratio in accordance with previous measurements relying on the identical scheme [204, 205], albeit deviating from results obtained using other measurement schemes which showed smaller ξ-α ratios for systems lacking high magnetization gradients.

Furthermore, for both intentional dopant levels, we observed a non-adiabaticity significantly larger than the corresponding damping parameter; however the ratio stayed constant within errors which indicates a similar scaling with the dopant and thus suggesting a common mechanism underlying α and the determined ξ contribution. Nevertheless, the dopant induced a change in the saturation magnetization for low concentrations and an additional change in the magnetic anisotropy at a concentration of $\approx 8\,\mathrm{at.\%}$. At higher concentrations, an unequal scaling of α and ξ could be possible as previously observed for Ho [199] and combined with an increased drift velocity, $\mu_B P j_e / e M_S$, at a fixed spin current density, $P j_e$, could enable high domain wall velocities as required for future devices.

CHAPTER 6

Summary and Outlook

In this thesis, the feasibility of two key requirements of proposed spin polarized current-driven domain wall motion-based spintronic devices was investigated. The study employed a micromagnetic model based on the Landau-Lifshitz-Gilbert equation to predict possible magnetic states and their response to external driving stimuli. This was then experimentally tested and investigated via high resolution imaging using SEMPA.

First, we investigated the influence of the structure geometry on the prevalence of transverse and vortex domain wall structures for macroscopic iron rings at different widths and thicknesses in a combined experimental and theoretical study. The simulated domain wall type distribution was systematically evaluated by considering the interplay between magnetostatic and exchange energy in addition to the Zeeman energy contribution present during the domain wall nucleation process as present in the experiment. Here, the previously frequently observed symmetric transverse and vortex domain walls are accompanied by an asymmetric transverse domain wall phase. An evaluation of the simulated asymmetric transverse domain wall states suggests that the asymmetry of the domain walls increases with increasing ring width and ring thickness and thus can be set by selecting appropriate geometries. We determined the corresponding experimentally realized domain wall state distribution at finite temperatures by employing high resolution SEMPA imaging and compared it to the $0\,\mathrm{K}$ simulated phase diagram. The experimental data showed a transition from the transverse to the vortex domain wall phase far above the analytically derived transition for the state which globally minimizes the energy. Furthermore, only the narrowest thin structures showed purely symmetric transverse walls while a substantial range of widths and thicknesses exhibited both symmetric and asymmetric transverse walls. For structures with a particularly strong edge roughness, vortex domain walls occurred deep within the transverse domain wall phase, thus, highlighting the importance of nucleation sites and locally varying magnetic properties in real systems. In particular, the influence of defects was found to be more crucial than in the previously studied Py and Co systems. We conclude that for application-related systems, the complex interplay between the geometry, surface condition and materials properties has to be carefully balanced to achieve a reliable formation of specific domain wall types, e.g. symmetric transverse domain walls. However, the simple growth behaviour of iron combined with its relatively high spin polarization and low magnetocrystalline anisotropy compared to Co adds interesting and potentially advantageous characteristics to the broad range of material properties available for spintronics while benefiting certain device geometries.

Secondly, we addressed the spin transfer torque effect generated by a spin polarized current acting on a magnetic vortex state with a well-defined core region giving rise to a localized spin torque. Specifically, by observing the vortex core displacement, we derived the coupling strength, ξ, of the non-adiabatic spin torque for the nickel-iron alloy, Permalloy. The measurement was performed on multiple disk structures each exhibiting up to four energetically-degenerate vortex states (different polarity and/or chirality). Vortex core positions were determined for different current densities of up to $\sim 5 \cdot 10^{11}\,\mathrm{A/m^2}$ to restrict considerations to structures with a sufficiently low pinning density and strength. For Permalloy a non-adiabaticity of 0.067 ± 0.015 was derived which agrees with previously published values derived for similar systems. In addition to that, the ratio of the Gilbert damping parameter, α, and ξ was identical within error with these published values and evaluated to 11.0 ± 2.5. Furthermore, we examined the non-adiabaticity while changing α by rare earth doping using Dy. The measurements suggest an increase of ξ with α; however, within the studied dopant concentration range the ξ-α ratio remained constant and thus an unchanged spin torque efficiency is suggested. Nevertheless, we observed

a reduction of the saturation magnetization with the Dy concentration which combined with a constant ξ-α ratio potentially enables high performance spintronic devices with fast domain wall velocities.

Overall, the thesis contributed to the ongoing investigation of the formation and control of magnetic states and it is to be expected that a combination of the described properties enables favourable performance and energy efficiency characteristics as required for new spintronic devices. Despite that, many aspects are left to be thoroughly examined and further disentanglement of contributing factors is necessary.

As an example, within this work the quasi-static domain wall formation was investigated for ring structures which support three different domain wall types and the importance of the local structure was highlighted. However, in an additional future investigation, the stability of the phase diagram under the influence of external forces and potential transformations between the observed domain wall structures would be of interest. Furthermore, different approaches for an induced domain wall transformation are available either utilizing more conventional Oersted-fields and spin transfer torques or alternatively, the newly studied spin orbit torque effects. Information about the corresponding energy potential can be acquired by systematically varying the external magnetic field direction for each nucleation event. The angular dependance of the domain wall type prevalence enables a mapping of the potential landscape. The energy barrier between metastable magnetization configurations is expected to be overcome at elevated temperatures. Thus, by introducing thermal energy into the system and measuring the transition probability between states, an estimate of the energy barrier height can be obtained which has significant importance for domain wall-based technologies such as non-volatile memory devices or magnetic field direction sensors. This could be complemented by finite temperature simulations, which themselves are an active field of research and challenging to perform rigorously. Furthermore, for this work the decision was made to change the ring thickness and width while keeping the outer diameter constant. Alternatively, at a constant width the domain wall stability at different mean curvatures becomes increasingly important, e.g. for meandering fixed-width nanowires and in particular in systems with artificially tailored edge roughness to mitigate the Walker breakdown.

We determined the non-adiabatic spin torque and the Gilbert damping parameter for three Dy dopant concentrations; however, a comprehensive study requires more dopant concentrations and a higher statistics for the determined parameters. The analysis can be complemented by replacing Dy with other rare earth elements like Tb for which a similar increase in α was reported or another rare earth element, e.g. Gd, with a claimed negligible influence on α. Furthermore, modifications have recently made to extend our system's capabilities to provide fast data acquisition with a nanosecond time resolution and allow for the synchronization with an external source and thus enable an additional measurement scheme. For instance, a time-resolution better than $50\,\text{ns}$ can be exploited to gauge the pinning site density and strength. Here, a (slow) linear current ramp causes a linear increase in the spin transfer torque strength and moves the vortex core quasi-instantaneously to an equilibrium position. By measuring the trajectory and its deviation from a straight line, information about the pinning site density and strength can be inferred while the linear contribution has a close connection to the non-adiabaticity. Alternatively, a rectangular current pulse with a fast rise time enables an advanced scheme for the determination of the vortex core gyration and subsequent relaxation towards the equilibrium position. Provided that the time-resolution is significantly higher than the relaxation rate, the observed trajectory can be used to extract α for each individual structure while not relying

on a FMR measurement of an accompanying thin film. Furthermore, employing the high spatial and time resolution allows for detailed studies of the domain wall depinning behaviour and the complex dynamics during current-induced transformations, e.g. beyond the Walker breakdown, while the present system is limited to the observation of the initial and final state and thus provides only mean domain wall velocities.

Another active research area in spintronics targets the decoupling of the charge current and the spin current. A generated pure spin current acts on the magnetic state without adding a thermal load at the position where the magnetization is changing which is usually present in systems with charge current-induced magnetization modification. For instance, this can be achieved in a layered structure with a current carrying component on the bottom and a ferromagnetic material on top, e.g. in a charge current carrying heavy metal such as Pt the spin Hall effect causes a spin current perpendicular to the generating current. Further interactions can be used to generate spin currents such as the Dresselhaus and the Rashba spin orbit coupling. Alternatively, by employing a non-local spin valve layout the spin current generation and the magnetic system can be spatially separated further with a non-magnetic spin conduit, e.g. Cu, in between. For such systems a lock-in scheme of the modified SEMPA could enable the imaging of the periodic magnetization modification and the potential spin accumulation on the surface of the heavy metal.

From these examples it can be seen that the upgraded SEMPA system opens up a large range of new measurements, retaining existing SEMPA attributes such as a high surface sensitivity of $\sim 1\,\text{nm}$ and a high lateral resolution, and extends them to short time scales, enabling a new class of SEMPA measurements.

CHAPTER 7

Appendix

7.1 Normalization of Measured Asymmetry

Secondary electrons are collected by a spin polarized low energy electron diffraction (SPLEED) detector and the number of diffracted electrons for each of the four main diffraction spots are determined with Channeltron detectors. For non-magnetic samples the measured average count rates for the Channeltron detectors should be identical, however, due to detector sensitivity asymmetries discrepancies can be observed. Contributing factors to the discrepancies are slight misalignments of the Channeltron detectors, the tungsten single crystal and the sample position relative to the SPLEED detector. Beside a geometrical misalignment, unequal electron detection efficiencies of opposing Channeltron detectors and internal deflection voltages of the SPLEED detector change the relative count rates, consequently changing the perceived normalized magnetization of the samples. Neglecting, typical measurement effects such as averaging of the magnetic moments close to the electron beam, e.g. the contribution of secondary electron generated by the back-scattered electron beam and reflection close to the lateral sample edge, and assuming a single magnetic material throughout the sample, the measured asymmetry, A_{Meas}, for each position is located on a circle centered around zero with a common radius. However, typically A_{Meas} fullfills neither of the two conditions and is located on an off-center ellipse (see Fig. 7.1). Multiple measures are available to determine the "best" fitting ellipse [234] to the asymmetry distribution, however, we will restrict considerations to schemes based on the minimal Euclidean distance of a point to the ellipse and the algebraic distance. For noiseless distributions, i.e. the measured asymmetry lies on an ellipse, the two schemes render identical ellipses, but in the presence of noise the output differs [235, 236]. For a single point, $\boldsymbol{A} = (A_1, A_2)^\top$, the Euclidean distance, D_E, and the algebraic distance, D_A, to an ellipse are defined as follows:

$$D_E(\boldsymbol{A}) = \min_{\theta \in [0, 2\pi)} \left\| \begin{pmatrix} \cos\tau & -\sin\tau \\ \sin\tau & \cos\tau \end{pmatrix} \begin{pmatrix} A_{r_1}\cos\theta \\ A_{r_2}\sin\theta \end{pmatrix} + \boldsymbol{A}_0 - \boldsymbol{A} \right\|^2 \tag{7.1.1}$$

$$D_A(\boldsymbol{A}) = \boldsymbol{A}^\top \begin{pmatrix} \lambda_1 & \lambda_2 \\ 0 & \lambda_3 \end{pmatrix} \boldsymbol{A} + (\lambda_4, \lambda_5)\boldsymbol{A} + \lambda_6 \tag{7.1.2}$$

The Euclidean distance relies on the parametric representation of an ellipse and provides a convenient way to determine the center, $\boldsymbol{A}_0$, the axis A_{r_1}, A_{r_2} and the tilting, τ. Be that as it may, computationally, this approach is unfeasible for a large data set [235, 236]. The algebraic distance hides $\boldsymbol{A}_0$, A_{r_1}, A_{r_2} and τ in its coefficients,

$$\lambda_1 = A_{r_1}^2 \sin^2\theta + A_{r_2}^2 \cos^2\theta$$
$$\lambda_2 = 2(A_{r_2}^2 - A_{r_1}^2)\sin\theta\cos\theta$$
$$\lambda_3 = A_{r_1}^2 \cos^2\theta + A_{r_2}^2 \sin^2\theta$$
$$\lambda_4 = -2\lambda_1 A_{0\,1} - \lambda_2 A_{0\,2}$$
$$\lambda_5 = -\lambda_2 A_{0\,1} - 2\lambda_3 A_{0\,2}$$
$$\lambda_6 = \lambda_1 A_{0\,1}^2 + \lambda_2 A_{0\,1} A_{0\,2} + \lambda_3 A_{0\,2}^2 - A_{r_1}^2 A_{r_2}^2,$$

but inverse transformations for the coefficients are available [235]. Although, the algebraic distance (see equation 7.1.1) describes additional geometric shapes, $\lambda_2^2 - 4\lambda_1\lambda_3 < 0$ restricts it to ellipses [236]. Under this restriction, we minimize the mean distance,

$$\chi^2[\{\boldsymbol{A}_i\}_{i \in \{1,...,N\}}] \equiv \sum_{i=1,...,N} \sigma_i^{-2} D_A^2(\boldsymbol{A}_i), \tag{7.1.3}$$

for a given data set, $\{\boldsymbol{A}_i\}_{i\in\{1,\dots,N\}}$, using a numerically stable non-iterative algorithm for constant weights[1], $\sigma_i = \sigma$ [237]. Using the proposed algorithm on measured asymmetry data, $\{A_i\}_{i=1,\dots,N}$, a noise-level dependent overestimation of the minor and major axes can be observed, causing a reduction of the mean corrected magnitude (see Fig. 7.2). For magnetic structures with an isotropic asymmetry distribution, e.g. a vortex state, a simple multiplication can be performed setting the mean asymmetry magnitude to one. For less isotropic distributions a simple correction is usually not feasible and computationally more expensive algorithms have to be used. The following data analysis rests upon an error estimate [238] of λ_k,

$$\frac{\partial^2 \chi^2 [\{\boldsymbol{A}_i\}_{i\in\{1,\dots,N\}}]}{\partial \lambda_k \partial \lambda_k} \equiv \sum_{i=1,\dots,N} \sigma^{-2} a_{k\,i} a_{k\,i} \equiv \sigma_{\lambda_k}^{-2},$$

with

$$\sigma^2 \equiv \frac{1}{N-5} \sum_{i=1,\dots,N} \left(\sum_{j=1,\dots,5} a_{i\,j} \lambda_j - 1 \right)^2$$

and

$$\boldsymbol{a}_j \equiv (A_{1\,j}^2, A_{1\,j} A_{2\,j}, A_{2\,j}^2, A_{1\,j}, A_{2\,j}).$$

The standard deviations, σ_{λ_k} are subsequently inserted into the derivatives of the inverse transformations to acquire $\delta \boldsymbol{A}_0$, δA_{r_1}, δA_{r_2} and τ to estimate the influence on the vortex-core position.

---

[1]Alternatives have been proposed to decrease the mean Euclidean distance between algebraic and Euclidean best-fit ellipses, iterative-algebraic algorithms based on a non-constant weighted mean to balance computational expense and the mean Euclidean distance of the data set to the fitted ellipse [235].
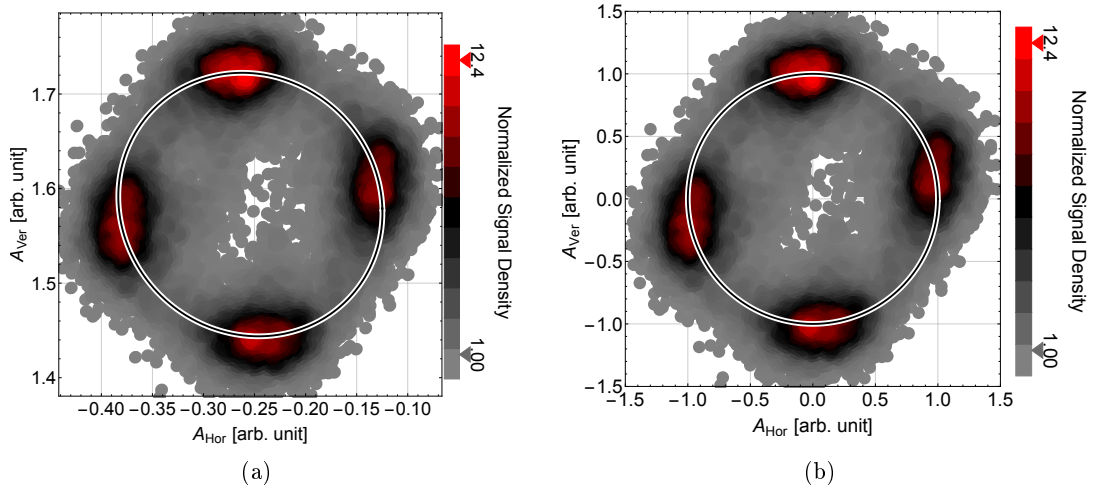
(a)   (b)

Figure 7.1: (a) Measured asymmetry distribution of a Landau-state in a 24 nm thick Permalloy square with a lateral dimension of $4.3\,\mu$m. The plot shows the ellipse which minimizes the average conic distance of the data points to the ellipse. The center of the ellipse with a minor axis of 0.13 and an eccentricity of 0.42 is at $\boldsymbol{A}_0 = (-0.25,\ 1.58)^\top$. (b) shows the asymmetry after applying a correction according to equation 7.1.1.
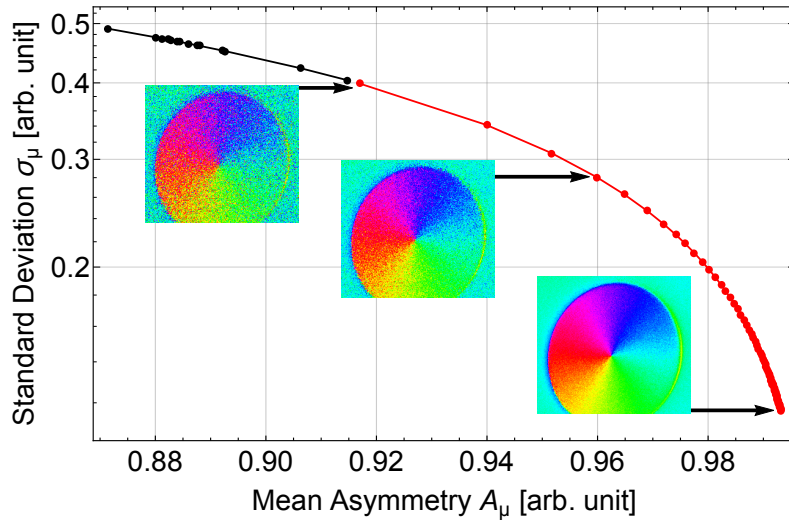

Figure 7.2: The general trend of the mean asymmetry magnitude, A_μ, is indicated by the black curve. It is derived from multiple magnetic vortex states in different sized 23 nm thick Permalloy disks with distinct noise-level, σ_μ, after various argon ion millings to remove a gold capping layer. The measurement times average to $\sim 30\,$min for each black data point. The red curve shows the trend of a specific vortex state with a low noise level after 19 min of milling and data points equally spaced in measurement time. Here, the inset depicts the state after different measurement times. The general trend (not shown above $A_\mu = 0.92$) agrees with the red curve down to the lowest measured noise-level.
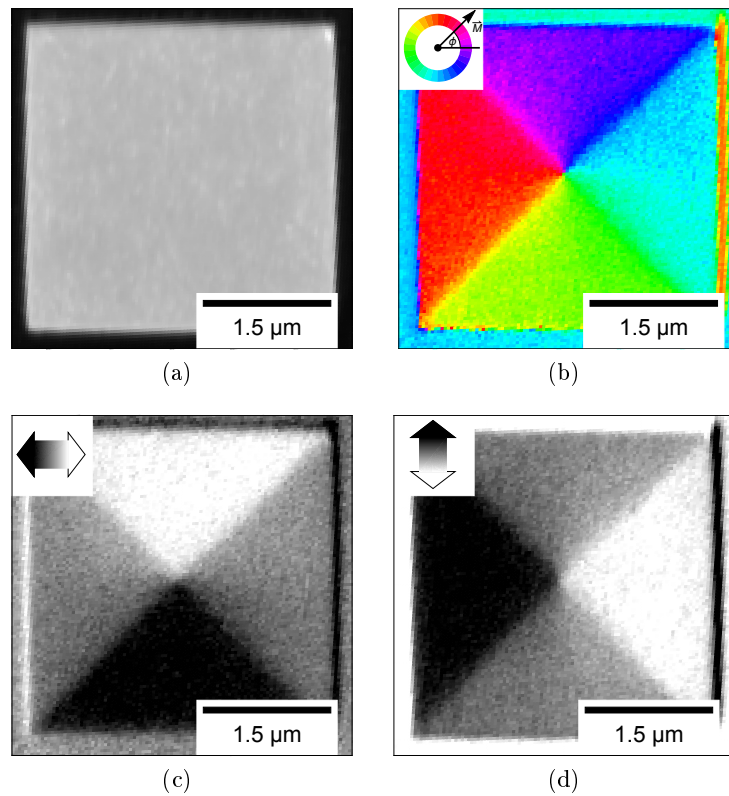
(a)   (b)

(c)   (d)

Figure 7.3: (a) SEM image of a 24 nm thick Permalloy square with lateral dimensions of 4.3 μm. The corrected measured asymmetry for the horizontal and vertical component is depicted in (c) & (d). (b) shows the color-coded asymmetry revealing a magnetic flux-closed Landau-state with a clock-wise rotation direction. Close to the sample edges a shift in magnetic contrast is observed which is attributed to electron escape angle induced skewed asymmetry [81] and limits the observable characteristic length scale of structured samples.

7.2 Feature-Detection in Images

The measured counts of the four Channeltron detectors are provided in matrices and combined into corrected in-plane asymmetries as outlined in section 7.1. In this section, we will discuss how a reliable feature-detection for noisy data is achieved by introducing a few conventions. Consider a simple vector space $A \subseteq \mathbb{R}^2$ and two vector fields $\boldsymbol{v_1}$ and $\boldsymbol{v_2}$ defined on A. Using the inner product $\langle ., . \rangle \to \mathbb{R}$ we define a scalar product on A:

$$\{\boldsymbol{v}_1, \boldsymbol{v}_2\}_A \equiv \left(\int_A \mathrm{d}A \right)^{-1} \int_A \langle \boldsymbol{v}_1 (\boldsymbol{r}), \boldsymbol{v}_2 (\boldsymbol{r}) \rangle \, \mathrm{d}A \qquad (7.2.1)$$

The scalar product exhibits the following properties:

$$\{\boldsymbol{v}_1, \boldsymbol{v}_2\}_A = \{\boldsymbol{v}_2, \boldsymbol{v}_1\}_A$$
$$\{\boldsymbol{v}_1, \lambda\boldsymbol{v}_2\}_A = \lambda\{\boldsymbol{v}_1, \boldsymbol{v}_2\}_A \qquad\qquad \forall \lambda \in \mathbb{R}$$
$$\{\boldsymbol{v}_1, M\boldsymbol{v}_2\}_A = \{\boldsymbol{v}_2, M^\top\boldsymbol{v}_1\}_A \qquad\qquad \forall M \in \mathbb{R}^{2x2}$$
$$\{\boldsymbol{v}_1, \boldsymbol{v}_2 + \boldsymbol{v}_3\}_A = \{\boldsymbol{v}_1, \boldsymbol{v}_2\}_A + \{\boldsymbol{v}_1, \boldsymbol{v}_3\}_A$$

Based on this scalar product we define a cross-correlation function,

$$S_A [\boldsymbol{v}_1, \boldsymbol{v}_2] \equiv 1 - \frac{1}{4}\{\boldsymbol{v}_1 - \boldsymbol{v}_2, \boldsymbol{v}_1 - \boldsymbol{v}_2\}_A,$$

which rates the similarity of the two vector fields $\boldsymbol{v}_1$ and $\boldsymbol{v}_2$. We restrict our considerations to fields which fulfill $\langle \boldsymbol{v}(r), \boldsymbol{v}(r) \rangle = 1 \; \forall \boldsymbol{r} \in \mathbb{R}^{2x2}$ and conclude that for such vector fields $S_A [\boldsymbol{v}_1, \boldsymbol{v}_2]$ is within $[0; 1]$. The measured data of a vortex state displaced by $\boldsymbol{R_0}$ can be approximated with an analytical description [239], $\boldsymbol{v}(\boldsymbol{r} - \boldsymbol{R}_0)$, combined with a zero-mean noise term, $\boldsymbol{n}(\boldsymbol{r})$. The proposed analytical solution for a displaced vortex core incorporates finite size effects which cause deformations of the magnetic state as the vortex core approaches the disk boundary. However, our measurements did not show a large displacement-disk diameter ratio for experimentally suitable current densities and a comparison of the measured vector field with a rigid analytical solution, $\boldsymbol{v}(\boldsymbol{r} - \boldsymbol{R})$ which has the vortex core at position $\boldsymbol{R}$ seems adequate:

$$
\begin{aligned}
S_A [\boldsymbol{v}_{Measured}, \boldsymbol{v}_{Reference}] =& S_A [\boldsymbol{v}_{R_0} + \boldsymbol{n}, \boldsymbol{v}_R] \\
=& 1 - \frac{1}{4}\{\boldsymbol{v}_{R_0} + \boldsymbol{n} - \boldsymbol{v}, \boldsymbol{v}_{R_0} + \boldsymbol{n} - \boldsymbol{v}_R\}_A \\
=& 1 - \frac{1}{4}\{\boldsymbol{v}_{R_0} - \boldsymbol{v}_R, \boldsymbol{v}_{R_0} - \boldsymbol{v}_R\}_A \\
& - \frac{1}{2}\{\boldsymbol{v}_{R_0} - \boldsymbol{v}_R, \boldsymbol{n}\}_A - \frac{1}{4}\{\boldsymbol{n}, \boldsymbol{n}\}_A \\
=& S_A [\boldsymbol{v}_{R_0}, \boldsymbol{v}_R] - \underbrace{\frac{1}{2}\{\boldsymbol{v}_{R_0} - \boldsymbol{v}_R, \boldsymbol{n}\}_A}_{\approx 0} - \frac{1}{4}\{\boldsymbol{n}, \boldsymbol{n}\}_A \qquad (7.2.2)
\end{aligned}
$$

For slowly varying vector fields the second term in equation 7.2.2 has a limited influence on S_A and vanishes exactly if $\boldsymbol{R_0} = \boldsymbol{R}$, but the maximum value of S_A as a function of $\boldsymbol{R}$ is shifted relative to the noiseless case. The approximate maximum value of S_A is determined by noise characteristics and depends on the noise source. By noting that a large fraction of fluctuations in the number of counts, typically $10^4 - 10^5$, can be attributed to shot noise and that each vector field component is derived by subtracting counts of two opposing
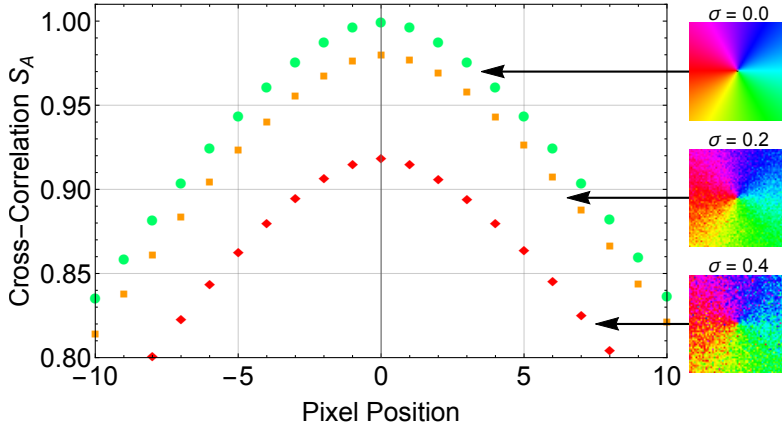
Figure 7.4: The cross-correlation, S_A, evaluated for discrete positions on a 30×30 mesh relative to the exact vortex core position for a standard deviation of $\sigma = 0.0$ (green dots), $\sigma = 0.2$ (orange squares) and $\sigma = 0.4$ (red diamonds). The inset shows the corresponding magnetic states for the different standard deviations. For each set, the maximum value of the cross-correlation is lowered by $\sigma^2/2$ while affecting the position of the interpolated maximum only negligibly (notice the slight tilting of the $\sigma = 0.4$ curve).

Channeltron detectors, the noise term of the measured asymmetry can be approximated by a zero-mean Gaussian noise with a standard deviation of σ:

$$\{\boldsymbol{n}, \boldsymbol{n}\}_A \approx 2\sigma^2$$

Provided that the second term in equation 7.2.2 is sufficiently suppressed, the selected measure, S_A, provides a robust scheme to determine the vortex core position in highly noisy data by comparing the measured asymmetry, $\boldsymbol{v}_{Measured} = \boldsymbol{A}$, with a reference vector field, $\boldsymbol{v}_{Reference}$. Our SEMPA setup provides pixel-based asymmetry data with a spatial resolution of $\sim 20 - 30\,\mathrm{nm/pixel}$ and, hence, the measure, S_A, is evaluated on discrete positions (see Fig. 7.4). A polynomial interpolation of order three is used to achieve a sub-pixel precision in locating $S_{A;max}$. Applying the proposed scheme to a detached $23\,\mathrm{nm}$ thick Permalloy disk, we extract the corrected in-plane asymmetry in a $55 \times 56\,\mathrm{pixel}$ large area around the expected vortex core and determine S_A for different displacements, $\boldsymbol{R}$, of the analytical reference structure. Relative to the center of the extracted area, S_A has an absolute maximum of 0.97 at $\boldsymbol{R} \approx (1.53, -3.86)\,\mathrm{pixels}$ which corresponds to a vortex core position of $(161.0, 43.1)\,\mathrm{nm}$ relative to the center of the disk (see Fig. 7.5).
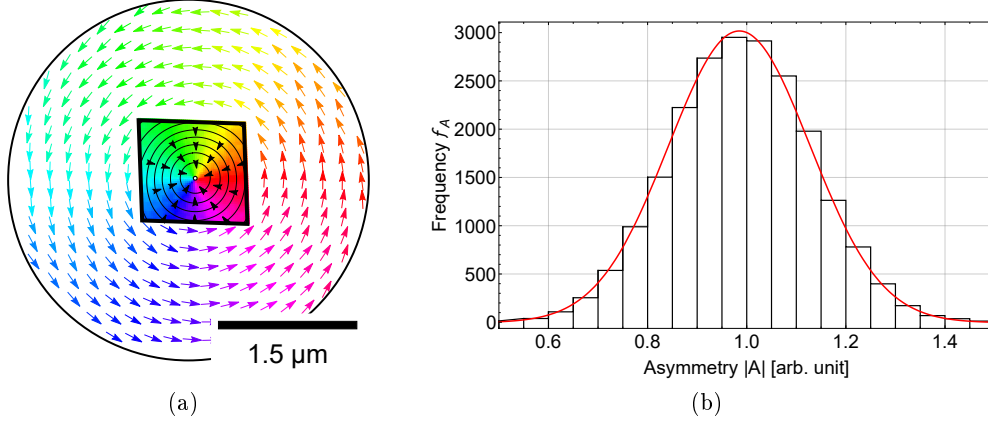
(a)   (b)

Figure 7.5: (a) Schematic derived from an asymmetry corrected vortex state in a $23\,\mathrm{nm}$ thick Permalloy disk. The colored arrows indicate the measured magnetization direction. The framed inner part shows the color-coded magnetization direction used for the vortex core position determination. Equipotential lines for S_A and the associated gradient field indicate the position of maximum congruence (white dot), understood as the vortex core position. Using $S_{A;max}$, our estimate for the standard deviation is $\sigma \approx 0.155$ whereas the corrected asymmetry distribution (see (b)) yields $\sigma_\mu \approx 0.143$ with a mean value of $A_\mu \approx 0.97$ indicating an imperfectly normalized distribution (see Fig. 7.2). However, we estimate the increase in σ due to a reduced A_μ to be ≈ 0.002 and account the observed difference to an uncompensated analytical reference structure, i.e. the reference structure does not equal the measured magnetic state. Further analysis reveals a strong reduction of the in-plane asymmetry in a region $\approx 200\,\mathrm{nm}$ around the vortex core (see Fig. 3.4) as expected [240].

7.3   Error-Estimate for the Vortex Core Position

SEMPA does not provide normalized asymmetries and a correction as described in section 7.1 has to be applied to the uncorrected $\boldsymbol{A}_{uncorr}$ to set the average norm of the asymmetry to $\langle \|\boldsymbol{A}\| \rangle = 1$. The accuracy of the correction is affected by the noise level and the magnetic state in question. The corrected asymmetry can be written as $A(\boldsymbol{r}) \equiv T_A(v(\boldsymbol{r} + \delta \boldsymbol{R}) - \boldsymbol{v}_0)$ with $\delta \boldsymbol{R}$ being the apparent displacement of the vortex core position due to noise. Furthermore, the position, $\boldsymbol{r}$, and $\delta \boldsymbol{R}$ are in the coordinate system provided by the measurement, i.e. the coordinate system of the distorted disk, and transformation to the undistorted geometry is applied subsequently. The known uncertainties in T_A and $\boldsymbol{v}_0$ can be translated into an uncertainty of the vortex core position as outlined below:

$$
\begin{aligned}
S_A[\boldsymbol{A}, \boldsymbol{v}] &= 1 - \frac{1}{4}\{\boldsymbol{A} - \boldsymbol{v}, \boldsymbol{A} - \boldsymbol{v}\}_A \\
&= 1 - \frac{1}{4}\{T(v_{\delta \boldsymbol{R}} - \boldsymbol{v}_0) - \boldsymbol{v}, T_A(v_{\delta \boldsymbol{R}} - \boldsymbol{v}_0) - \boldsymbol{v}\}_A \\
&= 1 - \frac{1}{4}\{T_A v_{\delta \boldsymbol{R}} - \boldsymbol{v}, T_A v_{\delta \boldsymbol{R}} - \boldsymbol{v}\}_A \\
&\quad + \frac{1}{2}\{T_A v_{\delta \boldsymbol{R}} - \boldsymbol{v}, T_A \boldsymbol{v}_0\}_A - \frac{1}{4}\{T_A \boldsymbol{v}_0, T_A \boldsymbol{v}_0\}_A
\end{aligned}
$$

According to the definition, $\delta\boldsymbol{R}$ vanishes in a noiseless system and an expansion of $\boldsymbol{v}_{\delta R}$ is appropriate

$$\boldsymbol{v}(\boldsymbol{r} + \delta\boldsymbol{R}) = \boldsymbol{v}(\boldsymbol{r}) + (\delta\boldsymbol{R}\cdot\boldsymbol{\nabla})\boldsymbol{v}(\boldsymbol{r}) + \frac{1}{2}(\delta\boldsymbol{R}\cdot\boldsymbol{\nabla})(\delta\boldsymbol{R}\cdot\boldsymbol{\nabla})\boldsymbol{v}(\boldsymbol{r}) + \mathcal{O}(\delta R_i \delta R_j \delta R_k)$$

We insert the expression into S_A and arrange the terms in order of powers in δR_i

$$\begin{aligned}
S_A[\boldsymbol{A}, \boldsymbol{v}] = 1 &- \frac{1}{4}\{T_A(\boldsymbol{v} - \boldsymbol{v}_0) - \boldsymbol{v}, T_A(\boldsymbol{v} - \boldsymbol{v}_0) - \boldsymbol{v}\}_A \\
&+ \frac{1}{2}\sum_{i}^{2}\delta R_i \underbrace{\{(\mathbb{1} - T_A)\boldsymbol{v} + T_A\boldsymbol{v}_0, T\partial_i\boldsymbol{v}\}_A}_{\equiv G_i} \\
&+ \frac{1}{4}\sum_{i,j}^{2}\delta R_i \delta R_j \underbrace{(\{(\mathbb{1} - T_A)\boldsymbol{v} + T\boldsymbol{v}_0, T_A\partial_i\partial_j\boldsymbol{v}\}_A - \{T_A\partial_i\boldsymbol{v}, T_A\partial_j\boldsymbol{v}\}_A)}_{\equiv -J_{ij}} \\
&+ \mathcal{O}(\delta R_i \delta R_j \delta R_k) \\
= 1 &- \frac{1}{4}\{T_A(\boldsymbol{v} - \boldsymbol{v}_0) - \boldsymbol{v}, T_A(\boldsymbol{v} - \boldsymbol{v}_0) - \boldsymbol{v}\}_A \\
&+ \sum_{i}^{2}\delta R_i(G_i - \sum_{j}^{2}J_{ij}\delta R_j) \\
&+ \mathcal{O}(\delta R_i \delta R_j \delta R_k)
\end{aligned}$$

In the presence of noise, the extreme of the measure, S_A, at the position $\boldsymbol{R}$ is consequently shifted by $\delta\boldsymbol{R} = J^{-1}\boldsymbol{G} = (J^{-1}\boldsymbol{G})(T_A, \boldsymbol{v}_0; \boldsymbol{v}, A)$ which depends on the asymmetry correction, $\{T_A; \boldsymbol{v}_0\}$, the sub space, A, and the analytical solution, $\boldsymbol{v}$. The uncertainty estimate in the vortex core position due to an asymmetry correction can therefore be written as

$$(\Delta_A R_k)^2(T_A, \boldsymbol{v}_0) = \sum_{i,j=1}^{2}(\Delta T_{Aij}(\partial_{T_{Aij}} R_k)(T_A, \boldsymbol{v}_0))^2 \tag{7.3.1}$$

$$+ \sum_{i=1}^{2}(\Delta v_{0,i}(\partial_{v_{0,i}} R_k)(T_A, \boldsymbol{v}_0))^2. \tag{7.3.2}$$

In addition to the derived uncertainty estimate, $(\Delta_A \delta R_k)^2$, we have to consider the influence of the applied geometric transformation on our image and remember that it is based on an ellipse fit to the disk and line fits to the contact pads, which can be written as

$$T_G = O(-\theta_C)O(-\theta_D)K(r_{D1}, r_{D2})O(\theta_D) \tag{7.3.3}$$

which consists of rotation matrices, $O(\theta)$, and a scaling matrix,

$$K(r_1, r_2) = \begin{pmatrix} \frac{r_1+r_2}{2r_1} & 0 \\ 0 & \frac{r_1+r_2}{2r_2} \end{pmatrix}.$$

The values and uncertainties of θ_D, r_{Di}, $\boldsymbol{r}_D$ are derived applying an edge detection algorithm to the measured topographic data and using the method seen in section 7.1 to determine the best fitting ellipse (see Fig. 7.6(a)). The remaining inclination angle, θ_C,

is determined via line fits to the upper and lower contact pad of the disk and taking the mean value (see Fig. 7.6(b)). The geometric transformation is used to derive the vortex core position, $\boldsymbol{R}'$, in the coordinate system of the undistorted geometry relative to the center of the disk, $\boldsymbol{r}_D$, and evaluate its standard deviation assuming uncorrelated errors:

$$(\Delta \boldsymbol{R}'_k)^2 = \sum_{j=1}^{2} ((\Delta T_{Gkj}(\boldsymbol{R}_j - \boldsymbol{r}_{Dj}))^2 + (T_{Gkj}\Delta_A \boldsymbol{R}_j)^2 + (T_{Gkj}\Delta \boldsymbol{r}_{Dj})^2).$$

Additionally, we observed a systematic error of the vortex core position which we attribute to the interpolation of S_A. The systematic error is below 0.05 pixels which corresponds to an additional uncertainty of about $1.5\,\text{nm}$ in the vortex core position. However, the main contribution to the uncertainty is the noise in the measured asymmetry and is typically in the range of $10 - 30\,\text{nm}$, but can reach several hundred nanometers for relatively noisy data.

---

[1]In our analysis, we neglected the influence of the uncertainty of the geometric transformation on maximizing the cross-correlation, S_A, and the strong reduction of in-plane asymmetry within a distance of $\approx 200\,\text{nm}$ of the vortex core (see Fig. 3.4).

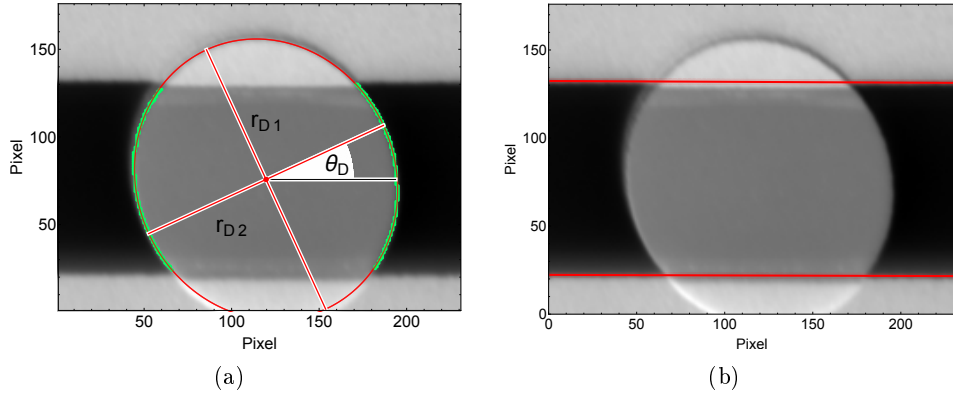(a)   (b)

Figure 7.6: (a) shows the ellipse minimizing χ^2 for edge coordinates of the distorted disk. Only edge coordinates (green dots) in-between the contact pads were taken into account ruling out possible effects due to height differences. The major and minor axes of the ellipse, r_{D1} and r_{D2}, as well well the tilting, θ_D, are indicated. (b) shows line fits to the edges of the contact pads used to determine the inclination angle, θ_C. The assumed current direction within the disk structure is perpendicular to the edges of the contact pads, defining $\boldsymbol{e}_{\parallel}$.

Bibliography

[1] W. Thomson. "On the Electro-Dynamic Qualities of Metals. –Effects of Magnetization on the Electric Conductivity of Nickel and of Iron." Proc. R. Soc. **8**, 546 – 550 (1856).

[2] M. N. Baibich, *et al.* "Giant Magnetoresistance of $(001)Fe/(001)Cr$ Magnetic Superlattices." Phys. Rev. Lett. **61**, 2472–2475 (1988).

[3] G. Binasch, P. Grünberg, F. Saurenbach, and W. Zinn. "Enhanced magnetoresistance in layered magnetic structures with antiferromagnetic interlayer exchange." Phys. Rev. B **39**, 4828–4830 (1989).

[4] M. Julliere. "Tunneling between ferromagnetic films." Phys. Lett. A **54**, 225–226 (1975).

[5] G. W. Fernando, A. N. Kocharian, R. E. Watson, and M. Weinert. "Stoner criterion of ferromagnetism and moment saturation in the Hubbard model with an applied magnetic field." Physica B **230**, 509 – 512 (1997).

[6] E. C. Stoner. "Collective Electron Ferromagnetism." Proc. R. Soc. A **165**, 372–414 (1938).

[7] M. S. S. Brooks, O. Eriksson, and B. Johansson. "$3d$-$5d$ band magnetism in rare earth transition metal intermetallics: $LuFe_2$." J. Phys.: Condens. Matter **1**, 5861 (1989).

[8] T. Lewowski and K. Wozniak. "Measurement of Curie temperature for gadolinium: a laboratory experiment for students." Eur. J. Phys. **18**, 453 (1997).

[9] K. D. Jayasuriya, S. J. Campbell, and A. M. Stewart. "Magnetic transitions in dysprosium: A specific-heat study." Phys. Rev. B **31**, 6032–6046 (1985).

[10] H. D. Arnold and G. W. Elmen. "Permalloy, A New Magnetic Material of Very High Permeability." Bell Syst. Tech. J. **2**, 101–111 (1923).

[11] L. F. Yin, *et al.* "Magnetocrystalline Anisotropy in Permalloy Revisited." Phys. Rev. Lett. **97**, 067203 (2006).

[12] E. Klokholm and J. A. Aboaf. "The saturation magnetostriction of permalloy films." J. Appl. Phys. **52**, 2474–2476 (1981).

[13] L. T. Baczewski, *et al.* "Magnetism in Rare-Earth-Transition Metal Systems. Magnetization Reversal and Ultra-High Susceptibility in Sandwiched Thin Films Based on Rare-earth and Cobalt Alloys." Acta. Phys. Pol. A **83**, 629 (1993).

[14] E. Burzo. "Magnetic properties and exchange interactions in rare-earth-iron-based compounds." Rom. Rep. Phys. **63**, 1316–1328 (2011).

[15] J. H. Van Vleck and R. Orbach. "Ferrimagnetic Resonance of Dilute Rare-Earth Doped Iron Garnets." Phys. Rev. Lett. **11**, 65–67 (1963).

[16] G. Woltersdorf, *et al.* "Damping by Slow Relaxing Rare Earth Impurities in $Ni_{80}Fe_{20}$." Phys. Rev. Lett. **102**, 257602 (2009).

[17] W. Heisenberg. "Zur Theorie des Ferromagnetismus." Z. Phys. **49**, 619–636 (1928).

[18] A. Hubert and R. Schäfer. *Magnetic Domains* (Springer-Verlag Berlin Heidelberg, 1998). ISBN 978-3-540-85054-0.

[19] G. Dieterle, *et al.* "Switching probabilities of magnetic vortex core reversal studied by table top magneto optic Kerr microscopy." Appl. Phys. Lett. **108**, 022401 (2016).

[20] L. Heyne, *et al.* "Relationship between Nonadiabaticity and Damping in Permalloy Studied by Current Induced Spin Structure Transformations." Phys. Rev. Lett. **100**, 066603 (2008).

[21] J. W. Lau, J. K. Bording, M. Beleggia, and Y. Zhu. "Energy barrier to magnetic vortex nucleation." Appl. Phys. Lett. **88**, 012508 (2006).

[22] U. Atxitia, D. Hinzke, and U. Nowak. "Fundamentals and applications of the Landau-Lifshitz-Bloch equation." J. Phys. D: Appl. Phys. **50**, 033003 (2017).

[23] S. Blundell. *Magnetism in Condensed Matter.* Oxford Master Series in Condensed Matter Physics 4 (OUP Oxford, 2001). ISBN 978-0-1985-0592-1.

[24] C. Abert, *et al.* "Numerical methods for the stray-field calculation: A comparison of recently developed algorithms." J. Magn. Magn. Mater. **326**, 176 – 185 (2013).

[25] A. Aharoni. "Demagnetizing factors for rectangular ferromagnetic prisms." J. Appl. Phys. **83**, 3432–3434 (1998).

[26] M.-F. Lai and C.-N. Liao. "Size dependence of C and S states in circular and square Permalloy dots." J. Appl. Phys. **103**, 07E737 (2008).

[27] C. A. F. Vaz, *et al.* "Multiplicity of magnetic domain states in circular elements probed by photoemission electron microscopy." Phys. Rev. B **72**, 224426 (2005).

[28] A. Aharoni. "Brown's "fundamental theorem" revisited." J. Appl. Phys. **90**, 4645–4650 (2001).

[29] R. F. Butler and S. K. Banerjee. "Single-domain grain size limits for metallic iron." J. Geophys. Res. **80**, 252–259 (1975).

[30] D. Sander. "The magnetic anisotropy and spin reorientation of nanostructures and nanoscale films." J. Phys.: Condens. Matter **16**, R603 (2004).

[31] R. Skomski, A. Kashyap, and A. Enders. "Is the magnetic anisotropy proportional to the orbital moment?" J. Appl. Phys. **109**, 07E143 (2011).

[32] J. Kirschner. *Polarized Electrons at Surfaces*. Springer Tracts in Modern Physics (Springer-Verlag Berlin Heidelberg, 1985). ISBN 978-3-6621-5219-5.

[33] F. J. Darnell and E. P. Moore. "Crystal Structure of Dysprosium at Low Temperatures." J. Appl. Phys. **34**, 1337–1338 (1963).

[34] R. Z. Levitin, *et al.* "Nature of the Magnetic Anisotropy of Dysprosium: Investigation of the Anisotropy of Dysprosium-Gadolinium Alloys." J. Exp. Theor. Phys. **35**, 968 (1972).

[35] J. García-Otero, M. Porto, J. Rivas, and A. Bunde. "Influence of the cubic anisotropy constants on the hysteresis loops of single-domain particles: A Monte Carlo study." J. Appl. Phys. **85**, 2287–2292 (1999).

[36] P. Bruno. *Physical origins and theoretical models of magnetic anisotropy*. Schriften des Forschungszentrums Jülich (OUP Oxford, 1993). ISBN 3-89336-110-3.

[37] J. H. Phillips and R. G. Shephard. "The variation of the magnetocrystalline anisotropy of 4% molybdenum permalloys with composition and temperature." J. Phys. D: Appl. Phys. **3**, 1605 (1970).

[38] E. Machlin. *Materials Science in Microelectronics II: The Effects of Structure on Properties in Thin Films*. Materials science in microelectronics (Elsevier Science, 2010). ISBN 978-0-0804-6040-6.

[39] W. F. Brown. "Micromagnetics: Successor to domain theory?" J. Phys. Radium **20**, 101–104 (1959).

[40] D. C. Ralph and M. D. Stiles. "Spin transfer torques." J. Magn. Magn. Mater. **320**, 1190–1216 (2008).

[41] S. Chikazumi. *Physics of Ferromagnetism* (Oxford University Press, 1997). ISBN 0-19851-776-9.

[42] R. P. Cowburn. "Property variation with shape in magnetic nanoelements." J. Phys. D: Appl. Phys. **33**, R1 (2000).

[43] M. Prutton. "Cross-tie walls in thin permalloy films." Philos. Mag. **5**, 625–633 (1960).

[44] J. P. Jakubovics. "Comments on the definition of ferromagnetic domain wall width." Philos. Mag. **38**, 401–406 (1978).

[45] L. D. Landau and E. Lifshitz. "On the theory of the dispersion of magnetic permeability in ferromagnetic bodies." Phys. Z. Sowjet. **8**, 153 (1935).

[46] T. L. Gilbert. "A phenomenological theory of damping in ferromagnetic materials." IEEE Trans. Magn. **40**, 3443–3449 (2004).

[47] MicroMagnum. "http://micromagnum.informatik.uni-hamburg.de." .

[48] L. Berger. "Exchange interaction between ferromagnetic domain wall and electric current in very thin metallic films." J. Appl. Phys. **55**, 1954–1956 (1984).

[49] J. C. Slonczewski. "Current-driven excitation of magnetic multilayers." J. Magn. Magn. Mater. **159**, L1 – L7 (1996).

[50] O. Boulle, G. Malinowski, and M. Kläui. "Current-induced domain wall motion in nanoscale ferromagnetic elements." Mater. Sci. Eng. R-Rep. **72**, 159–187 (2011).

[51] S. Zhang and Z. Li. "Roles of Nonequilibrium Conduction Electrons on the Magnetization Dynamics of Ferromagnets." Phys. Rev. Lett. **93**, 127204 (2004).

[52] A. Mougin, *et al.* "Domain wall mobility, stability and Walker breakdown in magnetic nanowires." EPL **78**, 57007 (2007).

[53] N. L. Schryer and L. R. Walker. "The motion of 180° domain walls in uniform dc magnetic fields." J. Appl. Phys. **45**, 5406–5421 (1974).

[54] A. Thiaville, Y. Nakatani, J. Miltat, and Y. Suzuki. "Micromagnetic understanding of current-driven domain wall motion in patterned nanowires." EPL **69**, 990–996 (2005).

[55] F. Bitter. "On Inhomogeneities in the Magnetization of Ferromagnetic Materials." Phys. Rev. **38**, 1903–1905 (1931).

[56] J. R. Garrood. "Methods of Improving the Sensitivity of the Bitter Technique." Proc. Phys. Soc. **79**, 1252 (1962).

[57] P. Rice and J. Moreland. "A new look at the Bitter method of magnetic imaging." Rev. Sci. Instrum. **62**, 844–845 (1991).

[58] O. Kitakami, T. Sakurai, and Y. Shimada. "High density recorded patterns observed by high-resolution Bitter scanning electron microscope method." J. Appl. Phys. **79**, 6074–6076 (1996).

[59] A. Okuda, J. Ichihara, and Y. Majima. "Scanning Lorentz force microscopy." Appl. Phys. Lett. **81**, 2872–2874 (2002).

[60] T. Warwick, *et al.* "A scanning transmission x-ray microscope for materials science spectromicroscopy at the advanced light source." Rev. Sci. Instrum. **69**, 2964–2973 (1998).

[61] S. Imada, S. Suga, W. Kuch, and J. Kirschner. "Magnetic Microspectroscopy by a Combination of XMCD and PEEM." Surf. Rev. Lett. **09**, 877–881 (2002).

[62] R. P. Gunawardane and C. R. Arumainayagam. *Auger Electron Spectroscopy*, pp. 451–483 (Springer US, Boston, MA, 2006). ISBN 978-0-3873-7590-8.

[63] R. Schneider. *Energy-Dispersive X-Ray Spectroscopy (EDXS)*, pp. 293–310 (Wiley-VCH Verlag GmbH & Co. KGaA, 2011). ISBN 978-3-5276-3692-1.

[64] M. P. Seah and W. A. Dench. "Quantitative electron spectroscopy of surfaces: A standard data base for electron inelastic mean free paths in solids." Surf. Interface Anal. **1**, 2–11 (1979).

[65] M. Erbudak and G. Ravano. "Polarized secondary electron spectroscopy, a new tool in solid state sciences." Surf. Sci. **126**, 120 – 125 (1983).

[66] J. Kirschner and K. Koike. "Spin polarization of secondary electrons from $Fe(110)$ excited by unpolarized primary electrons." Surf. Sci. **273**, 147 – 159 (1992).

[67] C. M. Schneider. "Soft X-ray photoemission electron microscopy as an element-specific probe of magnetic microstructures." J. Magn. Magn. Mater. **175**, 160 – 176 (1997).

[68] R. Van Grieken and A. Markowicz. *Handbook of X-Ray Spectrometry* (CRC Press, 2001). ISBN 978-0-8247-0600-5.

[69] J. Goldstein, *et al. Scanning Electron Microscopy and X-ray Microanalysis* (Springer US, 2003). ISBN 978-0-3064-7292-3.

[70] R. Frömter, S. Hankemeier, H. P. Oepen, and J. Kirschner. "Optimizing a low-energy electron diffraction spin-polarization analyzer for imaging of magnetic surface structures." Rev. Sci. Instrum. **82**, 033704 (2011).

[71] T. Kohashi, M. Konoto, and K. Koike. "High-resolution spin-polarized scanning electron microscopy (spin SEM)." J. Electron Microsc. **59**, 43–52 (2010).

[72] G. Schönhense and H. C. Siegmann. "Transmission of electrons through ferromagnetic material and applications to detection of electron spin polarization." Ann. Phys. **505**, 465–474 (1993).

[73] M. Getzlaff, J. Bansmann, and G. Schönhense. "Spin-Polarization Effects For Electrons Passing Through Thin Iron And Cobalt Films." Solid State Comm. **87**, 467–469 (1993).

[74] J. Unguris. "6. Scanning electron microscopy with polarization analysis (SEMPA) and its applications." Experimental Methods in the Physical Sciences **36**, 167 – XVI (2001).

[75] D. L. Abraham and H. Hopster. "Magnetic probing depth in spin-polarized secondary electron spectroscopy." Phys. Rev. Lett. **58**, 1352–1354 (1987).

[76] E. Fues and H. Hellmann. "Über polarisierte Elektronenwellen." Physik. Z. **31**, 465 – 478 (1930).

[77] G. Chrobok and M. Hofmann. "Electron spin polarization of secondary electrons ejected from magnetized europium oxide." Phys. Lett. A **57**, 257 – 258 (1976).

[78] K. Koike and K. Hayakawa. "Scanning Electron Microscope Observation of Magnetic Domains Using Spin-Polarized Secondary Electrons." Jpn. J. Appl. Phys. **23**, L187 (1984).

[79] K. Koike and K. Hayakawa. "Spin Polarization of Electron-Excited Secondary Electrons from a Permalloy Polycrystal." Jpn. J. Appl. Phys. **23**, L85 (1984).

[80] K. Koike, H. Matsuyama, H. Todokoro, and K. Hayakawa. "Spin-Polarized Scanning Electron Microscope for Magnetic Domain Observation." Jpn. J. Appl. Phys. **24**, L542 (1985).

[81] M. R. Scheinfein, *et al.* "Scanning electron microscopy with polarization analysis (SEMPA)." Rev. Sci. Instrum. **61**, 2501–2527 (1990).

[82] R. M. Reeve, *et al.* "Magnetic domain structure of $La_{0.7}Sr_{0.3}MnO_3$ thin-films probed at variable temperature with scanning electron microscopy with polarization analysis." Appl. Phys. Lett. **102** (2013).

[83] S.-H. Chung, D. T. Pierce, and J. Unguris. "Simultaneous measurement of magnetic vortex polarity and chirality using scanning electron microscopy with polarization analysis (SEMPA)." Ultramicroscopy **110**, 177 – 181 (2010).

[84] E. Kisker, W. Gudat, and K. Schröder. "Observation of a high spin polarization of secondary electrons from single crystal Fe and Co." Solid State Commun. **44**, 591 – 595 (1982).

[85] H. Hopster, *et al.* "Evidence for Spin-Dependent Electron-Hole-Pair Excitations in Spin-Polarized Secondary-Electron Emission from Ni(110)." Phys. Rev. Lett. **50**, 70–73 (1983).

[86] J. S. Helman. "Structure of the spin polarization spectrum of secondary electrons emitted from nickel." Solid State Commun. **57**, 505 – 507 (1986).

[87] N. F. Mott. "The Scattering of Fast Electrons by Atomic Nuclei." Proc. R. Soc. A **124**, 425–442 (1929).

[88] K. Koike and K. Hayakawa. "Scanning Electron Microscope Observation of Magnetic Domains Using Spin-Polarized Secondary Electrons." Jpn. J. Appl. Phys. **23**, L187 (1984).

[89] M. R. Scheinfein, *et al.* "Improved low-energy diffuse scattering electron-spin polarization analyzer." Rev. Sci. Instrum. **60**, 1–11 (1989).

[90] H. P. Oepen, G. Steierl, and J. Kirschner. "Scanning electron microscope with polarization analysis: Micromagnetic structures in ultrathin films." J. Vac. Sci. Technol. B Nanotechnol. Microelectron. **20**, 2535–2538 (2002).

[91] M. Escher, *et al.* "FERRUM: A New Highly Efficient Spin Detector for Electron Spectroscopy." e-J. Surf. Sci. Nanotech **9**, 340–343 (2011).

[92] D. Kutnyakhov, *et al.* "Imaging spin filter for electrons based on specular reflection from iridium (001)." Ultramicroscopy **130**, 63–69 (2013).

[93] R. W. DeBlois and C. D. Graham Jr. "Domain Observations on Iron Whiskers." J. Appl. Phys. **29**, 931–939 (1958).

[94] S. A. Gusev, V. N. Petrov, and E. V. Skorokhodov. "Problems of implementing SEMPA in experiments." J. Surf. Invest.: X-Ray, Synchrotron Neutron Tech. **4**, 582–587 (2010).

[95] M. Kläui, *et al.* "Direct Observation of Domain-Wall Configurations Transformed by Spin Currents." Phys. Rev. Lett. **95**, 026601 (2005).

[96] S. N. Samarin, *et al.* "Elastic versus inelastic spin-polarized electron scattering from a ferromagnetic surface." Phys. Rev. B **94**, 155440 (2016).

[97] P. Weinberger. "John Kerr and his effects found in 1877 and 1878." Philos. Mag. Lett. **88**, 897–907 (2008).

[98] J. Zak, E. R. Moog, C. Liu, and S. D. Bader. "Fundamental magneto-optics." J. Appl. Phys. **68**, 4203–4207 (1990).

[99] C. Tannous and J. Gieraltowski. "The Stoner-Wohlfarth model of ferromagnetism." Eur. J. Phys. **29**, 475 (2008).

[100] C. You and S. Shin. "Derivation of simplified analytic formulae for magneto-optical Kerr effects." Appl. Phys. Lett. **69**, 1315–1317 (1996).

[101] J. Hamrle, *et al.* "Analytical expression of the magneto-optical Kerr effect and Brillouin light scattering intensity arising from dynamic magnetization." J. Phys. D: Appl. Phys. **43**, 325004 (2010).

[102] J. R. Black. "Electromigration - A brief survey and some recent results." IEEE Trans. Electron. Dev. **16**, 338–347 (1969).

[103] B. D. Josephson. "Possible new effects in superconductive tunnelling." Phys. Lett. **1**, 251 – 253 (1962).

[104] P. W. Anderson and J. M. Rowell. "Probable Observation of the Josephson Superconducting Tunneling Effect." Phys. Rev. Lett. **10**, 230–232 (1963).

[105] R. C. Jaklevic, J. Lambe, A. H. Silver, and J. E. Mercereau. "Quantum Interference Effects in Josephson Tunneling." Phys. Rev. Lett. **12**, 159–160 (1964).

[106] R. L. Fagaly. "Superconducting quantum interference device instruments and applications." Rev. Sci. Instrum. **77**, 101101 (2006).

[107] C. Kittel. "On the Theory of Ferromagnetic Resonance Absorption." Phys. Rev. **73**, 155–161 (1948).

[108] K. Eason, M. P. R. G. Sabino, M. Tran, and Y. F. Liew. "Origins of magnetic damping measurement variations using ferromagnetic resonance for nano-sized devices." Appl. Phys. Lett. **102**, 232405 (2013).

[109] R. D. McMichael, D. J. Twisselmann, and A. Kunz. "Localized Ferromagnetic Resonance in Inhomogeneous Thin Films." Phys. Rev. Lett. **90**, 227601 (2003).

[110] C. Chappert, *et al.* "Ferromagnetic resonance studies of very thin cobalt films on a gold substrate." Phys. Rev. B **34**, 3192–3197 (1986).

[111] R. Arias and D. L. Mills. "Extrinsic contributions to the ferromagnetic resonance response of ultrathin films." Phys. Rev. B **60**, 7395–7409 (1999).

[112] E. Rutherford. "LXXIX. The scattering of α and β particles by matter and the structure of the atom." Philos. Mag. **21**, 669–688 (1911).

[113] W.-K. Chu, J. W. Mayer, and M.-A. Nicolet. *Backscattering Spectroscopy* (Academic Press, 1978). ISBN 0-12173-850-7.

[114] J. F. Ziegler, M. D. Ziegler, and J. P. Biersack. "SRIM - The stopping and range of ions in matter (2010)." Nucl. Instr. Meth. Phys. Res. B **268**, 1818 – 1823 (2010). 19th International Conference on Ion Beam Analysis.

[115] H. Duan, *et al.* "Sub-10-nm half-pitch electron-beam lithography by using poly(methyl methacrylate) as a negative resist." J. Vac. Sci. Technol. B Nanotechnol. Microelectron. **28**, C6C58–C6C62 (2010).

[116] B. Cord, *et al.* "Limiting factors in sub-10nm scanning-electron-beam lithography." J. Vac. Sci. Technol. B Nanotechnol. Microelectron. **27**, 2616–2621 (2009).

[117] M. Morita, *et al.* "Growth of native oxide on a silicon surface." J. Appl. Phys. **68**, 1272–1281 (1990).

[118] K. Kim, *et al.* "Growth law of silicon oxides by dry oxidation." Semicond. Sci. Techn. **11**, 1059 (1996).

[119] A. Athanassouli, T. Ganetsos, F. Klose, and S. Messoloras. "Morphology and oxidation kinetics of SiO_2 layers on silicon." Semicond. Sci. Techn. **17**, 65 (2002).

[120] M. Stepanova and S. Dew. *Nanofabrication: Techniques and Principles* (Springer Vienna, 2012). ISBN 978-3-7091-0423-1.

[121] M. Foerster, *et al. Domain Wall Memory Device*, pp. 1387–1441 (Springer Netherlands, Dordrecht, 2016). ISBN 978-9-4007-6892-5.

[122] R. P. Cowburn. "Property variation with shape in magnetic nanoelements." J. Phys. D: Appl. Phys. **33**, R1 (2000).

[123] J.-G. Zhu, Y. Zheng, and G. A. Prinz. "Ultrahigh density vertical magnetoresistive random access memory (invited)." J. Appl. Phys. **87**, 6668 (2000).

[124] A. Imre, *et al.* "Application of mesoscopic magnetic rings for logic devices." In *Nanotechnology, 2004. 4th IEEE Conference on*, pp. 137–139 (2004).

[125] U. Welp, *et al.* "Magnetization reversal in arrays of individual and coupled Co-rings." J. Appl. Phys. **93**, 7056–7058 (2003).

[126] M. Kläui, C. A. F. Vaz, L. Lopez-Diaz, and J. A. C. Bland. "Vortex formation in narrow ferromagnetic rings." J. Phys. Condens. Matter **15**, R985 (2003).

[127] F. J. Castaño, *et al.* "Metastable states in magnetic nanorings." Phys. Rev. B **67**, 184425 (2003).

[128] T. Uhlig and J. Zweck. "Direct Observation of Switching Processes in Permalloy Rings with Lorentz Microscopy." Phys. Rev. Lett. **93**, 047203 (2004).

[129] J. Rothman, *et al.* "Observation of a Bi-Domain State and Nucleation Free Switching in Mesoscopic Ring Magnets." Phys. Rev. Lett. **86**, 1098–1101 (2001).

[130] M. Kläui. "Head-to-head domain walls in magnetic nanostructures." J. Phys.: Condens. Matter **20**, 313001 (2008).

[131] Y. Nakatani, A. Thiaville, and J. Miltat. "Head-to-head domain walls in soft nanostrips: a refined phase diagram." J. Magn. Magn. Mater. **290–291, Part 1**, 750–753 (2005). Proceedings of the Joint European Magnetic Symposia (JEMS' 04).

[132] R. Wieser, U. Nowak, and K. D. Usadel. "Domain wall mobility in nanowires: Transverse versus vortex walls." Phys. Rev. B **69**, 064401 (2004).

[133] R. D. McMichael and M. J. Donahue. "Head to head domain wall structures in thin magnetic strips." IEEE Trans. Magn. **33**, 4167–4169 (1997).

[134] N. Rougemaille, *et al.* "Phase diagram of magnetic domain walls in spin valve nano-stripes." Appl. Phys. Lett. **100**, 172404 (2012).

[135] V. D. Nguyen, *et al.* "Third type of domain wall in soft magnetic nanostrips." Sci. Rep. **5**, 12417 (2015).

[136] S. Jamet, N. Rougemaille, J.-C. Toussain, and O. Fruchart. "Head-to-head domain walls in one-dimensional nanostructures: an extended phase diagram ranging from strips to cylindrical wires." arXiv:1412.0679 (2015).

[137] N. Wiese, *et al.* "On the scaling behaviour of cross-tie domain wall structures in patterned $NiFe$ elements." EPL **80**, 57003 (2007).

[138] A. Thiaville, Y. Nakatani, J. Miltat, and Y. Suzuki. "Micromagnetic understanding of current-driven domain wall motion in patterned nanowires." EPL **69** (2005).

[139] S. Finizio, *et al.* "Magnetic configurations in nanostructured Co_2MnGa thin film elements." New J. Phys. **17**, 083030 (2015).

[140] S. Finizio, *et al.* "Domain wall transformations and hopping in $La_{0.7}Sr_{0.3}MnO_3$ nanostructures imaged with high resolution x-ray magnetic microscopy." J. Phys.: Condens. Matter **26**, 456003 (2014).

[141] D. Backes, *et al.* "Transverse domain walls in nanoconstrictions." Appl. Phys. Lett. **91**, 112502 (2007).

[142] D. Petit, *et al.* "Magnetic imaging of the pinning mechanism of asymmetric trans-verse domain walls in ferromagnetic nanowires." Appl. Phys. Lett. **97**, 233102 (2010).

[143] S. Glathe and R. Mattheis. "Magnetic domain wall pinning by kinks in magnetic nanostripes." Phys. Rev. B **85**, 024405 (2012).

[144] S. Glathe, *et al.* "Splitting of a moving transverse domain wall in a magnetic nanos-tripe in a transverse field." Phys. Rev. B **81**, 020412 (2010).

[145] M. J. Donahue and D. G. Porter. OOMF User's Guide Version 1.0 (1999).

[146] T. J. Bromwich, A. K. Petford-Long, F. J. Castaño, and C. A. Ross. "Lorentz microscopy of elliptical magnetic rings." J. Appl. Phys. **99**, 08H304 (2006).

[147] M. Kläui, *et al.* "Magnetic states in wide annular structures." J. Appl. Phys. **99**, 08G308 (2006).

[148] P. E. Roy, *et al.* "Antivortex domain walls observed in permalloy rings via magnetic forec microscopy." Phys. Rev. B **79**, 060407(R) (2009).

[149] M. H. Park, *et al.* "Vortex head-to-head domain walls and their formation in onion-state ring elements." Phys. Rev. B **73**, 094424 (2006).

[150] M. Hayashi, *et al.* "Dependence of Current and Field Driven Depinning of Domain Walls on Their Structure and Chirality in Permalloy Nanowires." Phys. Rev. Lett. **97**, 207205 (2006).

[151] M. Laufenberg, *et al.* "Quantitative determination of domain wall coupling energetics." Appl. Phys. Lett. **88**, 212510 (2006).

[152] T. J. Hayward, *et al.* "Direct imaging of domain-wall interactions in $Ni_{80}Fe_{20}$ planar nanowires." Phy. Rev. B **81**, 020410 (2010).

[153] T. Miyawaki, *et al.* "Magnetic interaction of submicron-sized ferromagnetic rings in one-dimensionsal array." Appl. Phys. Lett. **89**, 122508 (2006).

[154] V. Estévez and L. Laurson. "Head-to-head domain wall structures in wide permalloy strips." Phys. Rev. B **91**, 054407 (2015).

[155] M. Kläui, *et al.* "Direct observation of spin configurations and classification of switching processes in mesoscopic ferromagnetic rings." Phys. Rev. B **68**, 134426 (2003).

[156] K. J. Harte. "Theory of Magnetization Ripple in Ferromagnetic Films." J. Appl. Phys. **39**, 1503–1524 (1968).

[157] W. C. Uhlig, M. J. Donahue, D. T. Pierce, and J. Unguris. "Direct imaging of current-driven domain walls in ferromagnetic nanostripes." J. Appl. Phys. **105**, 103902 (2009).

[158] M. Kläui, *et al.* "Domain wall behaviour at constrictions in ferromagnetic ring structures." Physica B **343**, 343–349 (2004).

[159] B. Krüger, *et al.* "Current-driven domain-wall dynamics in curved ferromagnetic nanowires." Phys. Rev. B **75**, 054421 (2007).

[160] M. J. Donahue and R. D. McMichael. "Micromagnetics on Curved Geometries Using Rectangular Cells: Error Correction and Analysis." IEEE Trans. Magn. **43**, 2878–2880 (2007).

[161] C. A. F. Vaz, *et al.* "Multiplicity of magnetic domain states in circular elements probed by photoemission electron microscopy." Phys. Rev. B **72**, 224426 (2005).

[162] I. Hashim, H. S. Joo, and H. A. Atwater. "Structural and Magnetic Properties of Epitaxial $Ni_{80}Fe_{20}$ Thin Films on Cu/Si." Surf. Rev. Lett. **2**, 427 (1995).

[163] C. H. Park and D. J. Chadi. "Hydrogen-Mediated Spin-Spin Interaction in $ZnCoO$." Phys. Rev. Lett. **94**, 127204 (2005).

[164] Z. Li and S. Zhang. "Domain-wall dynamics driven by adiabatic spin-transfer torques." Phys. Rev. B **70**, 024417 (2004).

[165] X. Wang, *et al.* "Steady-state domain wall motion driven by adiabatic spin-transfer torque with assistance of microwave field." Appl. Phys. Lett. **103**, 262408 (2013).

[166] D. Wang, *et al.* "Domain wall motion driven by adiabatic spin transfer torque through excitation of nonlinear dynamics." J. Phys.: Condens. Matter **28**, 206005 (2016).

[167] A. Thiaville, Y. Nakatani, J. Miltat, and Y. Suzuki. "Micromagnetic understanding of current-driven domain wall motion in patterned nanowires." EPL **69**, 990–996 (2005).

[168] G. Tatara, *et al.* "Spin Torque and Force due to Current for General Spin Textures." J. Phys. Soc. Jpn. **76**, 054707 (2007).

[169] G. Tatara, *et al.* "Threshold Current of Domain Wall Motion under Extrinsic Pinning, β-Term and Non-Adiabaticity." J. Phys. Soc. Jpn. **75**, 064708 (2006).

[170] T. Valet and A. Fert. "Theory of the perpendicular magnetoresistance in magnetic multilayers." Phys. Rev. B **48**, 7099–7113 (1993).

[171] L. Berger. "Spin relaxation in metallic ferromagnets." Phys. Rev. B **83**, 054410 (2011).

[172] S. D. Steenwyk, *et al.* "Perpendicular-current exchange-biased spin-valve evidence for a short spin-diffusion length in permalloy." J. Magn. Magn. Mater. **170** (1997).

[173] S. Dubois, *et al.* "Evidence for a short spin diffusion length in permalloy from the giant magnetoresistance of multilayered nanowires." Phys. Rev. B **60**, 477–484 (1999).

[174] T. Kimura, J. Hamrle, and Y. Otani. "Estimation of spin-diffusion length from the magnitude of spin-current absorption: Multiterminal ferromagnetic/nonferromagnetic hybrid structures." Phys. Rev. B **72**, 014461 (2005).

[175] A. A. Starikov, *et al.* "Unified First-Principles Study of Gilbert Damping, Spin-Flip Diffusion, and Resistivity in Transition Metal Alloys." Phys. Rev. Lett. **105**, 236601 (2010).

[176] C. E. Moreau, I. C. Moraru, N. O. Birge, and W. P. Pratt Jr. "Measurement of spin diffusion length in sputtered Ni films using a special exchange-biased spin valve geometry." Appl. Phys. Lett. **90**, 012101 (2007).

[177] R. H. Wade. "The Determination of Domain Wall Thickness in Ferromagnetic Films by Electron Microscopy." Proc. Phys. Soc. **79**, 1237 (1962).

[178] S. McVitie and J. N. Chapman. "Measurement of domain wall widths in Permalloy using differential phase contrast imaging in stem." J. Magn. Magn. Mater. **83**, 97 – 98 (1990).

[179] J. N. Chapman, R. Ploessl, and D. M. Donnet. "Differential phase contrast microscopy of magnetic materials." Ultramicroscopy **47**, 331 – 338 (1992).

[180] S. Urazhdin, R. Loloee, and W. P. Pratt. "Noncollinear spin transport in magnetic multilayers." Phys. Rev. B **71**, 100401 (2005).

[181] G. Tatara and P. Entel. "Calculation of current-induced torque from spin continuity equation." Phys. Rev. B **78**, 064429 (2008).

[182] K. Gilmore, Y. U. Idzerda, and M. D. Stiles. "Identification of the Dominant Precession-Damping Mechanism in Fe, Co, and Ni by First-Principles Calculations." Phys. Rev. Lett. **99**, 027204 (2007).

[183] I. Garate, K. Gilmore, M. D. Stiles, and A. H. MacDonald. "Nonadiabatic spin-transfer torque in real materials." Phys. Rev. B **79**, 104416 (2009).

[184] J. Xiao, A. Zangwill, and M. D. Stiles. "Spin-transfer torque for continuously variable magnetization." Phys. Rev. B **73**, 054428 (2006).

[185] K.-J. Lee, *et al.* "Self-consistent calculation of spin transport and magnetization dynamics." Phys. Rep. **531**, 89 – 113 (2013).

[186] C. A. Akosa, *et al.* "Role of spin diffusion in current-induced domain wall motion for disordered ferromagnets." Phys. Rev. B **91**, 094411 (2015).

[187] X. Waintal and M. Viret. "Current-induced distortion of a magnetic domain wall." EPL **65**, 427 (2004).

[188] G. Tatara and H. Kohno. "Theory of Current-Driven Domain Wall Motion: Spin Transfer versus Momentum Transfer." Phys. Rev. Lett. **92**, 086601 (2004).

[189] J. Shibata, G. Tatara, and H. Kohno. "A brief review of field- and current-driven domain-wall motion." J. Phys. D: Appl. Phys. **44**, 384004 (2011).

[190] K. Sekiguchi, *et al.* "Time-Domain Measurement of Current-Induced Spin Wave Dynamics." Phys. Rev. Lett. **108**, 017203 (2012).

[191] J.-Y. Chauleau, *et al.* "Self-consistent determination of the key spin-transfer torque parameters from spin-wave Doppler experiments." Phys. Rev. B **89**, 020403 (2014).

[192] M. C. Hickey, *et al.* "Spin-transfer torque efficiency measured using a Permalloy nanobridge." Appl. Phys. Lett. **97**, 202505 (2010).

[193] M. Eltschka, *et al.* "Nonadiabatic Spin Torque Investigated Using Thermally Activated Magnetic Domain Wall Dynamics." Phys. Rev. Lett. **105**, 056601 (2010).

[194] R. Moriya, *et al.* "Probing vortex-core dynamics using current-induced resonant excitation of a trapped domain wall." Nature Phys. **4**, 368–372 (2008).

[195] E. Martinez, L. Lopez-Diaz, O. Alejos, and L. Torres. "Resonant domain wall depinning induced by oscillating spin-polarized currents in thin ferromagnetic strips." Phys. Rev. B **77**, 144417 (2008).

[196] G. S. D. Beach, M. Tsoi, and J. L. Erskine. "Current-induced domain wall motion." J. Magn. Magn. Mater. **320**, 1272 – 1281 (2008).

[197] G. S. D. Beach, *et al.* "Nonlinear Domain-Wall Velocity Enhancement by Spin-Polarized Electric Current." Phys. Rev. Lett. **97**, 057203 (2006).

[198] G. Meier, *et al.* "Direct Imaging of Stochastic Domain-Wall Motion Driven by Nanosecond Current Pulses." Phys. Rev. Lett. **98**, 187202 (2007).

[199] T. A. Moore, *et al.* "Scaling of spin relaxation and angular momentum dissipation in permalloy nanowires." Phys. Rev. B **80**, 132403 (2009).

[200] L. Thomas, R. Moriya, C. Rettner, and S. S. P. Parkin. "Dynamics of Magnetic Domain Walls Under Their Own Inertia." Science **330**, 1810–1813 (2010).

[201] S. D. Pollard, *et al.* "Direct dynamic imaging of non-adiabatic spin torque effects." Nat. Commun. **3**, 1028 (2012).

[202] A. Bisig, *et al.* "Enhanced Nonadiabaticity in Vortex Cores due to the Emergent Hall Effect." Phys. Rev. Lett. **117**, 277203 (2016).

[203] L. Heyne. *Manipulation of Magnetic Domain Walls and Vortices by Current Injection.* Ph.D. thesis, Universität Konstanz, Konstanz (2010).

[204] L. Heyne, *et al.* "Direct Determination of Large Spin-Torque Nonadiabaticity in Vortex Core Dynamics." Phys. Rev. Lett. **105**, 187203 (2010).

[205] S. Rößler, *et al.* "Nonadiabatic spin-transfer torque of magnetic vortex structures in a permalloy square." Phys. Rev. B **89**, 174426 (2014).

[206] D. Claudio-Gonzalez, A. Thiaville, and J. Miltat. "Domain Wall Dynamics under Nonlocal Spin-Transfer Torque." Phys. Rev. Lett. **108**, 227208 (2012).

[207] S. Lepadatu, *et al.* "Domain-wall pinning, nonadiabatic spin-transfer torque, and spin-current polarization in permalloy wires doped with vanadium." Phys. Rev. B **81**, 020413 (2010).

[208] Y. Tserkovnyak, A. Brataas, and G. E. W. Bauer. "Theory of current-driven magnetization dynamics in inhomogeneous ferromagnets." J. Magn. Magn. Mater. **320**, 1282 – 1292 (2008).

[209] K.-W. Kim, K.-J. Lee, H.-W. Lee, and M. D. Stiles. "Intrinsic spin torque without spin-orbit coupling." Phys. Rev. B **92**, 224426 (2015).

[210] H. Kohno, G. Tatara, and J. Shibata. "Microscopic Calculation of Spin Torques in Disordered Ferromagnets." J. Phys. Soc. Jpn. **75**, 113706 (2006).

[211] Y. Tserkovnyak, H. J. Skadsem, A. Brataas, and G. E. W. Bauer. "Current-induced magnetization dynamics in disordered itinerant ferromagnets." Phys. Rev. B **74**, 144405 (2006).

[212] B. Krüger, *et al.* "Proposal of a Robust Measurement Scheme for the Nonadiabatic Spin Torque Using the Displacement of Magnetic Vortices." Phys. Rev. Lett. **104**, 077201 (2010).

[213] A. A. Thiele. "Steady-State Motion of Magnetic Domains." Phys. Rev. Lett. **30**, 230–233 (1973).

[214] B. Krüger, *et al.* "Harmonic oscillator model for current- and field-driven magnetic vortices." Phys. Rev. B **76**, 224426 (2007).

[215] N. A. Usov and S. E. Peschany. "Magnetization curling in a fine cylindrical particle." J. Magn. Magn. Mater. **118**, L290 – L294 (1993).

[216] L. Heyne and M. Kläui. "Analytical Description for Current-Induced Vortex Core Displacement." J. Appl. Phys. **109**, 07C908 (2011).

[217] J. Fassbender, *et al.* "Introducing artificial length scales to tailor magnetic properties." New J. Phys. **11**, 125002 (2009).

[218] A. García-Arribas, *et al.* "Tailoring the magnetic anisotropy of thin film permalloy microstrips by combined shape and induced anisotropies." Eur. Phys. J. B **86**, 136 (2013).

[219] S. G. Reidy, L. Cheng, and W. E. Bailey. "Dopants for independent control of precessional frequency and damping in $Ni_{81}Fe_{19}$ (50 nm) thin films." Appl. Phys. Lett. **82**, 1254–1256 (2003).

[220] A. A. Baker, A. I. Figueroa, G. van der Laan, and T. Hesjedal. "Tailoring of magnetic properties of ultrathin epitaxial Fe films by Dy doping." AIP Adv. **5**, 077117 (2015).

[221] C. Kittel. "Ferromagnetic resonance." J. Phys. Radium **12**, 291–302 (1951).

[222] B. Van Waeyenberge, *et al.* "Magnetic vortex core reversal by excitation with short bursts of an alternating field." Nature **444**, 461–464 (2006).

[223] G. B. M. Fior, *et al.* "Indirect switching of vortex polarity through magnetic dynamic coupling." J. Appl. Phys. **119**, 093906 (2016).

[224] Y. Gaididei, D. D. Sheka, and F. G. Mertens. "Controllable switching of vortex chirality in magnetic nanodisks by a field pulse." Appl. Phys. Lett. **92**, 012503 (2008).

[225] B. K. Liew, N. W. Cheung, and C. Hu. "Projecting interconnect electromigration lifetime for arbitrary current waveforms." IEEE Trans. Electron. Dev. **37**, 1343–1351 (1990).

[226] A. F. Mayadas, J. F. Janak, and A. Gangulee. "Resistivity of Permalloy thin films." J. Appl. Phys. **45**, 2780–2781 (1974).

[227] D.-J. Yao, W.-C. Lai, and H.-C. Chien. "Temperature Dependence of Thermal Conductivity for Silicon Dioxide." In *ASME 2008 First International Conference on Micro/Nanoscale Heat Transfer*, 42924, pp. 435–439 (2008).

[228] R. L. Compton and P. A. Crowell. "Dynamics of a Pinned Magnetic Vortex." Phys. Rev. Lett. **97**, 137202 (2006).

[229] Y. Xu, L. Scott Chumbley, G. A. Weigelt, and F. C. Laabs. "Analysis of interdiffusion of Dy, Nd, and Pr in Mg." J. Mater. Res. **16**, 3287 – 3292 (2001).

[230] Y. Zhao, *et al.* "Experimental Investigation of Temperature-Dependent Gilbert Damping in Permalloy Thin Films." Sci. Rep. **6**, 22890 (2016).

[231] B. Beyersdorff, *et al.* "Thermal effects in spin-torque assisted domain wall depinning." Phys. Rev. B **86**, 184427 (2012).

[232] C. Weißenfels and P. Wriggers. "Numerical modeling of electrical contacts." Computational Mechanics **46**, 301–314 (2010).

[233] H. Fangohr, *et al.* "Joule heating in nanowires." Phys. Rev. B **84**, 054437 (2011).

[234] P. L. Rosin. "Assessing Error of Fit Functions for Ellipses." Graph. Models Im. Proc. **5**, 494–502 (1996).

[235] W. Gander, G. H. Golub, and R. Strebel. "Least-squares fitting of circles and ellipses." BIT Numer. Math. **34**, 558–578 (1994).

[236] A. Fitzgibbon, M. Pilu, and R. B. Fisher. "Direct Least Square Fitting of Ellipses." IEEE Trans. Pattern Anal. Mach. Intell. **21**, 476–480 (1999).

[237] R. Halir and J. Flusser. "Numerically Stable Direct Least Squares Fitting Of Ellipses." (1998).

[238] K. T. McDonald. "Error Estimation in Fitting of Ellipses." (2014).

[239] J. A. J. Burgess, J. E. Losby, and M. R. Freeman. "An analytical model for vortex core pinning in a micromagnetic disk." J. Magn. Magn. Mater. **361**, 140 – 149 (2014).

[240] F. Junginger, *et al.* "Quantitative determination of vortex core dimensions in head-to-head domain walls using off-axis electron holography." Appl. Phys. Lett. **92**, 112502 (2008).

Danksagung

Aus Datenschutzgründen entfernt / Removed due to data privacy

Part I

Anhänge gemäß Prüfungsordnung

Eidesstattliche Erklärung

Hiermit erkläre ich an Eides statt, dass ich meine Dissertation selbständig und ohne fremde Hilfe verfasst und keine anderen als die von mir angegebenen Quellen und Hilfsmittel zur Erstellung meiner Dissertation verwendet habe. Die Arbeit ist in vorliegender oder ähnlicher Form bei keiner anderen Prüfungsbehörde zur Erlangung eines Doktorgrades eingereicht worden.

Mainz, den

Pascal Krautscheid

Lebenslauf

Aus Datenschutzgründen entfernt / Removed due to data privacy

Veröffentlichungen

Zeitschriftenartikel

P. Krautscheid, R. M. Reeve, D. Schönke, I. Boventer, A. Conca Parra, A. V. Chumak, B. Hillebrands, J. Ehrler, J. Osten, J. Fassbender und Mathias Kläui.
Correlation between Damping and Non-Adiabaticity probed via Current-Induced Vortex Core Displacement in Rare-Earth doped Permalloy Disks.
To be submitted

P. Krautscheid, R. M. Reeve, M. Lauf, B. Krüger und Mathias Kläui.
Domain wall spin structures in mesoscopic Fe rings probed by high resolution SEMPA.
J. Phys. D: Appl. Phys **49**, 425004 (2016)

M. Janoschek, M. Garst, A. Bauer, **P. Krautscheid**, R. Georgii, P. Boni, and C. Pfleiderer.
Fluctuation-induced first-order phase transition in Dzyaloshinskii-Moriya helimagnets.
Phys. Rev. B **87**, 134407 (2013)

Vorträge

R. M. Reeve, **P. Krautscheid**, M. Lauf, B. Krüger and M. Kläui.
High Resolution SEMPA Imaging of Domain Wall Spin Configurations in Mesoscopic Fe Rings.
Annual Conference on Magnetism and Magnetic Materials (MMM) 2016, New Orleans, USA.

R. M. Reeve, J.-S. Kim, A. Loescher, **P. Krautscheid**, M.-A. Mawass, A. Bisig, B. Krüger, J. Yoon, C-Y. You, M. Weigand, H. Stoll, G. Schütz, H. J. M. Swagten, B. Koopmans und M. Kläui.
Magnetic Microscopy of Nanoscale Domain Wall Devices.
Korean-German Network Workshop, Seoul National University, Korea.

P. Krautscheid, M. Lauf, R. M. Reeve, B. Krüger und M. Kläui
High Resolution Imaging of Nanoscale Structures using SEMPA.
Joint Conference Magnetism and Magnetic Materials - IEEE International Magnetics 2016, San Diego, USA.

R. M. Reeve, C. Mix, M. König, **P. Krautscheid**, C. Engel, M. Foerster, G. Jakob und M. Kläui.
Magnetic Imaging of LSMO Thin Films Using Scanning Electron Microscopy with Polarization Analysis.
Magnetics and Optics Research International Symposium 2013, Saitama, Japan.

Poster

D. Schönke, **P. Krautscheid**, M. Lauf, B. Krüger, R. M. Reeve and M. Kläui.
SEMPA imaging of magnetic spin configurations and manipulation by spin currents.
Deutsche Physikalische Gesellschaft Frühjahrstagung 2017, Dresden, Deutschland.

R. M. Reeve, **P. Krautscheid**, M. Lauf, D. Schönke, B. Borie, B. Krüger und M. Kläui.
Domain Wall Spin Structures in Mesoscopic Fe Rings.
Joint European Magnetic Symposia (JEMS) 2016, Glasgow, Schottland.

P. Krautscheid, D. Schönke, M. Lauf, B. Kräger, R. M. Reeve und M. Kläui.
Magnetic Imaging of Domain Wall Spin Structures in Fe Rings using SEMPA.
Deutsche Physikalische Gesellschaft Frühjahrstagung 2016, Regensburg, Deutschland.

P. Krautscheid, M. Lauf, R. M. Reeve, B. Krüger und M. Kläui
High Resolution Imaging of Nanoscale Structures using SEMPA.
Deutsche Physikalische Gesellschaft Frühjahrstagung 2015, Berlin, Deutschland.

R. M. Reeve, C. Mix, M. König, **P. Krautscheid**, C. Engel, M. Foerster, G. Jakob und M. Kläui.
Surface spin polarization of LSMO thin films probed by scanning electron microscopy with polarization analysis at variable temperature.
IEEE International Magnetics Conference 2014, Dresden, Germany.

P. Krautscheid, R. M. Reeve, B. Krüger und M. Kläui
High Resolution Imaging of Magnetization in Nanoscale Structures for Spin Current Based Devices.
Deutsche Physikalische Gesellschaft Frühjahrstagung 2014, Dresden, Deutschland.

P. Krautscheid, R. M. Reeve, C. Mix, M. König, C. Engel, M. Foerster, G. Jakob und M. Kläui.
Magnetic Imaging of LSMO Thin Films using Scanning Electron Microscopy with Polarization Analysis.
Drei Königstreffen (2014), Bad Honnef, Deutschland.

Robert M. Reeve, **Pascal Krautscheid**, Markus König, Christian Mix, Michael Foerster, Gerhard Jakob, and Mathias Kläui.
Temperature Dependent High Resolution Imaging of the Domain Structure of LSMO Thin Films via SEMPA.
Deutsche Physikalische Gesellschaft Frühjahrstagung 2013, Regensburg, Deutschland.